An experimental investigation of oscillating spheres in a very viscous fluid

A thesis submitted to the University of Manchester for the degree of

Doctor of Philosophy

in the Faculty of Engineering and Physical Sciences

2014

Finn Box

School of Physics and Astronomy

Contents

Word count: 48,946

4

List of Tables

List of Figures

6

8

9

11

Abstract

An experimental investigation of a sphere performing torsional oscillations in a Stokes flow is presented. A novel experimental set up was developed which enabled the motion of the sphere to be remotely controlled through application of a magnetic field. The response of the sphere to the applied field was characterised and good agreement with a theoretical model was found. The effect of nearby boundaries were investigated in two cases; when the rotational axis of the sphere was (1) parallel and (2) perpendicular to the normal to the bounding surface. The interaction between a torsionally oscillating sphere and an otherwise stationary sphere was then studied for various combinations of spheres. The effect that a tether connecting the spheres had on the dynamics of two interacting spheres was considered by comparing tethers of different materials. Finally, a multi-body configuration of spheres connected by elastic tethers which propelled itself in a Stokes flow when actuated magnetically was developed. Throughout the investigation Particle Image Velocimetry, a quantitative flow visualisation technique, was used to determine the resultant flows and provide insight into the fluid dynamics.

Declaration

No portion of the work referred to in this thesis has been submitted in support of an application for another degree or qualification of this or any other university or other institution of learning.

Finn Box

School of Physics and Astronomy

University of Manchester

Oxford Road

Manchester

M13 9PL

March 2014

Copyright

The Author

'Why don't you tell me a story?'

'Please tell me a story, too'

'You know, I think I'll tell you the story of my life'

'You tell me!'

'I wanna hear too'

'I was born in Telford, Shropshire, a long time ago, see. And now I'm lucky enough to be here with you'

'Yeah, but what happened in between?'

'Yeah, what else happened?'

'Well, it, uh, went pretty much like this...'

Adapted from 'Life Story' - The Hellers (Command Records, 1968)

The Art of Puncture Repair

In my family, my impracticality is renowned and best exemplified by an inability to fix a flat bicycle tyre. Imagine the bemusement when I began a PhD in experimental physics. I would like to gratefully acknowledge the glass-ridden streets of Manchester, and the following people, for teaching me how to fix a puncture, amongst others things.

First and foremost, I would like to thank Professor Tom Mullin for teaching me how to teach myself, and opening my eyes to the beauty of fluid motion. And for the cheese sandwiches in Chinley. Dr. Carl Tipton, of Crazy Carl's Mad Labs, is gratefully acknowledged for showing me how to be an experimentalist in a physics laboratory, and electrocuting me in the process. I am indebted to Assistant Professor Yuji Tasaka for inviting me to Japan to learn quantitative flow visualization methods, which became such an important part of my work. I would mainly like to thank Paul Tipler for the banter, but the technical assistance he provided throughout many iterations of many experiments is also hugely appreciated. Furthermore, without various donations of experimental equipment I would have had no experiment and I am therefore grateful to Professor Andrew Murray, Professor Kostya Novoselov and Dr. Paul Walmsley.

On a less technical note, I would like to thank Professor Anne Juel for

Chapter 1

Introduction

In his celebrated work '*On the effect of the internal friction of fluids on pendulums*' [1], G. G. Stokes considered the motion of a sphere in a very viscous fluid and provided the foundation for subsequent studies of the motion and interaction of particulate matter in viscous fluids. Scientific advances in this field have been numerous and recent technological developments have resulted in increased applications of the laws governing the motion of particles in viscous fluids. The fluid dynamics of a sphere performing torsional oscillations in a viscous fluid has received little experimental attention, however, since it was first considered theoretically in 1860 [2]. Furthermore, the experimental work which has concerned the torsionally oscillating sphere was performed using a sphere with a supporting rod or fibre, like the work conducted by Stokes was performed using a pendulum, and the effects of the support on the flow were not considered [3–6].

This thesis presents results from an experimental investigation into the torsional oscillations of a sphere in a very viscous fluid. The experimental work presented here was conducted on a free sphere, the motion of which

was controlled using an applied magnetic field. The aims of the investigation were to (a) provide quantitative data from careful experiments which can be compared with available theoretical predictions concerning the fluid motion generated by an oscillating sphere, (b) to inspire further theoretical progress by considering the effect of nearby boundaries and the interaction of pairs of spheres and (c) to apply knowledge of the interaction of spheres in a very viscous fluid to the development of an actuated device capable of swimming at low Reynolds number.

In §1.1, a brief discussion is presented of a dimensionless parameter, the Reynolds number, and its implications. The literature concerning the torsional oscillations of a sphere in a viscous fluid is reviewed in §1.2. The analogous example of a steady rotating sphere is discussed in §1.3 and the effects which arise from close proximity of a rotating sphere to a solid boundary are considered in §1.4. In §1.5, the propulsion of multi-body configurations of spherical particles and other synthetic swimmers is used to explore how locomotion can be achieved in viscosity dominated, low Reynolds number flows. Finally, in §1.6, a preview is presented of the structure of the thesis.

1.1 Experimental Realisation of a Stokes Flow

The presented results were obtained in an experimental realisation of a Stokes flow and it is necessary to consider the implications of low-Re fluid dynamics. The Reynolds number, Re, is a dimensionless parameter which is determined by the ratio of the inertial to viscous forces in a fluid system. It is defined as $Re = UL/\nu$ where U is the characteristic velocity of the system, L the characteristic length of the system and ν the viscosity of the fluid. At low

Re, $Re << 1$, the inertial term in the governing equations of motion, the Navier-Stokes equations, becomes negligible and in the limit of $Re \to 0$ the fluid velocity satisfies the linear Stokes equations. Thus motion is determined by viscous, not inertial, forces and fluid transport is dominated by viscous diffusion.

Results were obtained for Reynolds numbers typically < 0.1 so that the motion is considered primarily as Stokesian, although small departures were found from Stokes flow and these are discussed. The consequences of Stokesian fluid dynamics on locomotion is revisited later in §1.5 but first the dynamics of a spherical particle at low Re will be reviewed.

1.2   Studies of a Torsionally Oscillating Sphere

The torsional oscillations of a sphere immersed in, and also enclosing, a viscous fluid were first discussed theoretically and experimentally by Helmholtz and Piotrowski in 1860 [2] with regards to the specific application of a viscometer. The viscosity of the fluid can be calculated from the logarithmic decrement of decaying oscillations of a sphere suspended from a torsion fibre, a configuration known as a torsion pendulum. The sphere is deflected from the equilibrium position and subjected to the restoring couple of the fibre and the surrounding fluid. Using this method, and enclosing the fluid within a spherical shell, Andrade [7] devised an apparatus capable of determining the coefficient of viscosity to an accuracy of less than 0.5%. This technique is suitable for measuring the viscosities of substances which react with air, such as molten metals, as the fluid is completely encased. Andrade also concluded that no slip took place between the liquid and the sphere surface, contrary

to the belief of Helmholtz and Piotrwoski.

In 1891, Buchanan [8] considered the oscillatory motion of a solid spheroid suspended in a viscous fluid by a torsion fibre. He analytically derived the solution for the primary velocity field generated by, and the resistive hydrodynamic torque acting on, a spheroid performing damped rotary oscillations in an unbound, incompressible, viscous fluid. The solution for a sphere was then obtained by reducing the ellipticity of the prolate sphere to zero. Buchanan concluded that, if the fluid is initially at rest, the resulting fluid motion will be circumferential in annuli around the axis of rotation. Thus the entire fluid can be thought to move in concentric shells around the oscillating sphere.

Small torsional oscillations of a solid sphere, deflected from the equilibrium position in an otherwise quiescent viscous fluid under an elastic restoring force or couple, were examined by Kestin [9]. This work considered both the motion of the sphere and the surrounding fluid, including initial transient motion. Exact solutions of the Navier-Stokes equations were presented after simplification through omission of the inertial terms, which restricts the validity of the solutions to small oscillations and negligible secondary fluid motion. The solutions for the fluid motion were in agreement with the spherical shell solution previously obtained through the method of separation of variables [10].

Lamb solved the unsteady Stokes equations for concentric spheres, the inner of which executed rotary oscillations, and obtained a solution as a series of spherical harmonics. The solution for a single, free sphere performing torsional oscillations in an infinite mass of incompressible viscous fluid was then obtained by extending the radius of the outer sphere to infinity whilst

maintaining constant pressure. The torque on the sphere was also calculated from the stress components on the surface of the sphere.

Kanwal [11] investigated the oscillatory rotation of rigid axi-symmetric bodies about an axis of symmetry in a viscous, incompressible fluid using Stoke's stream function. A solution was obtained in terms of spheroidal wave functions of complex arguments and good agreement was found with the solution of Lamb [12]. This work was later extended to consider the slow rotary oscillations of a sphere in a fluid bounded by an infinite cylinder, the axis of which coincides with the axis of rotation of the sphere [13].

Tekasul *et al.* [14] numerically solved for the torque on a torsionally oscillating sphere in an unbound medium using a Green's function approach and found a less than 0.1% difference with analytic solutions. This work was extended to include numerical solutions with slip between the fluid and the sphere surface, which is of interest in micro- and nano-fluidic conditions [15]. Lei *et al.* [16] calculated the viscous torque on a spherical particle under arbitrary rotation and a particle rotating in a velocity field rather than a still fluid. By considering a characteristic dimension of the body, Zhang and Stone [17] extended the analysis to the oscillatory translations and rotations of nearly spherical particles.

The aforementioned studies assumed the fluid moves in concentric circles around the torsionally oscillating sphere, and the centres of these annuli lie on the axis of rotation. Carrier and Di Prima [18] used perturbation techniques to solve the nonlinear Navier-Stokes equations which result when the radial and axial flows are not neglected. Their work uncovered a secondary circulatory motion in planes containing the axis of rotation: fluid recedes

from the sphere along the equatorial plane and flows in at the poles. This inertial effect results from a centrifugal force which is greatest at the equator. A pressure-gradient counteracts the normal component of the centrifugal force suppressing separation from the sphere surface. However, the pressure-gradient cannot counteract the tangential component of the centrifugal force which instead manifests as a circulatory flow driven by an inflow at the poles and an outflow at the equator. The secondary flow results in a steady pumping which increases with increasing oscillation amplitude and decreases with increasing frequency of oscillation [3].

The fundamental circumferential motion and the secondary, circulatory streaming motion interact and a correction term to the torque acting on a sphere was calculated by Carrier and Di Prima [18]. However, disagreement between predicted amplitude effects and experimental measurements by Folse *et al.* [4] led to identification of an algebraic error in the original calculation of the correction to the torque [19]. Folse *et al.* measured the relative change in added moment of inertia due to viscous effects, and the relative change in the logarithmic decrement of a sphere suspended between two rods (a torsion pendulum constrained in the transverse direction from below by a supporting rod). The gradual variation of the damping rate was subsequently explained by the weakly nonlinear theory of Di Prima and Liron [19]. Gopinath [20] also investigated steady-streaming effects and concluded that the streaming is generated by viscous-like forces yet is independent of viscosity.

It is of interest to note that relatively few experimental investigations have been conducted, and all experimental work was performed on a torsion pendulum: a sphere suspended in the viscous fluid by means of a torsion

fibre or mechanically driven rod, and at times supported from below to prevent transverse motion [3–6]. The torsion pendulum was either subject to an initial deflection and then left to approach the equilibrium position through decaying oscillations [4–6], or was driven by an external motor with oscillations of constant time-period [3]. The effect of the motion of the supporting fibre or rod on the resulting flow was neglected in all cases. Furthermore, the experimental work performed mainly concerned the inertial effects which occur at $Re > 1$. For instance, Hollerbach *et al.* [3] conducted flow visualisation of the radial jet which results from hemispherically symmetric circulatory flows colliding at the equator. The radial jet is ejected along the equator and, for large-amplitude oscillations, generates vortex pairs which break down into turbulence.

No literature has been uncovered which concerns the influence of boundaries on the flow generated by a torsionally oscillating sphere. The impact of solid boundaries on a sphere rotating with constant angular velocity, however, has received considerable attention in the literature. The relevant work on a steady rotating sphere in a viscous fluid is summarised in the following section to provide insight into the analogous case of the torsionally oscillating sphere.

1.3   Studies of the Steady Rotation of a Sphere

The steady rotation of a sphere in an infinite, incompressible mass of viscous fluid was first considered by Stokes [1]. The transversely oscillating sphere, and a sphere translating in a straight line with uniform velocity, in a viscous fluid were also discussed. Stokes noted that if the second-order terms in the

Navier-Stokes equations are taken into account then the motion of a sphere rotating about a fixed axis generates an inflow parallel to the axis and an outflow parallel to the equatorial plane, similar to the case of the torsionally oscillating sphere. Jeffery [21] neglected the second-order, convective terms and solved for the velocity of a spherical shell of fluid surrounding the sphere. The resistive torque exerted by the fluid on the sphere was also determined and found to be an accord with the earlier approximate solution of Kirchoff [22].

The secondary streaming in the meridional plane was first treated in depth by Bickley [23] who discovered that the change from inflow to outflow takes place on the surface at an angle of $54.5°$ from the rotational axis. Bickley also noted that the secondary flow contributes to the viscous dissipation of energy and exerts a small secondary torque on the sphere. The coefficient of torque resulting from the secondary flow was calculated by Collins [24]. Takagi [25] used a power series expansion to calculate the torque up to the order of Re^{14} and also calculated the vorticity, skin-friction and pressure on the surface of the sphere. Determination of the intrinsic hydrodynamic resistance to rotation was extended to arbitrary particles using tensors which were dependent on the exterior geometry of the particle [26].

Sawatski [27] conducted a comprehensive investigation of the flow field in the vicinity of a sphere rotating with constant angular velocity in a viscous fluid over the range $10^0 < Re < 10^7$, with a focus on the boundary layer development and the laminar-turbulent transition to a fully developed boundary layer. A further investigation of the flow around a sphere rotating in Newtonian and visco-elastic liquids was conducted with the specific aim

of developing a rotating sphere viscometer [28]. Good agreement was found between the experimental measurements and theoretical predictions of the primary flow for radial distances, r, of up to $r/a \simeq 4$. The secondary flow was found to reverse for visco-elastic fluids due to the dominance of elastic effects over inertial effects.

The unsteady, yet non-oscillatory, rotation of a sphere in an unbound, viscous fluid was first considered by Basset who examined a sphere set impulsively into rotation [29]. The suddenly-started rotating sphere was investigated using analytical [30] and numerical methods [31], and the transient flow pattern caused by an impulsive twist applied to an initially stationary sphere in a viscous fluid has also been examined [32]. A historic rotational term in the expression for the torque acting on a sphere when the motion is unsteady has been derived [33]. Finally, a *lift* force, which acts orthogonally to the direction of motion and the axis of rotation, was found [34], and later confirmed [35], to act on a spinning sphere translating through a fluid for small but non-zero Re flow. This transverse force is in addition to the drag force experienced by the sphere, and, for small Re, is independent of viscosity.

1.4 Studies of Boundary Effects on Rotating Spheres

The presence of nearby boundaries affects the fluid motion generated by the rotation of a sphere in an otherwise quiescent, Stokes flow. Symmetrical boundaries, such as a concentric bounding shell, increase the hydrodynamic

27

resistance exerted on a sphere and form the basis of rotating sphere viscometers [36] as discussed in §1.4.3. The introduction of planar boundaries break the symmetry of the system and the no-slip condition of the surface of the boundaries introduce additional viscous effects. The variation of the Stokes' drag force on a sphere translating in a fluid, and the rotational equivalent experienced by a spinning sphere, have been measured as a function of distance from a solid boundary using optical tweezers to control the particle position and motion [37]. Understanding of the forces and torques which result from walls, and their functional dependence on wall-sphere separation, are important in microfluidic and biological systems. In particular, the net force which acts on a spherical entity rotating near a wall results in propulsion and provides insight into the swimming mechanisms of micro-organisms in bounded low-Re flows. Two scenarios are to be considered; a sphere rotating about an axis (a) parallel, and (b) perpendicular, to the surface normal of the planar boundary, as shown in the schematic diagram in Figure 4.1.

1.4.1   A Parallel Boundary

For a sphere performing steady rotation about an axis which is parallel to the surface normal of a nearby boundary, an increase in resistive couple due to viscous-dissipation effects is induced by the boundary and increases as the sphere approaches the boundary. The dependence of the torque correction on separation distance changes depending on whether the sphere is very close to [21] or far from the boundary [38].

In the Stokes regime, this scenario was originally considered by Jeffery [21] who calculated the increase in hydrodynamic resistance as a function of wall-
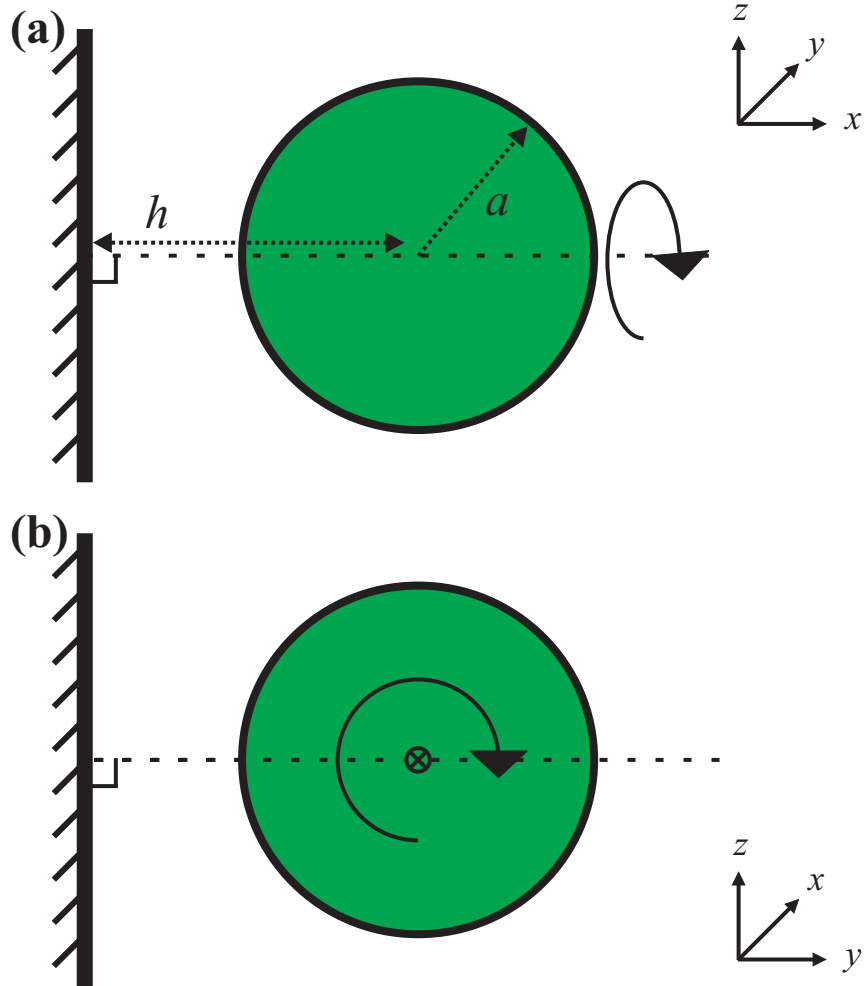
Figure 1.1: Schematic diagram of the orientation of the rotational motion of the sphere with respect to the bounding plane. The solid boundary is denoted by the thick line on the left-hand side of the image, the surface normal to the boundary is denoted by the horizontal dashed line to which the rotational axis of the sphere is (a) parallel and (b) perpendicular. The sphere-wall separation distance, h, is measured from the centre of the sphere to the surface of the boundary. The rotation direction is depicted by the curved, black arrow and the radius of the sphere, a, is depicted in (a).

sphere separation. Jeffery discussed the hydrodynamic torque exerted on a solid sphere rotating in a viscous fluid enclosed by a concentric, and a non-concentric, spherical shell. Takagi [39] examined the case of steady rotation around an axis parallel to the surface normal when studying the slow rotation of a sphere in close proximity to another, free sphere. In the limit of the free sphere becoming infinitely large, the rotating sphere could be considered to be close to an infinite planar boundary. Brenner [40] extended the effect of boundaries on the Stokes resistance to arbitrarily-shaped particles and found that the magnitude of the wall effect for the translation of a particle was much greater than for rotation, a result which has been confirmed experimentally [37].

Liu and Prosperetti [41] used numerical methods to investigate the effects of inertia in the system for Re up to 100. The parallel boundary inhibits the poleward flow and radial jet which are produced by the sphere. The unbalanced momentum results in a net force directed toward the wall parallel to the surface normal. Both the net force and resistive torque reduce with increasing wall-sphere separation. For Stokes flow, however, the net wall-parallel force acting on the sphere is zero, as no circulatory flow exists, and the resistive couple is significant as viscosity dominates [41].

1.4.2   A Perpendicular Boundary

For a sphere performing steady rotation about an axis which is perpendicular to a nearby boundary, Dean and O'Neill [42] analytically solved the Stokes equations for rotation perpendicular to the surface normal using bipolar co-ordinates. Goldman *et al.* [43] derived asymptotic, lubrication-like solutions

for the case where the gap-width approaches zero. The discrepancy between the obtained theoretical solutions and avaiable experimental data were explained by considering cavitation, a point which was investigated further by Ashmore *et al.* [44]. Chaoui and Feuillebois [45] used numerical methods to obtain precise expressions for the fluid velocity which allowed calculations of the fluid trajectories around a sphere close to a wall in a shear flow. As in the case of a parallel boundary, the presence of the perpendicular boundary introduces a strong resistive torque because of large viscous effects which diverge as the sphere approaches the boundary. This also results in two forces: a force directed parallel to the boundary and a force directed perpendicular to the boundary [43].

The force directed parallel to the boundary originates from viscous shear and causes the sphere to translate. For $Re < 1$, the direction of translation is in the direction the sphere would roll down the plane if it were free [41]. This wall-parallel force generated by a sphere rotating near a boundary is analogous to the torque experienced by a sphere translating near a boundary [46, 47]. Goldman *et al.* [43] acknowledged this *cross-effect* relationship: the force (per unit angular speed) exerted on a rotating sphere must equal the torque (per unit translational speed) exerted on a translating sphere.

A build-up of pressure results from fluid being squeezed between the sphere and the boundary and results in a force directed perpendicular to the boundary. For $Re < 1$, viscosity dominates in the gap between the sphere and the boundary and the wall-normal force is repulsive, forcing the sphere away from the boundary. This wall-normal force is greater at smaller separations and decreases rapidly with increasing separation [41]. The wall-normal force

is less significant than the wall-parallel force, and both effects decrease with increasing separation.

The analytic solutions of Dean and O'Neill [42] and Jeffery [21] can be combined to find the increased resistive torque due to the arbitrary orientation of the rotational axis from the planar boundary. Perkins and Jones [48] constructed grand resistance and mobility matrices in a general direction and orientation relative to a hard wall using a function with no divergent part, and were thus able to find explicit expressions for all gap-widths. Finally, Cox [49] calculated the hydrodynamic force and torque on a solid sphere at an arbitrary position from a planar boundary in a general, 2-dimensional flow at $Re = 0$. The result was used to describe the motion of spherical, non-zero size particles across streamlines, which resulted in local changes in concentration, in a prescribed undisturbed flow; a phenomena which has been observed experimentally and is entirely due to boundary effects [49].

1.4.3   The Rotating Sphere Viscometer

The case of a sphere performing steady rotation in a viscous fluid has received far more attention in the literature than the case of a torsionally oscillating sphere. However, the concept of using a steady rotating sphere to measure the viscosity of the fluid in which it is submerged was not considered until more than a century after Helmholtz and Piotrowski discussed the use of torsional oscillations of a sphere for viscosity measurements [2]. In the 1960s, Walters and co-workers demonstrated that measurement of the couple exerted on the sphere could provide a means of measuring the fluid viscosity [36], and experimental observation of the streamline pattern could provide a simple

qualitative check on rheogeniometer measurements [50]. A sphere rotating inside a concentric spherical container filled with viscous fluid where the ratio of the radii of the two spheres is $\sim 1:12$ results in the outer sphere having an effect of $< 1\%$ on the couple of the rotating sphere.

With the specific aim of developing a rotating sphere viscometer, Kelkar *et al.* [28] conducted an experimental investigation into the primary flow around a sphere rotating in Newtonian and visco-elastic fluids using a 3-dimensional particle imaging technique that was the precursor to modern flow visualization techniques such as Particle Image Velocimetry. Good agreement was found with the theoretical description of primary flow for radial distances up to $r/a \cong 4$; divergence of experimental results from theoretical predictions at greater distances was attributed to the influence of the container walls.

More recently, the rotating sphere viscometer has been developed and adapted for medical, biological and micro-fluidic applications. The advantage of a viscometer based on rotational motion, compared to the more conventional methods based on translational motion, is that a smaller volume of fluid is probed. This enables the measurement of the rheological properties of small, micro- to pico-litre, volumes of viscous fluids [51]. Experiments performed within cells and with eye fluid have demonstrated the suitability of rotating sphere viscometers for non-invasive, *in vivo* testing [52]. Furthermore, ingenious methods of non-mechanical control of the sphere rotation have been developed to eradicate the friction between the rotational axis of the sphere and the mechanical support, which often restricts the lower limit of viscosity measurement [53]. Examples of non-mechanical control are the optical application of a torque to a spherical particle trapped by laser

tweezers [52]; the electromagnetically spinning sphere viscometer, which uses a rotating magnetic field to drive the rotation of an aluminum sphere [53]; and the suspension of spherical, ferromagnetic particles in a viscous fluid, the orientation of which is then be controlled by the application of a magnetic field [51].

1.5   Life at Low Reynolds Number

At low Re fluid velocity is governed by the Stokes equations which have no inertial term. This has two significant implications on locomotion at low Re: the viscous forces which result from the deformation of a body do not depend on the rate of deformation, and time-reversible deformation of a body does not result in net displacement of the body [54]. These two factors contradict our intuitive understanding of swimming (which, for a human in water, occurs at $Re \sim 10^3$) in which cyclic deformations of a body in a fluid result in inertial forces, and a momentum, that propels the body through the fluid.

For propulsion at low Re, a body must undergo periodic, yet non-reciprocal deformation in order to generate non-zero net forces [55]. A body which deforms through a sequence of geometrical shapes may swim in a low-Re flow, provided the sequence of shapes is not identical when viewed after a time-reversal transformation. A body, free from external forces and torques, which self-propels at low Re is known as a swimmer [56]. The small scale of swimming microorganisms mean that biological examples of swimmers are plentiful. Examples of artificial, man-made swimmers are less numerous. However, recent advances in nanotechnology have led to promising methods

of exploiting low-Re propulsion for *in vivo* site-specific drug delivery [57].

The propulsive mechanisms of multi-body configurations of spherical particles have been explored both theoretically and experimentally. A one-dimensional swimmer consisting of three spheres linked by rigid rods has been studied extensively [58–62]. An internal engine in the middle sphere acts as an active element and changes the length of the connecting rods. A non-zero phase difference in the continuous, periodic motion of the two rods breaks the time-reversal and the translational symmetry, resulting in loco-motion in a direction parallel to the arms of the swimmer. Experimental validation of the three-sphere swimmer design was obtained by controlling the motion of beads in glycerol using optical tweezers [63]. The modes of motion were recreated and the flow generated by the pumping action of the cilia beads proved the configuration could swim. Further studies have shown that the presence of a nearby solid boundary causes the swimmer to reorientate [64] and the interaction between two swimmers is dominated by the relative phase of their swimming strokes [65]. The motion of the swimmer has also been considered in a non-stationary flow [66]; if the two end spheres were made of ferromagnetic material, then the swimmer could be navigated in a shear flow through application of an external magnetic field.

The dynamics of a collection of swimmers which comprise rotating spheres, and passive spheres, connected by rigid rods have also been described [67,68] and studied in the presence of a nearby solid boundary [69]. The dynamic behaviour of a swimmer consisting of actuated, rotating spheres and rigid connections has been investigated experimentally [70]. A swimmer consisting of one magnetically hard particle and one magnetically soft particle was

devised by Ogrin *et al.* [71]. Application of an elliptically rotating uniform magnetic field led to the non-reciprocal, periodic motion of the two spheres and net displacement of the swimmer. The external forces and torques which arise from application of a magnetic field mean the device is not, by definition, a swimmer [56]. However, magnetically-driven propellers can provide insight into the propulsive mechanisms of swimmers.

The buckling of a ferromagnetic filament subjected to an alternating current (AC) magnetic field may result in the symmetry-breaking deformation necessary to achieve locomotion [72]. A flexible magnetic filament attached to a red blood cell was experimentally demonstrated to swim upon application of an AC field [73, 74]. The free end of the filament followed the field direction and a bending wave propagated along the filament to the end attached to the red blood cell, propelling the swimmer in the opposite direction. Magnetically-driven flexible nanomotors provided the first example of directed delivery of polymeric drug carriers [57]. The nanomotors comprised a flexible tail, which deformed in a chiral fashion, and a magnetic head that was actuated by a rotating magnetic field [56].

Numerical simulations have shown that a magnetic dipole attached to a flexible tail also behaves as a swimmer when subjected to an unsteady magnetic field [75]. A bending wave propagates from the actuated magnetic dipole to the tip of the tail. Actuating an elastic filament makes the filament a function of the fluid flow which breaks the time-reversibility of the motion and results in locomotion [76]. Synthetic swimmers which exploit the actuation of a flexible filament have been realised experimentally. Wiggins *et al.* [77] oscillated a latex bead using laser tweezers and observed propagating waves of

displacement along the attached filament. Yu *et al.* [78] developed a robotic swimmer which consisted of an actuation device housed inside the swimmer body and attached to an elastic tail.

Thus, it has been shown that the potential implementation of synthetic swimmers in future *in vivo* drug delivery [57], and as pumps in microfluidic devices [63], means that the study of low-Re swimmers is of significant engineering importance as well as of scientific interest.

1.6   Thesis Structure

In Chapter 2, the experimental set-up used to control the torsional oscillations of a sphere in a very viscous fluid is described. Calibration of the magnetic field used to drive the motion of the sphere is presented, as is the method used to illuminate and observe the motion of the sphere. The equipment and techniques used to quantitatively visualise the fluid motion are also described. The dynamic response of a sphere to the applied magnetic field is detailed in Chapter 3. This includes derivation of a model describing the torques that act on the sphere. The flow generated by a sphere is measured and compared to a theoretical prediction of the fluid velocity.

In Chapter 4, the effects of a boundary on the motion of the sphere and the resultant flow are considered. The modifications to the experimental set-up are described before results obtained for a parallel boundary and a perpendicular boundary are presented and discussed. In Chapter 5, the perpendicular boundary is replaced by a passive sphere. Results concerning the interaction between a torsionally oscillating sphere and a passive sphere are presented for a variety of combinations of pairs of spheres. The combination

of sphere-pairs include spheres of equal and unequal radii.

The introduction of a tether that connects the two spheres is considered in Chapter 6. Effects which result from changes in the length and material properties of the tether are described. A low-Re swimmer comprising a multi-body configuration of tethered spheres is then detailed. The locomotive mechanism of the swimmer is also discussed. The work presented in this thesis is summarised in Chapter 7. Conclusions drawn through interpretation of the experimental results are highlighted and possible extensions of the work are proposed.

In Appendix A, a discussion is presented of the effects of the background magnetic field on the dynamic response of the sphere to the applied field. Appendix B contains details of the pairs of sphere used in Chapter 5. In Appendix C, a model is outlined which describes the fluid dynamics of a torsionally oscillating sphere interacting with a boundary and a passive sphere.

Throughout his PhD, the author investigated further nonlinear phenomena, including; the transition to turbulence in pipe flow, the highly nonlinear vortices which form from the interaction of a transverse jet with a Hagen-Poiseuille crossflow, the buckling of elastomeric and plastic lattices under dynamic compression, and the radial segregation of granular material in a rotating drum. In Appendix D, two publications are presented. The author contributed to these publications during the course of his PhD, however the work contained within them is not directly related to the investigation presented in this thesis.

Chapter 2

Experimental Apparatus and Techniques

A novel experimental system was developed to investigate the fluid motion induced by spheres which were forced to oscillate in a very viscous fluid. A schematic diagram of the experiment is shown in Figure 2.1. Near neutrally-buoyant spheres, containing neodymium magnets, were submerged in a very viscous fluid. A magnetic field was applied to the system, using large Helmholtz coils and oscillation of this field resulted in the periodic torsional motion of the spheres. The tank containing the viscous fluid was positioned on a platform of adjustable height in the centre of the Helmholtz coils. The electromagnet was surrounded by a Mumetal canister which reduced the effect of any extraneous magnetic fields. A Hall effect probe was used to measure the applied magnetic field, while a camera and an optical arrangement of mirrors enabled observation of the dynamic response of the spheres.

The individual components of the experimental arrangement are described
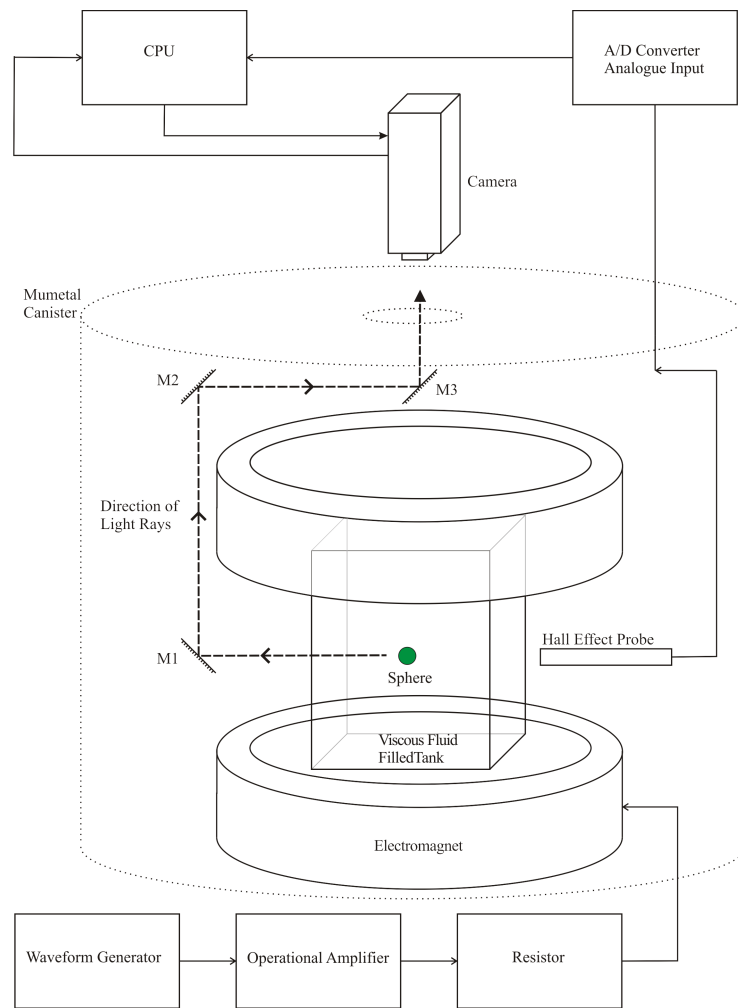
Figure 2.1: Schematic diagram of the experimental apparatus. Near neutrally-buoyant spheres in a viscous fluid filled tank were imaged using an optical arrangement of mirrors (M1, M2 and M3) and a computer-controlled camera. A magnetic field was applied using Helmholtz coils and measured by a Hall effect probe connected to a PC via an 16-bit analogue-to-digital signal converter. The current supplied to the Helmholtz coils was modulated using a waveform generator, amplified by an operational amplifier and passed through a resistor which acted as a resistive load. The experimental system was contained within a Mumetal canister to reduce the effects of extraneous fields.

40

in greater detail in the following sections. The spheres, and the positioning of the magnets within them, are described in §2.1. The dimensions and the physical properties of the magnets are then detailed in §2.2. Measurements of the viscosity and density of the viscous fluid, silicone oil, are presented in §2.3. Section 2.4 details the applied magnetic field and includes a discussion of the magnetic shielding. Steady (DC) magnetic fields were used to calibrate the electromagnet and a working region of uniform, consistent magnetic field was identified, as detailed in §2.4.1. Experiments were performed with alternating (AC) magnetic fields and the range of frequencies used in the experiments is documented in §2.4.2. The optics which were used to provide illumination and observation of the spheres are detailed in §2.5. Also included is an outline of the image analysis process employed to measure the motion of the spheres. Finally, an adaption of the experimental set-up is described in §2.6 which enabled the quantitative measurements of the flow fields generated by the motion of the spheres. The flow visualisation techniques used to conduct flow diagnostics, Laser-Induced Fluorescence (LIF) and Particle Image Velocimetry (PIV), are then discussed in greater detail in §2.6.2 and §2.6.3, respectively.

2.1   Spheres

The spherical particles used throughout this investigation were polypropylene spheres, manufactured by Dejay Distribution Limited UK, which had a density of 941.12 kgm^{-3}. Permanent magnets, described in further detail in §2.2, were inserted into machined holes in the spheres and small amounts of glue were used to keep them in place. Application of a magnetic field induced

a torque which acted to align the magnets with the applied field. Effectively, the torsional motion of the spheres was driven by an applied magnetic field.

Magnets were embedded into spheres of diameters 15.86 ± 0.01 mm and 12.70 ± 0.01 mm. In the spheres of diameter 15.86 mm, two magnets were embedded such that they were flush with the surface and diametrically opposite ($\pm 1°$) along an axis through the centre of the sphere as shown in Figure 2.2. The adjacent poles of the two magnets had opposite polarity and the two magnets therefore acted as a magnetic dipole, the length of which was equal to the sphere diameter. In the spheres of 12.70 mm diameter, one magnet was inserted into the centre of the sphere. Polypropylene spheres of diameters 15.86 ± 0.01 mm, 12.70 ± 0.01 mm, 9.53 ± 0.01 mm and 6.34 ± 0.01 mm that did not contain magnets were also used in this study. The interaction between magnetically driven, *active* spheres and non-driven, *passive* spheres is detailed in Chapter 5, and a multi-body configuration of connected spheres is investigated in Chapter 6.

The spheres contained a small air bubble which was less than 1% of the volume of the sphere and a result of the manufacturing process. A close approximation to neutral buoyancy for both magnetic and non-magnetic spheres was achieved by embedding 0.5 mm diameter bronze spheres into the surface of the polypropylene spheres. The spheres had a non-uniform density distribution that introduced a gravitational torque into the system which is discussed further in §3.4.1. The zero-field orientation of the magnetic dipole of the active spheres was controlled by careful positioning of the embedded weights. Attainment of near neutral buoyancy and approximately consistent zero-field orientation meant that reproducible results were

obtained for different spheres. The average density of the spheres used in the experiments will be specified in the relevant sections.
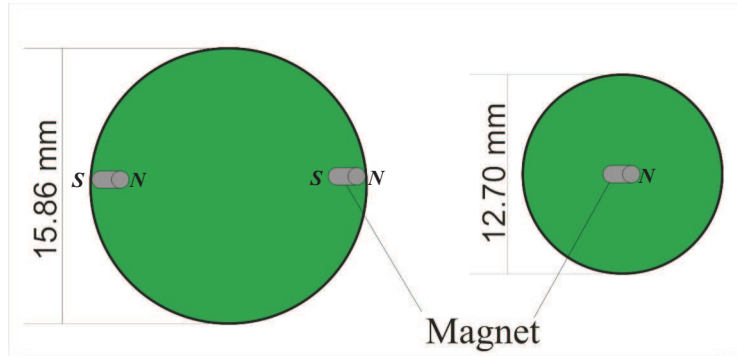
Figure 2.2: Schematic diagram illustrating the location of the neodymium permanent magnets within the polypropylene spheres. The magnets were inserted into machined holes in the spheres and glued in position. The position of the magnetic poles of the magnets are indicated on the diagram.

2.2   Neodymium Magnets

The permanent, cylindrical neodymium magnets embedded into the spheres were 3.00 ± 0.01 mm in length with a diameter of 2.48 ± 0.01 mm, occupying less than 2% of the sphere volume. Magnetically hard neodymium magnets were used as the effect of the applied magnetic field on their magnetisation was negligible. The permanent magnets had a remanence of 1.19 ± 0.05 T and a coercivity ≥ 868 kAm^{-1} [79]. Remanence is a measure of the remaining magnetisation after an applied field is removed, and the coercivity is the applied field required to reduce the magnetisation to zero after attaining magnetic saturation. These values suggest that the strength of the neodymium magnets is large for their size compared to standard ferromag-

43

netic materials such as iron. The magnetic dipole moment of an individual magnet, $\mu = 0.0140 \pm 0.0006$ Am^2, was effectively independent of the applied magnetic field for the range of values used [80].

2.3 Viscous Fluid

Spheres were submerged in a viscous liquid inside a rectangular tank, made of 5 mm thick perspex with internal width 125 mm, length 115 mm and height 200 mm. The working fluid was silicone oil (Basildon Chemical Company Limited, Oxfordshire, UK) with a manufacturers value of the kinematic viscosity of 1000 cSt at 25 °C. The viscosity of the silicone oil was measured as a function of temperature using a shortened form suspended level viscometer (BS/IP/SL(S) Size 8, Poulton, Selfe and Lee Ltd., Essex, UK) and a temperature-controlled water bath. A linear dependence of viscosity on temperature is shown in Figure 2.3, where the experimental data points are represented by blue circles. The fit to the data was derived using the least-squares method and has the form $\nu = (-17.64 \pm 0.37)T + (1.275\mathrm{x}10^3 \pm 7.71)$ mm^{2}s^{-1}, where ν is the kinematic viscosity of the fluid, and T is the temperature in degrees Celsius. Experiments were performed in a air-conditioned laboratory where the room temperature was maintained at 20 ± 1 °C to minimise variations in the viscosity. The viscosity of the silicone oil at 20.0 °C was calculated from the linear fit to be 922.13 ± 1.01 mm^{2}s^{-1}. The density of the silicone oil at 20.0 °C was measured using a hydrometer (BS718:1991 M100-101/04, Poulton, Selfe and Lee Ltd., Essex, UK), and found to be 975 ± 1 kgm^{-3}. The temperature inside the Mumetal shield was monitored using a mercury thermometer and the corresponding fluid viscosity was calcu-

lated for each individual experiment. The mean recorded temperature inside the shielding canister was found to be $T = 19.89 \pm 0.30$ °C. The viscosity of the fluid was calculated to be 924.14 ± 5.29 mm^{2}s^{-1} at a temperature of $T = 19.89 \pm 0.30$ °C.

In §5.4, the fluid was replaced by a more viscous silicone oil (Basildon Chemical Company Limited, Oxfordshire, UK) with a reported kinematic viscosity of $12,500$ cSt at 25 °C. The viscosity of the more viscous silicone oil was measured as a function of temperature using a rheometer (R/S Plus, Brookfield Engineering Laboratories, Massachusetts, USA) and a temperature-controlled water bath, as shown in the inset to Figure 2.3. The fit to the experimental data has the form $\nu = (-256.14\pm9.02)T + (1.8986\text{x}10^4 \pm 183.97)$ mm^{2}s^{-1}. Using this fit to the data the viscosity of the fluid was calculated for each experiment using the measured temperature value. The density of the fluid was also measured using a hydrometer and found to be 975 ± 1 kgm^{-3}. The viscosity of the fluid was calculated to be $(1.3976 \pm 0.0036)\text{x}10^4$ mm^{2}s^{-1} at the average measured temperature of $T = 19.56 \pm 0.08$ °C.

2.4   Applied Magnetic Field

Application of a magnetic field resulted in the motion of the active spheres submerged in the viscous fluid. The interaction of the applied magnetic field with the magnetic dipole of the sphere produced a magnetic torque which acted to align the dipole with the field. An alternating applied field could thus be used to control the torsional oscillations of a sphere containing a magnetic dipole. This novel set-up enabled the systematic study of the dynamics and interactions of spheres in a viscous fluid without the complications intro-
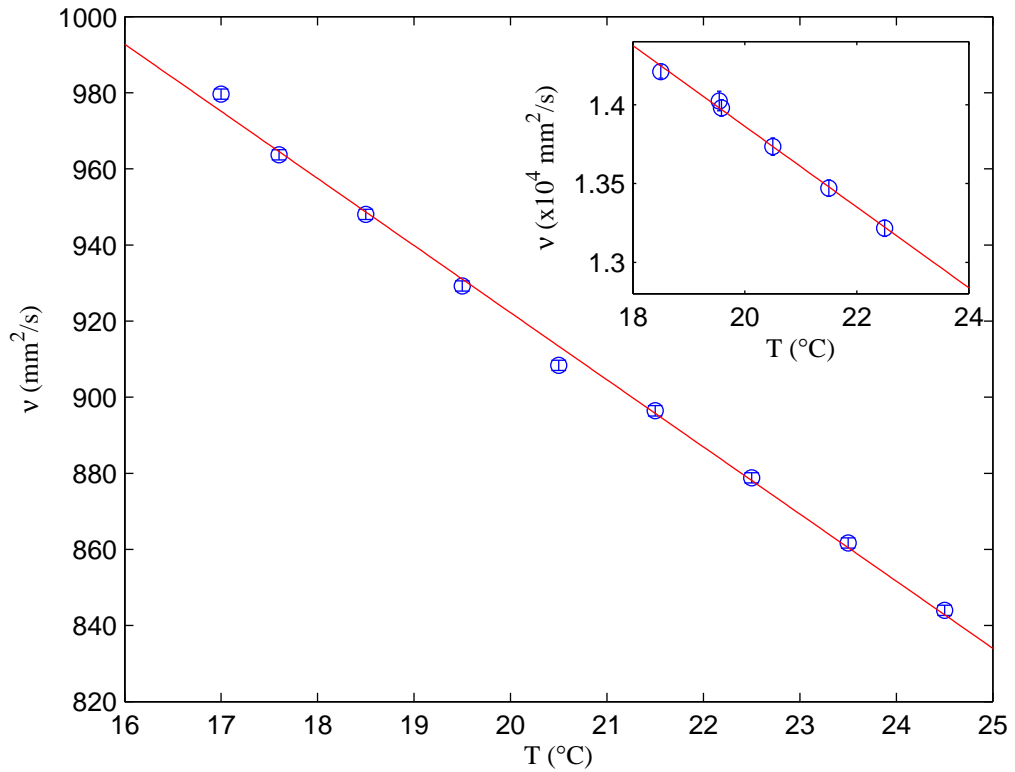
Figure 2.3: The kinematic viscosity of silicone oil measured as a function of temperature. A linear fit of the form $\nu = (-17.64 \pm 0.37)T + (1.275 \text{x} 10^3 \pm 7.71)$ mm^{2}s^{-1} was fitted to the data using the least-squares method. Inset: The kinematic viscosity of the more viscous silicone oil used in §5.4 measured as a function of temperature. A linear fit was fitted to the data and has the form $\nu = (-256.14 \pm 9.02)T + (1.8986 \text{x} 10^4 \pm 183.97)$ mm^{2}s^{-1}.

duced by a mechanical forcing mechanism which would require contact with the spheres. The dynamic response of an active sphere to an alternating field is documented in Chapter 3, and a suitable range of frequencies for experimentation is presented in §2.4.2. Calibration of the electromagnet and the Hall effect probes, and identification of a region of uniform magnetic field, was achieved using a steady field, and is detailed in §2.4.1.

Translational motion of the spheres was removed from the system by making both the driven and passive spheres neutrally buoyant in the viscous fluid. Furthermore, the magnetic dipole was aligned approximately horizontally when no magnetic field was applied. This meant that the magnetic dipole was initially aligned orthogonally to the applied field and was subjected to maximum magnetic torque. The sphere oscillated about this alignment when subjected to an alternating field.

The height and thickness of each Helmholtz coil was 140 mm and 35 mm respectively, and the gap between the two coils was 55 mm. The electromagnet inductance was 50 mH with a DC resistance of 0.36 ± 0.04 Ω. Shielding from background magnetic fields, such as the Earth's magnetic field, was achieved by placing the experimental system inside a Mumetal canister. Mumetal is a nickel-iron alloy with a magnetic permeability over 100 times greater than ordinary steel and shields by providing a path of low reluctance, and thus entraining magnetic flux. The Mumetal shield consisted of a 1.60 ± 0.02 mm thick cylindrical container, diameter and length of 510 mm and 520 mm respectively, with a lid and a base plate. Both the lid and base plate contained a centrally-located hole of 70 mm diameter through which cables could be passed to connect the experimental apparatus

to control boxes and a PC, and allowing for observations of the motion of the spheres. The magnetic field inside the Mumetal shield was measured using a Magnetometer and found to be one order of magnitude less than the background field in the laboratory. The background field in the laboratory was comparable to the geomagnetic field which varies from 25 to 65 μT [81], and the field strength within the shield was consistently found to be less than 5 μT.

2.4.1 DC Magnetic Field

A steady magnetic field was generated within the coils, parallel to the coil axis, by applying a current from a DC power supply. The power supply was connected to a DC coupled power amplifier and a 3 Ω resistor in series. The polarity of the constant magnetic field was altered by reversing the current of the circuit. A working region in which the generated field was uniform and the axial field strength was consistent to within 1% was identified using Hall effect probes. The region was cylindrical with 60 mm radius and height of 60 mm, located concentrically about the centre of the electromagnet. Within this region, the radial and azimuthal components of the magnetic field were measured to be consistently $\leq 1.5\%$ of the axial field for typical magnetic field strengths of $0.2 - 2$ mT used in experiments.

The magnitude of the magnetic field within the electromagnet was linearly proportional to the supplied direct current, as shown in Figure 2.4. The current was measured using an ammeter and the magnetic field strength in the axial direction was measured using a Gaussmeter. A linear fit was applied to the data giving $B = (0.878 \pm 0.001)I - (0.013 \pm 0.003)$ mT. All
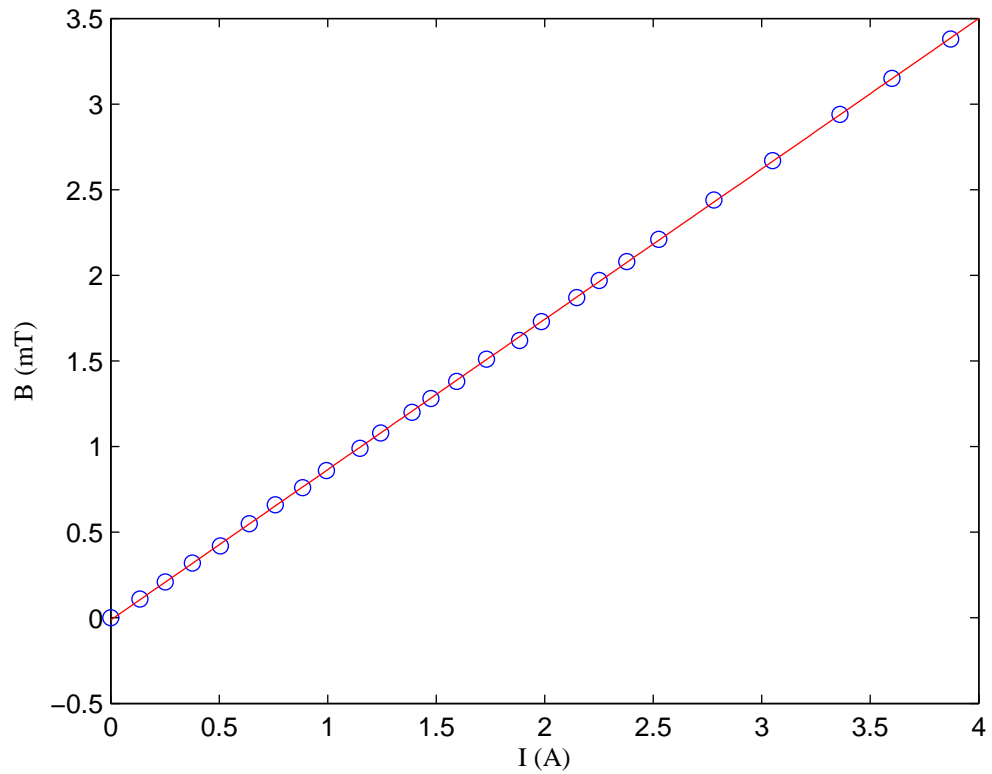
Figure 2.4: The magnetic field strength in the axial direction inside the Helmholtz coils, and within the uniform working region, measured as a function of the supplied DC current. The solid line is the least squares linear fit $B = (0.878 \pm 0.001)I - (0.013 \pm 0.003)$ mT. Errors on the data points are less than the size of the data markers.

reported values of the magnetic field strength refer to the axial component of the magnetic field, with positive magnetic field being directed vertically downwards.

Hall effect probes monitored the axial magnetic field strength within the Helmholtz coils. The Hall effect signal was logged using LabVIEW Signal Express (2012, National Instruments, Newbury, UK) via a 16-bit analogue-to-digital converter (NI USB-6212, National Instruments, Newbury, UK) at a sample rate of 1 kHz, orders of magnitude greater than the frequency of any alternating magnetic fields used. A second control probe was positioned outside the coils and shielded inside another smaller Mumetal canister of diameter 44 mm, height 104 mm and thickness 1.60 ± 0.02 mm. The signal from the secondary probe was subtracted from the first to remove background noise. The calibration of the Hall effect probe signal with the absolute, axial magnetic field strength is shown in Figure 2.5. The magnetic field was generated with a direct current and was measured using a Gaussmeter. A linear fit to the data takes the form $B = -(4.255 \pm 0.005)D - (0.006 \pm 0.002)$ mT, where D is the difference in voltage between the Hall effect probe within the working region of the electromagnet and the shielded, control probe. This calibration allowed calculation of the absolute magnetic field strength throughout the investigation.

2.4.2 AC Magnetic Field

Alternating magnetic fields were generated by supplying the Helmholtz coils with alternating current produced by a waveform generator. The impedance of the circuit for a signal with frequency ≤ 10 Hz is 3.36 ± 0.05 Ω. The alter-
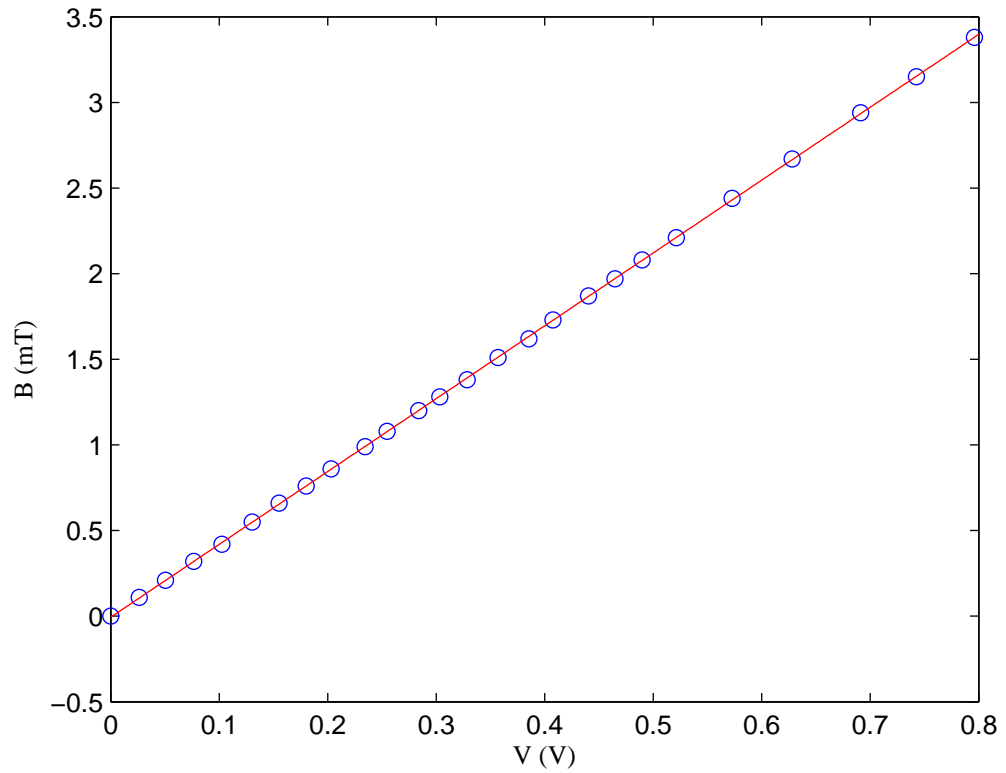
Figure 2.5: The magnetic field strength in the axial direction measured as a function of the Hall probe signal voltage. The solid line represents a linear, least-squares fit to the data of the form $B = -(4.255 \pm 0.005)D - (0.006 \pm 0.002)$ mT, where B is the magnetic field strength measured in the axial direction and D is the difference in voltage between the Hall effect probe within the working region of the electromagnet and the shielded control probe. Errors on the data points are less than the size of the data markers.

nating magnetic field could be used alone or superposed on top of a constant magnetic field by summing the DC and AC voltages prior to amplification. The effect of the frequency on the peak amplitude of the alternating magnetic field is shown in Figure 2.6. The peak amplitude of the axial magnetic field is constant for frequencies $0.01 < f < 4.00$ Hz and is consistent with the resultant field strength of a DC voltage equal to the AC peak voltage. However, the magnetic field strength rapidly decays with increasing frequency above 4 Hz.

2.5   Illumination and Observation

The spheres inside the tank were illuminated using two 400 mm strips of 36 Light Emitting Diodes (LEDs). The strips were attached to the inside surfaces of the upper and lower coils of the electromagnet to illuminate the working region from above and below. This set-up produced uniform illumination across the observable surface of the spheres. Furthermore, the rotational plane of the sphere was orientated to align with the observational plane using a laser-sheet. The motion of the spheres was recorded using a Genie camera (HM-1400, Teledyne DALSA, Ontario, Canada), with a spatial resolution of 1400x1024 pixels, which was positioned above the central hole of the lid of the Mumetal canister, as shown in Figure 2.1. The light leaving the tank was directed to the camera in a periscope-like manner via three mirrors (M1, M2 and M3), of width 76 mm and height 102 mm, positioned in between the electromagnet and the Mumetal canister. Mirror M1 was placed at 45° with respect to the side of the tank through which the spheres were observed. Mirrors M2 and M3 were adjusted in order to create an image at
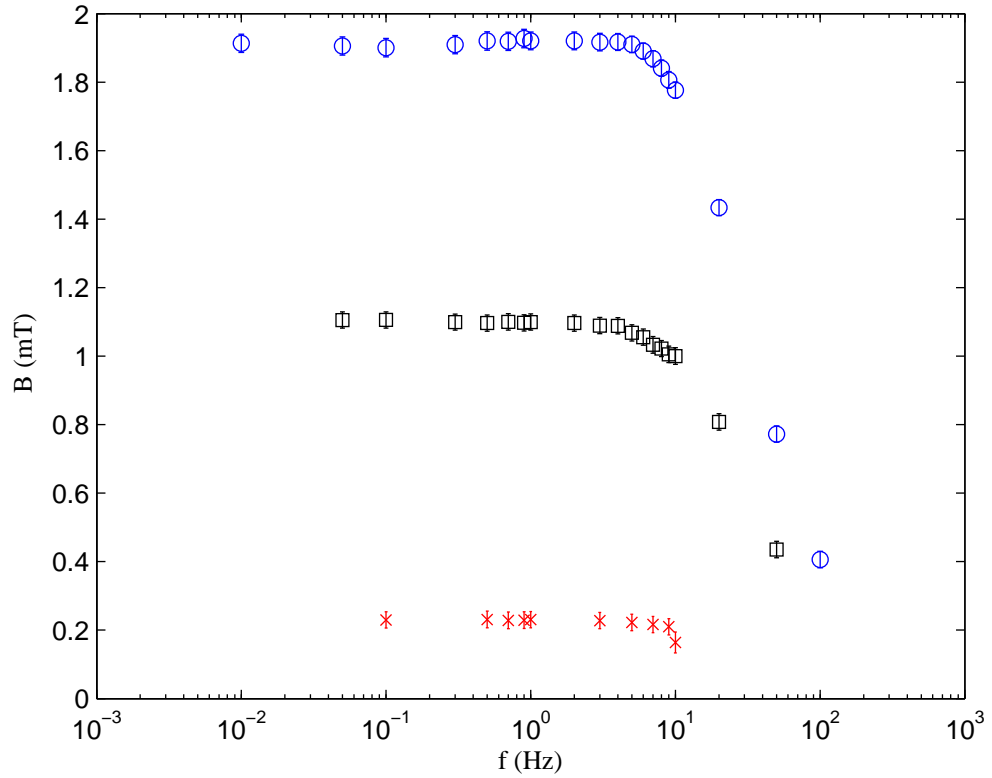
Figure 2.6: The peak-to-peak amplitude field strength inside the Helmholtz coils measured as a function of frequency of the field. The alternating magnetic field was generated by an AC signal. Measurements were taken for three different magnetic field amplitudes which corresponded to DC voltages of 9.0 V (o), 5.0 V (□), and 1.0 V (x). Error bars represent a 95% confidence limit calculated from a sinusoidal fit to the Hall effect probe signal.

the camera which was centered on the CCD sensor.

Analysis of the dynamic behaviour of the spheres involved tracking the motion of the spheres. Spheres used were coloured black with white markings, using permanent marker pens. Images of the spheres were processed using MATLAB software (R2011a, MathWorks Inc., Massachusetts, USA). Image contrast was enhanced to improve the accuracy of the thresholding, and the images were magnified for sub-pixel resolution. The white markings on the surface of the spheres were detected within the image using a Canny filter which initially smooths the image using a Gaussian filter before applying two thresholds to the image, one to detect and remove noise and one for edge detection of objects. Identification and labeling of spheres allowed for the removal of any further noise before the position and orientation of the spheres was determined. Tracking the motion of spheres throughout image sequences enabled the construction of a time-series of the dynamic response of the spheres to magnetic forcing and fluid interactions.

2.6   Flow Visualisation

Visualisation of the flow generated by the motion of the spheres required an adaptation of the experimental set-up, shown in Figure 2.7. The fluid was seeded with tracer particles, and a cross-section of the fluid was then illuminated using lasers and imaged using a high-speed camera. Analysis of the sequential images enabled determination of the fluid dynamics. The adaptation of the experimental apparatus is described in further detail in §2.6.1 prior to a discussion of the two flow visualisation techniques, Laser-Induced Fluorescence (LIF) and Particle Image Velocimetry (PIV), which

were used to study the flow generated by spheres.

Flow visualisation was conducted without the shielding Mumetal canister. The experimental system was therefore subject to the background magnetic field present in the laboratory. This external field was slowly-varying and comparable to the geomagnetic field. The dynamical behaviour of a sphere subject to both fields was similar to the behaviour of a sphere shielded from external fields and subject only to an applied field, as is discussed in further detail in Appendix A. The predominant effect of the external field was to align the magnetic dipole of the sphere in the direction of the external field and thus define the plane in which the sphere rotated. Observation of the flow was therefore conducted using a camera positioned orthogonal to this plane. Furthermore, the resultant fluid velocities were then characterised in terms of the velocity of the sphere surface, rather than in terms of the applied magnetic field.

2.6.1   Flow Visualization Equipment

A schematic diagram of the experimental apparatus used for flow visualisation is shown in Figure 2.7. Neutrally-buoyant, spherical microparticles (Fluostar particles, EBM Corporation, Tokyo, Japan) of 13.9 μm mean diameter were suspended in the viscous fluid and had a Rhodamine B coating so that they fluoresced under green-light laser illumination of wavelength 532 nm. A cross-section of the tank, corresponding to the rotational plane of the driven sphere, was illuminated using two green-light lasers. A continuous 50 mW laser sheet illuminated the cross-section from above, whilst a Nd:YAG pulsed laser illuminated the cross-section from below after being converted
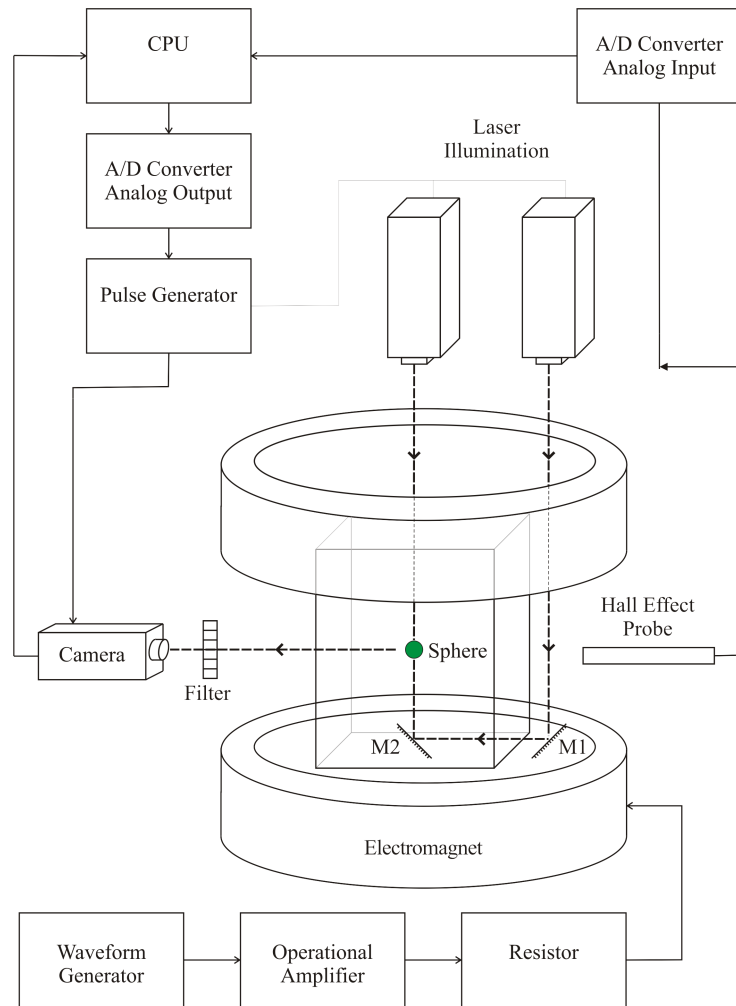
Figure 2.7: Schematic diagram of the experimental apparatus used for flow visualisation. Illumination of the rotational plane of the sphere was provided by lasers and an optical arrangements of mirrors (M1 and M2). A high-speed camera was positioned orthogonal to the illuminated plane and a low-pass filter was positioned between the tank and the camera to remove noise from the signal.

from a laser dot to a laser sheet by passing through a cylindrical lens. The Nd:YAG laser was positioned next to the 50mW laser, above the tank, and illuminated the cross-section from below after reflecting off two 45 degree mirrors, one positioned within the tank and one outside. A semi-cylindrical lens was used to reduce the width of the laser sheet to ≈ 1 mm to focus the illuminated plane on the centreline of the sphere. A low-pass filter was positioned between the tank and the camera to reduce background noise in the detected signal. A high-speed camera (pco.1200 hs, PCO AG, Kelheim, Germany) with a spatial resolution of 1280x1024 pixels was used to image the region of interest. The camera was positioned orthogonal to the illuminated plane, synchronised with the Nd:YAG pulsed laser using a pulse generator (BNC Model 500, Oxford Lasers Ltd., Oxon, UK) and imaged at a rate of 15 Hz, the maximum pulse-rate of the Nd:YAG laser, with an exposure of between 10 and 20 ms. Images captured by the camera were converted to 8-bit and a bandpass filter was applied to the images to remove noise and enhance signal strength. Pairs of consecutive images were then subject to sub-pixel Particle Image Velocimetry. Erroneous vectors in the resultant vector field were removed and any missing vectors in the field were interpolated using Laplace Equation Rearrangement.

2.6.2 Laser-Induced Fluorescence

Incorporating a dye into a fluid can allow visualisation of the flow field. Dilute fluorescent dye has the advantage that under normal lighting conditions it appears almost transparent, however, when illuminated by a light source of appropriate wavelength it fluoresces and becomes visible. Laser-Induced

Fluorescence (LIF) uses fluorescent dyes and thin laser-sheets to visualize internal flow structures. Rhodamine B is a fluorescent dye which, when illuminated by $\lambda \approx 532$ nm green light, emits an orange-coloured fluorescence. The tracer particles used in the flow visualisation experiments were coated with Rhodamine B and the observational plane was illuminated using green-light laser-sheets of $\lambda \approx 532$ nm. A camera positioned orthogonal to the laser plane observed an illuminated cross-section within the fluid and detected greater signal strength than would be detected using non-fluorescent tracer particles and normal lighting conditions [82].

Two types of flow seeding are commonly used in conjunction with LIF to identify flow structures and obtain measurements of internal flows [83]. Fluorescent tracer particles are often used in conjunction with sequential image processing to obtain quantitative measurements of the motion of the fluid. However, fluorescent dye can also be used to identify flow structures and obtain qualitative measurements from the intensity of the light pattern. Filters, such as the low-pass filter positioned in front of the camera, are often used in LIF experiments to reduce the background scatter from the walls of the experimental apparatus and to enhance the image quality before processing.

2.6.3   Particle Image Velocimetry

Digital image processing enables information to be extracted from a fluid flow. Scalar fields, such as the temperature and density of a fluid, and gradients of these fields are deducible from the colours and intensities present in an image. Observing the displacement of patterns in sequential images

provides information regarding the motion of a fluid. The motion of continuous patterns, such as the intensity of a dye, however, do not contain variations on all scales and therefore do not provide full spatial resolution in, for example, a turbulent flow. Furthermore, tracking the motion of individual, discrete particles in consecutive images is time consuming and prone to erroneous matching of particle-pairs, and is therefore conducted using low-density particle concentrations which also results in low spatial resolution. The spatial resolution can be improved by tracking patterns of particles. The particles are discrete and thus subject to the fluid motion on all scales. Tracking groups of particles, therefore, means that high-density particle concentrations can be used to achieve full spatial resolution without erroneous matching of particle-pairs. This technique of tracking the motion of particle patterns is known as Particle Image Velocimetry (PIV) and is used to " recover instantaneous 2- and 3-D velocity vector fields from multiple photographic images of a particle field within a plane or volumetric slab of a seeded flow, illuminated by a light source" [84], as shown in Figure 2.8.

The flow markers should follow the flow without affecting the physical properties of the fluid. For this reason, the seeding particles used were approximately 10 microns in size and had a similar density to the working fluid. The displacement of groups of flow markers from one image to the next is then determined to provide instantaneous velocity vectors. Estimates of the displacement of the particle patterns are determined by matching patterns in consecutive images.

Pattern-matching was conducted in a statistical sense by calculating the optimum, discrete cross-correlation between patterns in subsampled windows

59

of sequential images. A discrete cross-correlation calculated the sum of the product of the pixel-intensity in the relevant domain and was a maximum when a pattern-match occurs. It is formulated using $C(i', j') = \sum_{i=-k}^{k} \sum_{i=-l}^{l} f(i,j)g(i+i', j+j')$ where f and g are intensity values in sequential image windows, i and j are identified particle patterns in the original image, and i' and j' are their translated counterparts in the sequential image [84]. Images were divided into smaller interrogation windows and the cross-correlation was performed on these windows. The process can be considered to be a system which takes the particle pattern in the interrogation window of the first image as an input. The system applies a displacement function and a noise function to this input, and then outputs the particle pattern in the window of the next image. The displacement function results from the flow, while the noise may result from the particles exiting the interrogation window or the illumination plane, or the inherent noise in the images. The cross-correlation peak was used to identify the best match between input and output windows and helped locate sub-pixel correlation peaks which improved the accuracy of the process. The displacement of the particle pattern was estimated, and the instantaneous velocity of fluid within the sample window was calculated. The cross-correlation process was performed on interrogation windows throughout the entire image to construct a velocity vector field of the fluid motion within the illuminated cross-section, an example of which is given in Figure 2.8(a).

The determination of erroneous vectors within this vector field may result in the calculation of incorrect differential or integrable quantities, such as shear. Errors result from incorrect correlations, the 3-D motion of particles
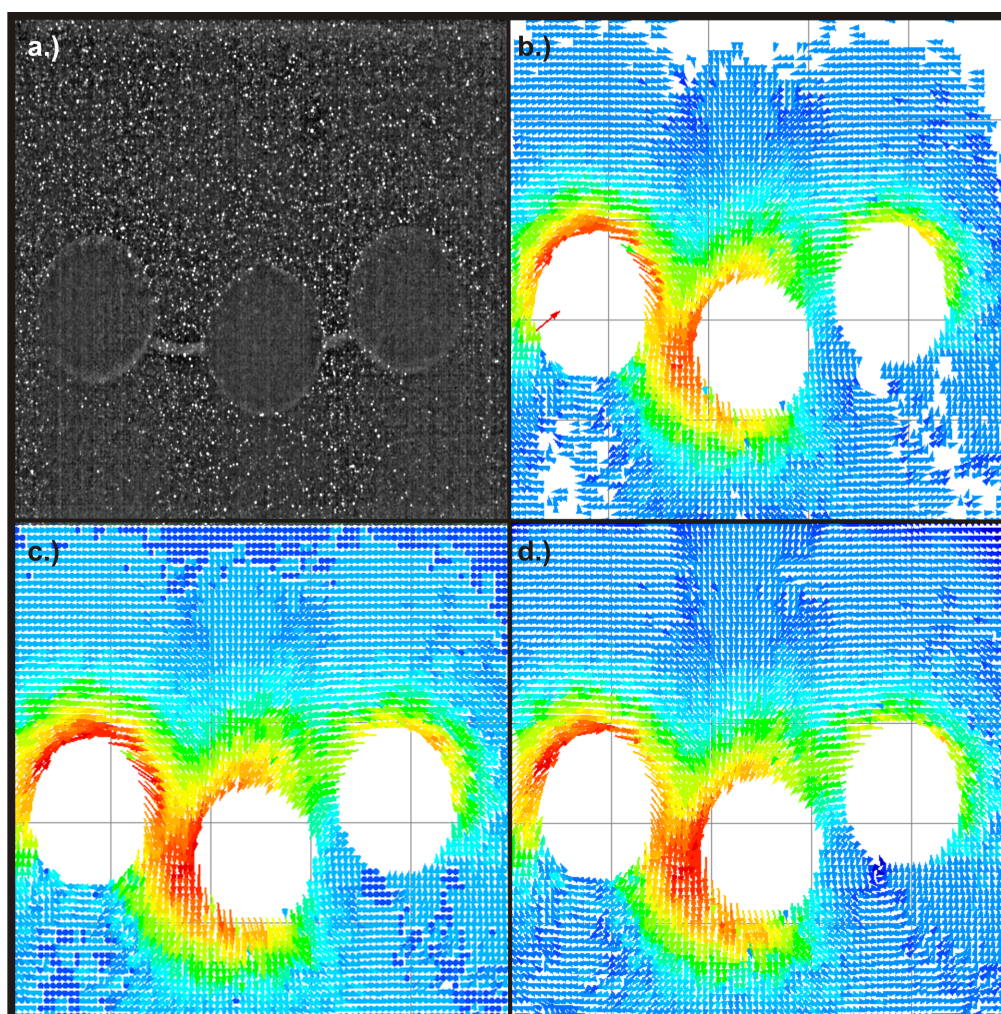
Figure 2.8: The Particle Image Velocimetry method. (a) Sequential image pairs are subject to a bandpass filter to remove noise and enhance signal strength. (b) Discrete cross-correlation maps the translation of patterns of tracer particles between images producing a vector field. The direction and magnitude of the vectors is denoted by the orientation and colour of the depicted arrows. (c) Erroneous vectors are removed (and missing vectors are flagged with blue dots in this instance). (d) Laplace Equation Rearrangement is used to interpolate the values of missing vectors from neighbouring vectors.

out of the illuminated plane, and the non-uniform seeding of the flow. To remove erroneous vectors from the velocity field, each vector was compared to its nearest neighbours and if the difference exceeded a threshold then the vector was removed, see Figure 2.8(c). Any resulting holes in the vector field which resulted from this erroneous vectors removal, or the lack of particles in the input/output interrogation windows, were filled by interpolating the surrounding vectors using, for example, Laplace Equation Rearrangement (LER), as shown in Figure 2.8(d).

Uncertainties in the cross-correlation technique adopted by PIV result from the concentration and size of the seeding particle and the size of the interrogation window used to subsample the original image. A high density of tracer particles within an interrogation window means more particles contribute to the statistical cross-correlation. A high concentration of seeding particles, a small particle image size, and a large window size thus reduce uncertainties in the cross-correlation. The cross-correlation assumes a linear shift of the particle pattern from the input window to the output window and does not take into account second order effects, such as the velocity gradient within the window. This velocity gradient within the window may also produce a bias towards lower velocities as faster-moving particles exit the window. A optimum window of 50x70 pixels was found to be small enough to minimise the velocity gradient in the flow but large enough to contain sufficient particles for a statistically sound cross-correlation.

Chapter 3

One Sphere

This Chapter contains a description of the dynamic response and the flow field around a single sphere which is driven by an oscillating magnetic field. A review of the applications of magnetic spheres driven by external magnetic fields is presented in §3.1. The torques involved in generating the dynamic response of a single, neutrally buoyant sphere containing a magnetic dipole is described in §3.2. In §3.3, the equations of motion governing the dynamics of a sphere in an oscillating magnetic field are presented. The torsional response of the sphere to an applied, alternating magnetic field is studied as a function of the dimensionless magnetic torque, Γ, and the dimensionless gravitational torque, $\hat{\epsilon}$, in §3.4. Finally, the results of an investigation using flow visualisation of the fluid motion generated by the rotary motion of a sphere are presented in §3.5.

3.1 Applications of Driven Magnetic Micro-Spheres

The fluid flow generated by a magnetic sphere in a viscous fluid subject to an applied magnetic field has a variety of industrial and biomedical applications. Although the following applications utilised micro-particles composed entirely of magnetic material, rather than macro-particles containing magnets, analogies can still be drawn with the system considered in this work and thus potential applications envisaged.

The rotational fluid flow generated by a magnetic micro-sphere driven by an external rotating magnetic field can propel passive micro-objects, and therefore be used for precise non-contact manipulation and long-range transportation of micro-objects. Multiple micro-manipulators in parallel create reconfigurable, virtual micro-fluidic channels for concurrent, non-contact transportation of multiple micro-objects [85]. Similarly, the hydrodynamic flow generated by paramagnetic colloidal particles subject to an external, rotating magnetic field has been used as a micro-stirrer to mix colloidal suspensions [86]. The synchronous and asynchronous rotation of a magnetic micro-sphere subject to an external rotating magnetic field has been studied and the nonlinear rotation rate, which occurs above a critical frequency of driving magnetic field, can be used to detect and monitor bacterial growth [87, 88].

As well as being used to mix fluids and manipulate micro-objects, the hydrodynamic forces generated by the motion of a magnetic sphere subject to an applied magnetic field can also be used to measure rheological properties of the fluid [53]. This includes non-invasive *in vivo* viscosity measurements [51].

Furthermore, with the advent of nanotechnology, magnetic nano-particles (MNPs) and colloidal suspensions of magnetic particles have been utilised in a wide range of biomedical applications [89] [90]. The controlled manipulation, through the application of external magnetic fields, and the size compatibility of MNPs with biological cells mean they are an important tool in both *in vitro* and *in vivo* applications. *In vitro* applications include the detection, separation and monitoring of biological species, and blood purification. *In vivo* applications include Magnetic Resonance Imaging (MRI), site-specific drug delivery and treatment of hyperthermia [91].

3.2   Driven Sphere Dynamics

The dynamic response of a sphere, containing a magnetic dipole, to an applied magnetic field is considered. A schematic of the coordinate system used in the development of a model is shown in Figure 3.1(a). The orientation of the rotational plane of the sphere was controlled to be orthogonal to the observer so that $\phi = 0$, where ϕ is the angle between the magnetic-dipole axis of the sphere and the line-of-sight of the observer - the x-axis. A projection of the coordinate system in the observed plane is shown in Figure 3.1(b). Figure 3.1(b) also indicates the direction of gravity, g, the direction of the applied magnetic field, B, and the position of the effective magnetic dipole within the spheres. The orientation of the magnetic dipole of the sphere with zero applied field is approximately horizontal in the eyes of the observer, $\theta \sim 0$ degrees where θ is the angle of the magnetic-dipole axis of the sphere from the y-axis.

Application of a steady magnetic field introduces a magnetic torque which
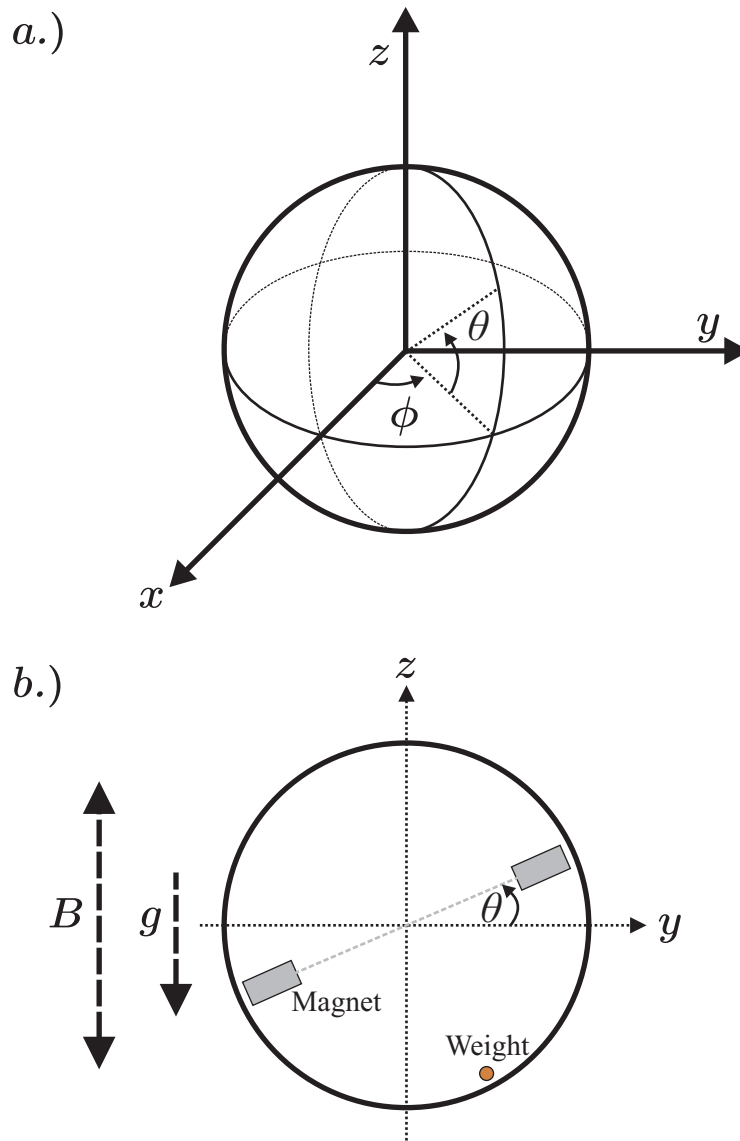
Figure 3.1: (a) A schematic of the coordinate system, and (b) a projection of the coordinate system onto the observed plane. The projection of the coordinate system also includes indications of the direction of the applied magnetic field, B, which induces a magnetic torque on the magnets embedded in the sphere, and the direction of gravity, g, which induces a torque on the non-uniform mass distribution within the sphere.

acts to align the magnetic dipole of the sphere with the applied field. The torque acting on the dipole causes the sphere to rotate in a clockwise or anti-clockwise direction depending on the direction of polarity of the magnetic axis of the sphere. The convention is that application of a magnetic field in the z-direction acts to align the magnetic dipole of the sphere at $\theta = 90°$. On reversal of the applied field, the magnetic torque reverses and acts to align the magnetic dipole of the sphere in the opposite direction. Through application of an alternating magnetic field, the sphere can be made to perform torsional oscillations with an amplitude and a frequency determined by the magnitude and frequency of the applied field.

3.3   Equations of Motion

The equation of motion for the dynamic response of a sphere subject to an applied magnetic field can be deduced from a combination of the viscous, gravitational and magnetic torques acting on the sphere:

$$8\pi\mu a^3 \frac{d\theta}{dt} = -\epsilon \sin\theta + Bm \sin\omega t \cos\theta, \qquad (3.1)$$

where μ is the dynamic viscosity of the fluid, a is the radius of the sphere, B is the magnetic field strength, m is the magnetic moment of the magnetic-dipole of the sphere, ω is the angular frequency, θ denotes the orientation of the magnetic axis of the sphere in the observational plane and ϵ is the gravitational torque which acts to return the sphere towards the zero applied field orientation at $\theta \sim 0$. The gravitational torque, ϵ, results from gravity acting on the non-uniform distribution of mass within the sphere. A non-dimensional time, based on the angular frequency ω of the applied oscillatory

67

field, can be defined as $\hat{t} = \omega t$. Equation 3.1 then becomes

$$\frac{d\theta}{d\hat{t}} = -\frac{\epsilon}{8\pi\mu a^3\omega}\sin\theta + \frac{Bm}{8\pi\mu a^3\omega}\sin\hat{t}\cos\theta. \tag{3.2}$$

Dimensionless parameters which quantify the ratio of the gravitational torque and the magnetic torque to the viscous torque acting on the sphere are thus defined by:

$$\hat{\epsilon} = \frac{\epsilon}{8\pi\mu a^3\omega}, \quad \Gamma = \frac{Bm}{8\pi\mu a^3\omega}, \tag{3.3}$$

respectively. Γ is therefore the inverse of the dimensionless Mason number which quantifies the typical ratio of hydrodynamic to magnetic torque [92].

This Ordinary Differential Equation (ODE) for θ can thus be written as

$$\frac{d\theta}{d\hat{t}} = \hat{\epsilon}\sin\theta + \Gamma\sin\hat{t}\cos\theta. \tag{3.4}$$

If the neutrally buoyant sphere had a uniform distribution of mass then the gravitational torque acting on the sphere would be negligible, $\hat{\epsilon} = 0$. When $\hat{\epsilon} = 0$, Equation 3.4 reduces to a separable ODE which can be solved for the dimensionless parameter Γ as a function of the total angular displacement $\Delta\theta = \theta_{max} - \theta_{min}$. This has the solution

$$\Gamma = \ln(\sec(\Delta\theta/2) + \tan(\Delta\theta/2)). \tag{3.5}$$

When $\hat{\epsilon} \neq 0$, as in the experiments, an exact analytic solution is no longer obtainable and the ODEs need to be solved numerically to find $\Delta\theta$ as a function of Γ and $\hat{\epsilon}$.

A numerical model of the experiment was developed by Dr. Alice Thompson[1] and implemented in MATLAB (R2011a, Mathworks, Massachusetts,

---

[1]Manchester Centre for Nonlinear Dynamics, University of Manchester, UK.

USA). The author used the model to solve the boundary value problem and calculate the total angular displacement of the sphere for dimensionless parameters which corresponded to the experimental values. A comparison was then made between the numerical and experimental results. Numerical simulations enabled the testing of experimentally unobtainable conditions, such as negligible gravitational torque. When $\hat{\epsilon} = 0$, an infinite family of periodic solutions to the governing equations of motion exists depending on the initial conditions of the system, such as the initial angle of the magnetic dipole of the sphere θ_0. Whereas, when $\hat{\epsilon} \neq 0$, all solutions converge onto a single stable periodic solution.

When gravity is negligible, and thus $\hat{\epsilon} = 0$, parallel alignment of the magnetic dipole of the sphere with the applied field is attainable. However, for non-zero $\hat{\epsilon}$, gravity acts on the non-uniform mass distribution within the sphere inducing a torque which acts to return the sphere to the zero-field orientation at $\theta \sim 0$. A greater magnetic torque is thus required to align the magnetic-dipole axis of the sphere with the applied field. Large $\hat{\epsilon}$ implies large gravitational torque and/or low-frequency applied field, and can significantly reduce the angular displacement of the sphere. This particular feature of the system will be discussed in greater depth in §3.4.4.

3.4 Dynamic Response of the Sphere

The dynamical response of the driven sphere was studied both experimentally and numerically and good agreement was found between the two sets of results. In the experiments, the sphere was subjected to a gravitational torque which was measured using the method outlined in §3.4.1. Further

experimental specifics relevant to the response of a single, free sphere are then detailed in §3.4.2. The dynamic response of the neutrally buoyant sphere in a viscous fluid to magnetic and gravitational forcing is discussed in §3.4.3 and §3.4.4, respectively.

3.4.1 Gravitational Torque

The effects of gravity were always present in the experiments and therefore the gravitational torque acting on the sphere could not be neglected, $\hat{\epsilon} \neq 0$. A non-zero $\hat{\epsilon}$ meant that a gravitational torque acted on the sphere to return the driven sphere to the zero-field angle which was $\theta \sim 0$ through careful embedding of weights into the sphere. A non-zero $\hat{\epsilon}$ also meant that greater magnetic torque was required to align the magnetic-dipole axis of the sphere with the applied field.

In order to characterise the dynamic response of a sphere to the applied field an empirical measure of the gravitational torque acting on the sphere was required. A simple test involved the rate at which the sphere returns to the zero-field position at $\theta \sim 0$ when released from a non-zero angle. In the absence of any forcing, $\Gamma = 0$, the equations can be separated. In this case, the analytic solution to Equation 3.4 is

$$\int_{\theta_A}^{\theta_B} \frac{1}{\sin\theta} d\theta = -\frac{\epsilon}{8\pi\mu a^3}(t_B - t_A). \qquad (3.6)$$

ϵ can therefore be determined by introducing a single (dimensional) time-scale T_0 so that

$$\int_{\theta_A}^{\theta_B} \frac{1}{\sin\theta} d\theta = -\frac{t_B - t_A}{T_0}. \qquad (3.7)$$

70

Exact integration of the left-hand side of the above equation gives

$$\ln \left| \frac{\csc\theta_B - \cot\theta_B}{\csc\theta_A - \cot\theta_A} \right| = \frac{t_A - t_B}{T_0}. \tag{3.8}$$

This means, if θ is small, the angle should decay exponentially to the unforced position at $\theta \sim 0$ according to $\theta \propto \exp(-t/T_0)$. Once T_0 is known, ϵ and $\hat{\epsilon}$ can be calculated according to

$$\epsilon = \frac{8\pi\mu a^3}{T_0}, \quad \hat{\epsilon} = \frac{1}{\omega T_0}. \tag{3.9}$$

Empirical estimates of the gravitational torque were obtained by measuring the decay of the angular position of a sphere from an offset position to the zero-field state on sudden removal of the magnetic forcing. The approach to the zero-field position was approximated by an exponential decay from which a time-scale associated with the gravitational torque term could be extracted.

A large (~ 2.2 mT) steady magnetic field was applied initially in order to attain approximate alignment with the applied field. Sudden removal of the applied field led to the rotation of the sphere back to the zero-field position under the influence of gravity. The time-scales associated with the capacitance falling in the electromagnets were orders of magnitude faster than the time-scale associated with the gravitational torque and were therefore neglected.

A time-series of the angular position of the sphere was obtained from an initial angle of $\lesssim 30°$ to the zero-field orientation, $\theta \sim 0$, under the influence of gravity, as shown in Figure 3.2 (top). A least-squares fit to the data has the form $\theta = 28.21e(-t/4.56) + 3.09$, from which a time-scale associated with the gravitational torque of 4.56 s was extracted. A decay

from $< 30°$ was considered sufficiently small to validate the use of the small-angle approximation which determines the decay to be exponential in form.

An accurate estimate of the time-scale associated with the gravitational torque was obtained by calculating the mean of 20 measurements. The gravitational torque term was measured for each sphere used in the investigation as individual spheres had unique, non-uniform distributions of mass, a result of the ubiquitous embedding of magnets and weightings, which led to specific gravitational torque terms.

3.4.2 Experimental Details

The particular sphere used throughout the experiments reported in this Chapter had a diameter of 15.86 ± 0.01 mm and contained a pair of diametrically opposed neodymium magnets. After the inclusion of the magnets, and the careful embedding of weights, the density of the sphere was $978.53 \pm 3.8 \mathrm{x} 10^{-3}$ kgm^{-3} and, when subject to zero-field, the magnetic dipole axis of the sphere was orientated approximately orthogonal to the applied field direction; in particular, at an angle of $3.22 \pm 0.77°$ from the horizontal position. The time-scale associated with the gravitational torque acting on the sphere was $T_0 = 4.67 \pm 0.03$ s, where the quoted error is the standard deviation of 20 measurements. A uniform, alternating magnetic field was applied in order to study the angular response of the sphere from this position. The amplitude and frequency ranges of the applied field were varied from 0 to ~ 2.5 mT and from $0.01 - 4$ Hz, respectively.
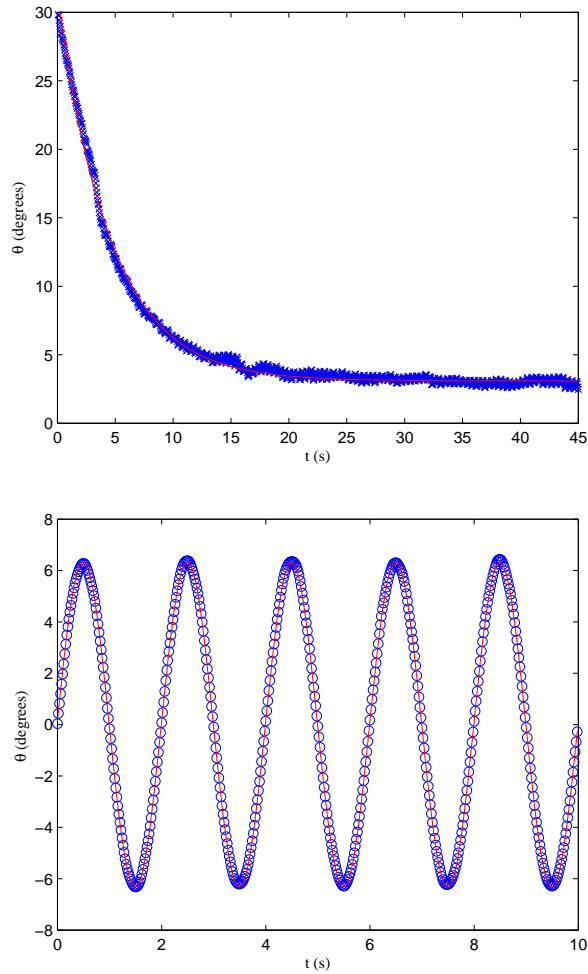
Figure 3.2: (top) A time-series of the angular position of the magnetic-dipole axis of the sphere measured as a function of time as the sphere rotates back to the zero-field orientation under the sole influence of gravity. A least-squares fit to the data has the form $\theta = 28.21e(-t/4.56) + 3.09$ and is depicted by the red line. (bottom) A time-series of the angular position of the magnetic-dipole axis of the sphere when driven by an applied field with a frequency $f = 0.5$ Hz into performing small-amplitude torsional oscillations throughout four periods of oscillation. A least-squares fit to the experimental data has the form $\theta = 6.48\sin(2\pi ft + 0.32)$.
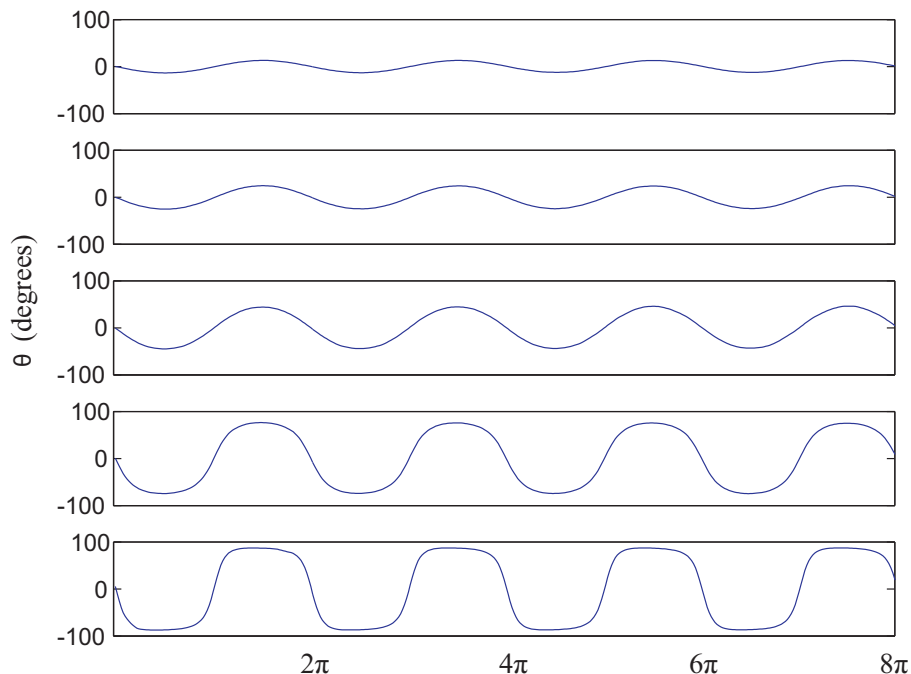
Figure 3.3: Experimental time-series of the angular displacement of the driven, magnetic sphere over four periods of oscillation, for $\Gamma = 0.21$, 0.41, 0.82, 2.07, 4.95 (top-to-bottom). The response of the sphere deviates increasingly from the form of the sinusoidal drive with increasing Γ.

3.4.3 Dynamic Repsonse to Magnetic Torque

In the experiments, the effect of the magnetic forcing was separated from that of the gravitational forcing by investigating the response of the sphere to magnetic fields of different amplitude whilst maintaining a constant frequency of applied field of 0.15 Hz. The gravitational torque term $\hat{\epsilon}$ was kept constant yet non-zero ($\hat{\epsilon} = 0.22$).

Small Γ resulted in small-amplitude, sinusoidal oscillations of the sphere which matched the sinusoidal form of the applied field i.e. the response was

linearly proportional to the drive. The sinusoidal form of the response to the applied field was validated by fitting a sinusoidal function to the data using the least-squares method, see Figure 3.2 (bottom). A time-series of the angular position of the magnetic-dipole axis of the sphere when performing small-amplitude torsional oscillations throughout four periods of oscillation is shown. The data shown in Figure 3.2 (bottom) was obtained for an applied field with a frequency $f = 0.5$ Hz and a least-squares fit to the experimental data has the form $\theta = 6.48 \sin(2\pi f t + 0.32)$. The standard deviation of the difference between the measured angular position and the fitted function provides an estimate of the quality of the fit and the deviation of the response from the sinusoidal form of the drive. For increasing Γ, the amplitude of the oscillation increased as greater magnetic torque resulted from increased field strength B. Furthermore, the response of the sphere deviated increasingly from a sinusoidal form as alignment of the magnetic axis with the applied field in both directions was approached.

Examples of experimental time-series of the angle of the sphere over four periods of oscillation are shown in Figure 3.3, for $\Gamma = 0.21, 0.41, 0.82, 2.07$ and 4.95 (top-to-bottom), which corresponds to applied magnetic fields of amplitude 0.112 ± 0.015, 0.224 ± 0.015, 0.448 ± 0.015, 1.122 ± 0.015 and 2.688 ± 0.015, respectively. The phase delay between the response of the sphere and the applied magnetic field decreased monotonically from $\pi/2$ for an frequency of 2 Hz to $\sim \pi/4$ at 0.05 Hz. For oscillations of amplitude less than $19°$, the standard deviation between fitted function and data was less than 0.1%. Oscillations of amplitude less than $19°$ were therefore considered to be small-amplitude torsional oscillations of a sinusoidal form.

However, larger amplitude oscillations were also well-approximated by a sinusoidal function; for oscillations of amplitude less than 45°, the standard deviation between the data and the least-squares fitted function was less than 1%.

Large Γ resulted in a nonlinear response of the sphere as the magnetic dipole attained alignment with the applied field, saturating the angular response at $\pm 90°$, and remained in that position until the field reversed direction. The slight asymmetry evident in the sphere response for larger Γ, evident in Figure 3.3, results from the non-zero contribution from the gravitational torque $\hat{\epsilon}$ which acts to reorientate the sphere from the aligned position to the zero-field position.

The total angular displacement of the sphere $\Delta\theta$ was calculated as a function of the dimensionless magnetic torque parameter Γ for $\hat{\epsilon} = 0.22$ from the time-series of the angle of the sphere and is shown in Figure 3.4. The blue circles and solid black line represent the experimental data and the numerical results respectively. The total angular displacement saturates at $\sim 180°$ (depicted by the dashed, red line in Figure 3.4) which represents the sphere rotating from alignment with the applied field in one equilibrium position to alignment in the opposite orientation on reversal of the effective field direction. Below a critical torque Γ_c, the total angular displacement of the sphere is attenuated in a manner analogous to the attenuation of a signal by a high-pass filter [93].

The total angular displacement of the sphere $\Delta\theta$ was investigated as a function of both the magnetic torque Γ, and the gravitational torque $\hat{\epsilon}$, and is shown as a function of Γ in Figure 3.5 for $\hat{\epsilon} < 0.396$. Numerical calculations
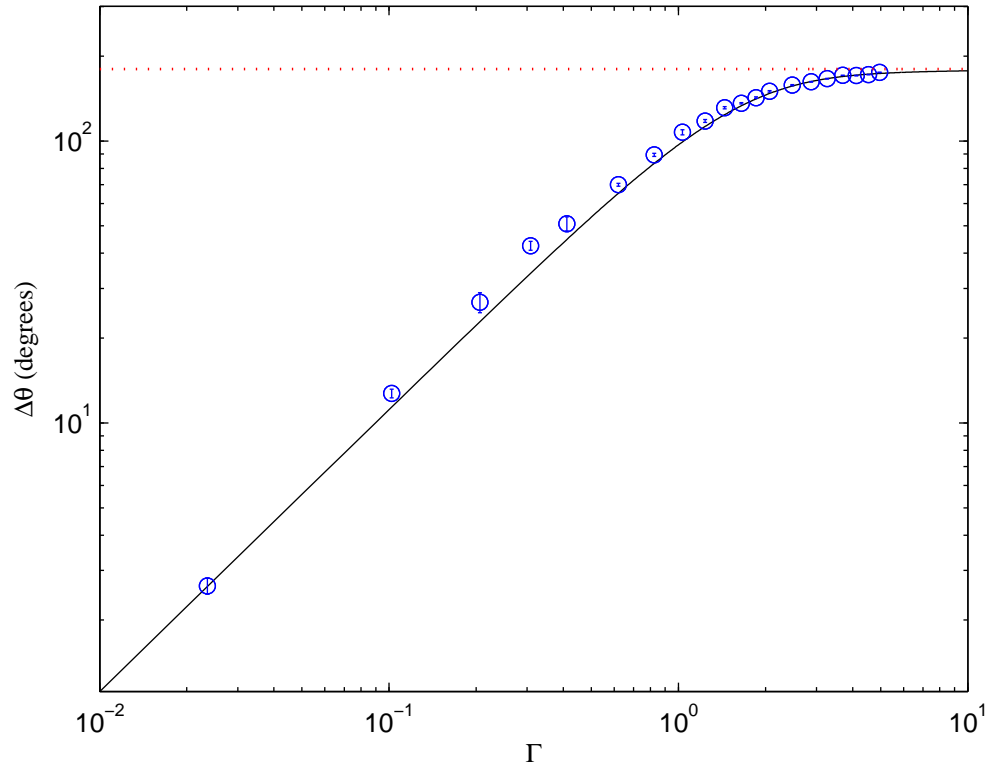
Figure 3.4: The total angular displacement of the sphere measured as a function of the dimensionless magnetic torque parameter Γ for $\hat{\epsilon} = 0.22$. Experimental data is denoted by the blue circles and the black line represents numerical calculations, while the dashed, red line depicts a total angular displacement of 180°.
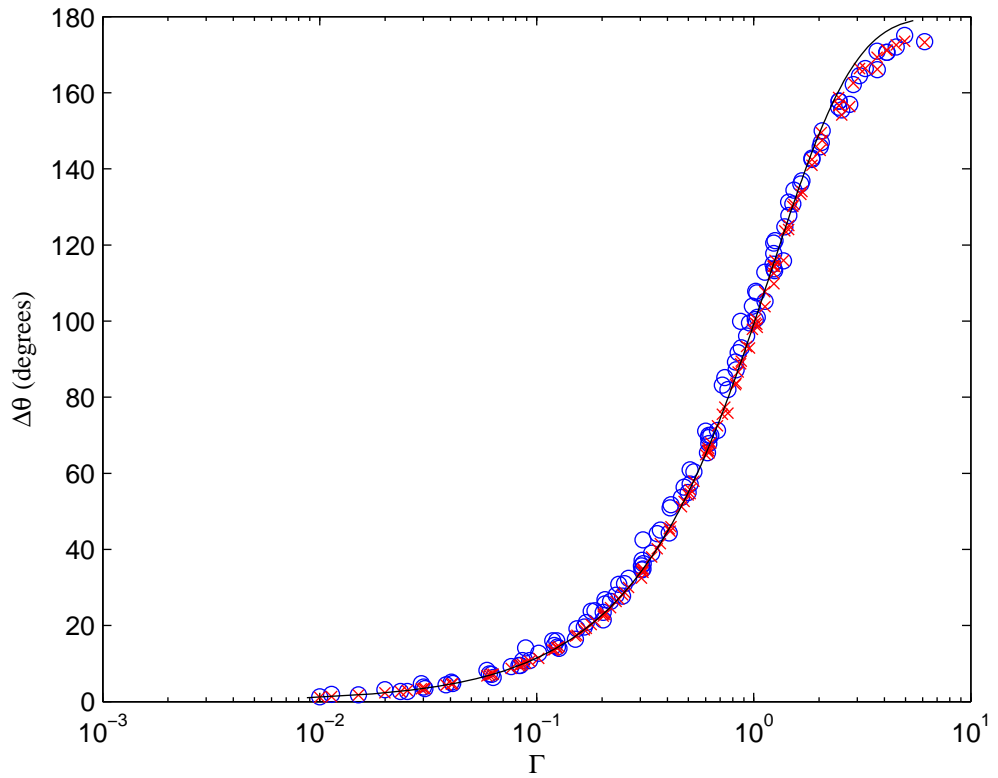
Figure 3.5: The total angular displacement of the sphere measured as a function of the magnetic torque parameter Γ for $\hat{\epsilon} < 0.396$. Blue circles represent the experimental data and red crosses represent the numerical solutions evaluated at the corresponding parameters. The black line represents the analytic solution for the case when the gravitational torque acting on the sphere is zero, $\hat{\epsilon} = 0$.

determined that for $\hat{\epsilon} > 0.396$ the dynamics of the sphere were significantly altered by the gravitational torque acting on it as significantly greater magnetic torque was required to attain comparable angular displacement of the sphere, see §3.4.4. The experimental data is represented in Figure 3.5 by the blue circles, with corresponding numerical calculations represented by the red crosses, and the analytic solution to the governing equations of motion obtained for $\hat{\epsilon} = 0$ (see Equation 3.5), depicted by the solid black line. Error bars on the experimental data points have not been included to aid visual clarity. There is good agreement between the experimental and numerical findings. Characterising the response of the sphere in this manner enabled determination of a applied field regime in which the sphere executes small-amplitude torsional oscillations of a sinusoidal form.

3.4.4 Dynamic Repsonse to Gravitational Torque

A non-zero $\hat{\epsilon}$ results from the non-uniform distribution of mass within the sphere and acts to return the sphere to the zero-field orientation at $\theta \sim 0$. An increase in $\hat{\epsilon}$ means that an increase in Γ is required to attain comparable angular saturation of the sphere. The effect of a non-zero $\hat{\epsilon}$ is to reduce the angular displacement at which the sphere response saturates by acting to return the sphere to the zero-field position. This results in the deviation of the experimental data and numerical results from the analytic solution, derived for $\hat{\epsilon} = 0$, around an angular displacement of $\sim 180°$, as shown in Figure 3.5.

The dynamic response of the sphere to changes in $\hat{\epsilon}$ at constant Γ is analogous to the response of the sphere to changes in Γ for constant $\hat{\epsilon}$. When

Γ is constant, a small $\hat{\epsilon}$ results in a sinusoidal small-amplitude response of the sphere. Increasing $\hat{\epsilon}$ increases the amplitude of the oscillation and the deviation of the response from the sinusoidal form of the applied field. An increase in $\hat{\epsilon}$ represents an increase in the timescale of the oscillating applied field which means that the induced magnetic torque acts on the sphere for longer before the field and the rotation direction reverses.

Good quantitative agreement also exists between experimental measurements and numerical calculations for $\hat{\epsilon} > 0.396$, as can be seen in Figure 3.6. The results shown in Figure 3.5 have been used to construct Figure 3.6 but now include numerical results obtained as a function of Γ for $\hat{\epsilon} = 1.33$ (green line) and $\hat{\epsilon} = 3.34$ (magenta line), and experimental data obtained for $\Gamma > 0.396$ and various values of $\hat{\epsilon}$. The results clearly show that for constant Γ, a large $\hat{\epsilon}$ significantly reduces the total angular displacement of the sphere because gravity acts to return the sphere to the zero-field position. Therefore, for increasing $\hat{\epsilon}$, greater magnetic torque is required to attain alignment with the applied field in both directions. For $\hat{\epsilon} > 0.396$, the maximum angular displacement which the sphere can attain is significantly reduced when compared to a response which attains approximate alignment with the applied field in both directions. The value of $\hat{\epsilon} = 0.396$ was determined by initially computing the required Γ which ensured $\Delta\theta$ was within 1% of the maximum response of 180° when $\hat{\epsilon} = 0$, this was found to be $\Gamma = 4.85$. The $\hat{\epsilon}$ for which $\Delta\theta$ was reduced by 5% of the maximum possible displacement of 180° was deemed to be significant, was calculated for $\Gamma = 4.85$ and determined to be $\hat{\epsilon} = 0.396$.
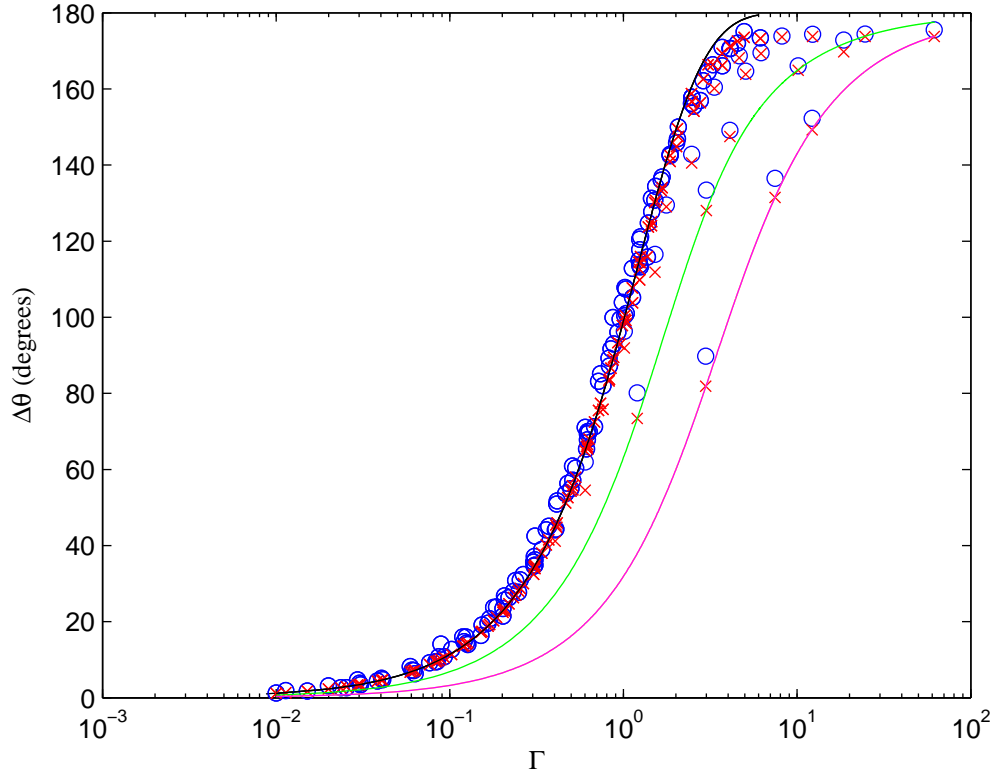
Figure 3.6: The total angular displacement of the sphere measured as a function of the magnetic torque parameter Γ. Blue circles represent the experimental data and red crosses represent the numerical solutions evaluated at the corresponding parameters. The black line represents the analytic solution for the case when the gravitational torque acting on the sphere is zero, $\hat{\epsilon} = 0$. The green and magenta lines represent to numerical results obtained with $\hat{\epsilon} = 1.33$ and $\hat{\epsilon} = 3.34$, respectively

81

3.5   Fluid Dynamics

The application of an alternating magnetic field induces torsional oscillation of a single, active sphere in a viscous fluid. In order to visualise the fluid flow generated by the motion of the sphere, a camera was positioned parallel to the axis of rotation and two-dimensional Particle Image Velocimetry (PIV) was conducted using the equipment and methods documented in §2.6.1. An instantaneous velocity vector field obtained at $3\pi/10$ in the oscillation cycle of the sphere is shown in Figure 3.7. The sphere was rotating in the clockwise direction which induced rotation of the surrounding fluid in the same direction. The velocity vectors are represented by arrows, the colour of which denotes the magnitude of the velocity which ranges from 0 mms^{-1} (dark blue) to 8 mms^{-1} (dark red). The velocity vector field shows that the velocity of the fluid is greatest close to the surface of the sphere and decreases with radial distance from the sphere surface.

Instantaneous particle paths were determined from the experimentally measured flow field using the graphical software Tecplot 360 (2011, Tecplot Inc., Washington, USA). Furthermore, particle paths were computed from the analytical solution for the fluid velocity generated by the steady rotation of a sphere in an unbounded, incompressible viscous fluid [21]:

$$v = \frac{\Omega a^3}{r^2} sin\phi \tag{3.10}$$

where Ω is the angular velocity of the sphere, a is the sphere radius, r is the radial distance from the centre of the sphere and ϕ is the angle measured from pole-to-pole. Measurements were conducted in the equatorial plane and therefore $sin\phi = 1$. The experimental and analytical instantaneous particle paths produced at $3\pi/10$ in the oscillation cycle of the sphere are shown in
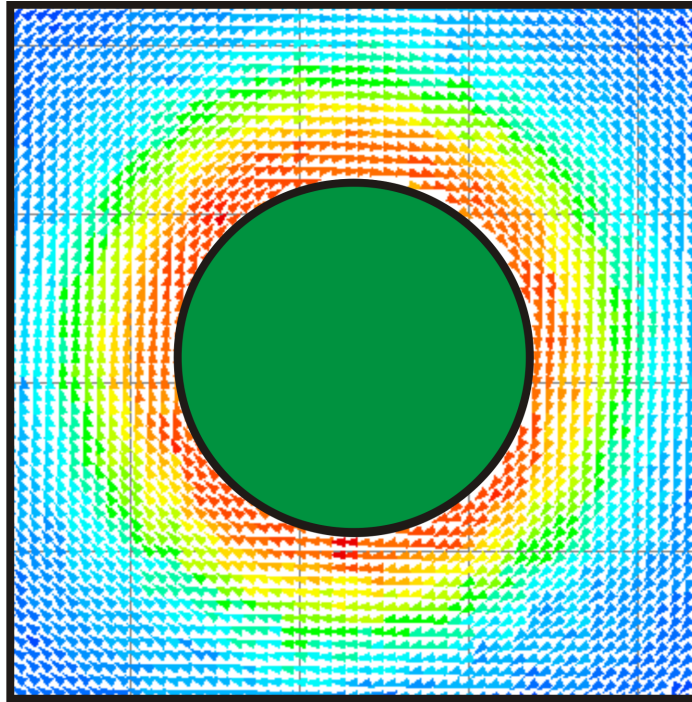
Figure 3.7: A typical velocity vector field depicting the flow generated by a spherical particle rotating, in the clockwise direction, in a viscous fluid. The instantaneous velocity field was measured using Particle Image Velocimetry at $3\pi/10$ in the oscillation cycle. The green circle in the centre of the image denotes the sphere. The vectors are represented by coloured arrows, the magnitude of which ranges from 0 mms^{-1} (dark blue) to 8 mms^{-1} (dark red).

Figure 3.8, and good agreement was obtained. Particle paths illustrate the trajectories particles would follow if placed in the fluid. In the case shown in Figure 3.8, if the velocity field was steady (i.e. due to a sphere rotating with constant angular velocity) then a marker placed in the fluid on one of the particle paths would circle the sphere indefinitely.

The magnitude of the fluid velocity, v, is a function of radial distance from the sphere centre, r, and was calculated from the experimental vector fields. The observed symmetry of the flow about the axis of rotation of the sphere enabled spatial averaging around $360°$ of the vector field. This was conducted at various points in the oscillation cycle for a sphere oscillating with a frequency of 0.15 Hz. The fluid velocity was then normalised by the corresponding instantaneous velocity of the sphere surface, v_S. The resultant dependence of the fluid velocity on radial distance is shown in Figure 3.9, measured at phase positions of $2\pi/10$, $3\pi/10$, $4\pi/10$, $5\pi/10$, and $6\pi/10$ in the oscillation cycle. Apart from the weak divergence of the data with increasing radial distance, which was attributed to a reduction in the amount of resolved fluid velocities, the collapse of the data onto a single curve indicates that the flow at any instant corresponds to the case for a body moving uniformly with the given instantaneous velocity. This provides experimental confirmation that the observed phenomena occurs in the low-frequency, Stokes flow limit in which the velocity varies only slowly with time and the flow can be regarded as steady at any given instant [94]. The fluid velocity resulting from the torsionally oscillating sphere can therefore be justifiably compared with the analytical solution of the fluid velocity for a sphere rotating with constant angular velocity.
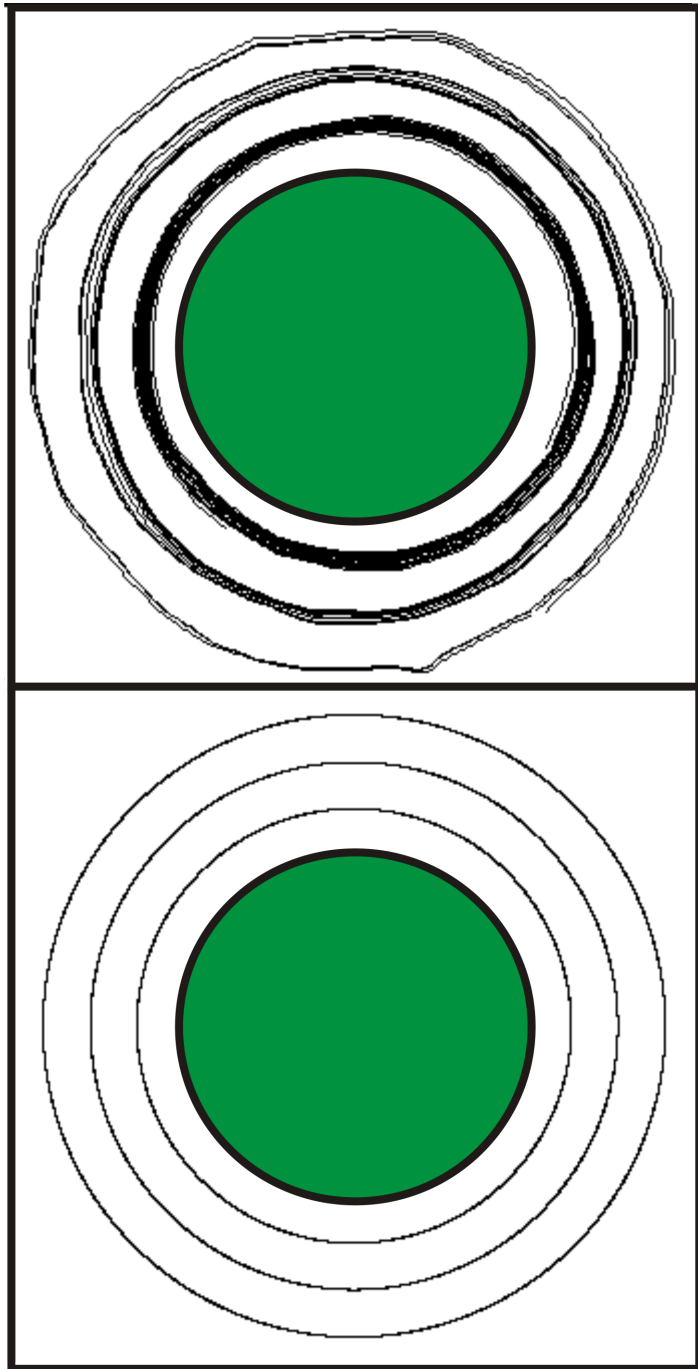
Figure 3.8: Experimental particle paths derived from the instantaneous velocity vector field (top), and analytical particle paths (bottom). The green circle in the centre of both images corresponds to the sphere.
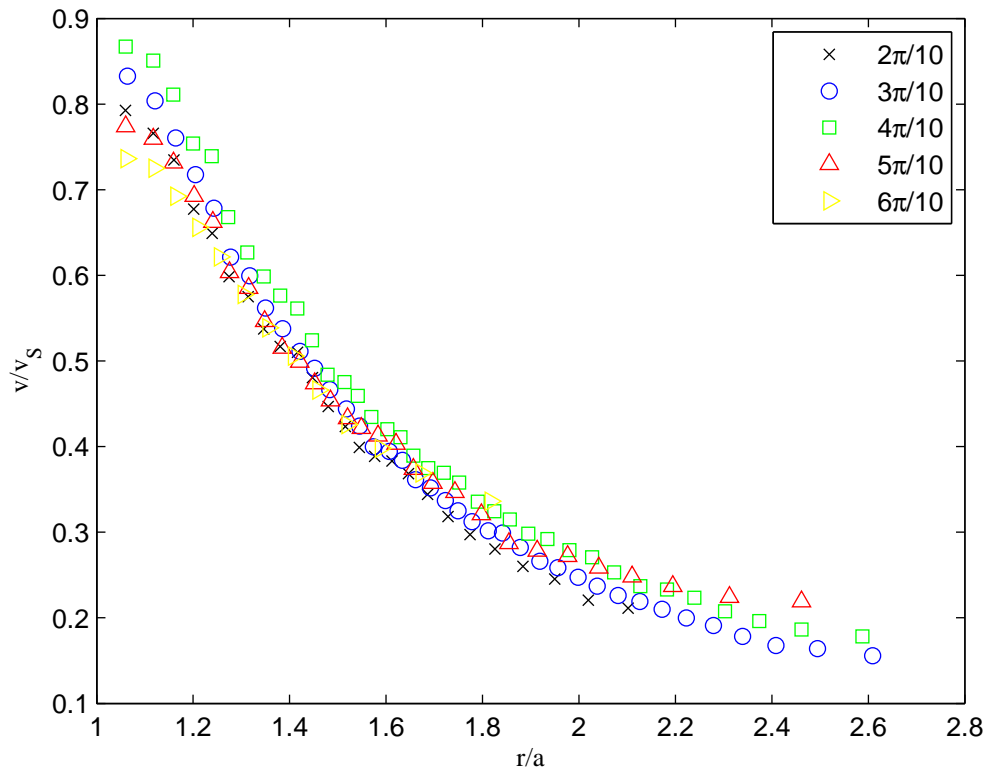
Figure 3.9: The fluid velocity measured as a function of radial distance at $2\pi/10$, $3\pi/10$, $4\pi/10$, $5\pi/10$, and $6\pi/10$ in the oscillation cycle. The fluid velocity has been normalised by the instantaneous velocity of the surface of the sphere. The collapse of the data onto a single curve confirms that the phenomena is in the low-frequency, Stokes flow limit.

The empirically measured fluid velocity resulting from the slow, low-frequency torsional oscillations of a sphere and the fluid velocity calculated from the analytical solution for a sphere undergoing steady rotation, given by Equation 3.10, are both shown in Figure 3.10. The experimental data points shown in Figure 3.10 were obtained at $3\pi/10$ in the oscillation cycle and are represented by the blue data points, while the black curve represents the analytical solution. In both instances, the fluid velocity has been normalised by the velocity of the surface of the sphere. The errors on the data points represent the standard deviation of the measurements. Good quantitative agreement is found between the experimental and analytical fluid velocity as a function of radial distance. The consistent underestimation of the measured fluid velocity is attributed to the finite width of the laser-sheet illumination. The significant deviation of the experimental data from the analytic solution close to the sphere results from specular reflections by the surface of the sphere which, prior to diffusing, illuminate tracer particles that are not on the equatorial plane. The marginal reduction in agreement at a radial distance $\gtrsim 2a$ is attributed to the influence of the boundaries of the tank containing the viscous fluid which were $\sim 8a$ from the centre of the sphere. The influence of solid planar boundaries on the flow and the driven sphere dynamics will be the subject of the following Chapter.
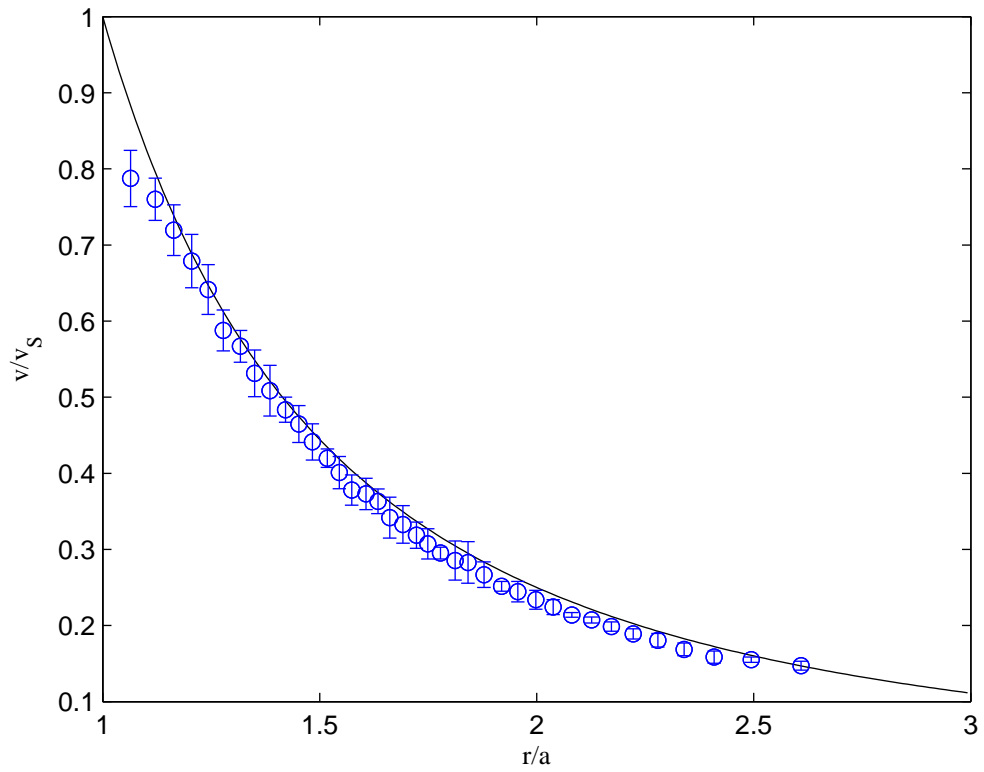
Figure 3.10: The fluid velocity measured as a function of radial distance. The fluid velocity has been normalised by the surface velocity of the sphere. The blue data points represent the experimental velocity, the standard deviation of which is given by the error bars. The black curve is the analytic solution for the fluid velocity due to a sphere rotating with constant angular velocity in an infinite fluid [21].

3.6 Summary

A neutrally buoyant sphere with a magnetic-dipole axis and a non-uniform mass distribution was submerged in a viscous fluid and subject to an unsteady magnetic field. The dynamic response of the sphere was to perform torsional oscillations about the zero-field position of the magnetic-dipole axis. A simple balance of the magnetic, gravitational and viscous torques acting on the sphere enabled identification of two non-dimensional parameters which determined the behaviour of the sphere: Γ, which resulted from the interaction of the magnetic dipole of the sphere and the applied field and acted to align the magnetic-dipole of the sphere with the applied field; and $\hat{\epsilon}$ which resulted from gravity acting on the non-uniform mass distribution within the sphere and acted to return the magnetic-dipole of the sphere to the zero-field position. The zero-field position of the magnetic axis of the sphere was approximately at $\theta = 0$ because of careful embedding of the weights used to achieve neutral buoyancy of the sphere. The response of the sphere to an applied field was investigated experimentally and numerically and good agreement was found between the empirical data and the numerical results.

The flow generated by the motion of the sphere was then studied in the equatorial plane and found to move in arcs along a circular trajectory around the sphere, the direction of which was determined by the rotation of the sphere. The fluid velocity was found to have a functional dependence on the radial distance from the sphere, decreasing with increasing radial distance. Instantaneous measurements of the fluid velocity throughout the torsional oscillation cycle confirmed that the phenomena occurred in the low-frequency, low-Reynolds number regime in which the flow can be regarded as steady at

any given instant. Good agreement was found between experimental measurements of the fluid velocity around the sphere and the analytical solution of the functional dependence of the fluid velocity on radial distance from a sphere performing steady rotational oscillations in an infinite, viscous fluid. The experiments were, however, conducted in a finite-sized tank filled with viscous fluid, in which the bounding edges of the container could have influenced the generated flow and the dynamic response of the sphere to the applied field. An investigation into the effects which arise when solid, planar boundaries are introduced into the system is described in the following Chapter.

Chapter 4

One Sphere: Boundary Effects

A discussion of the dynamic response of a single sphere in a large volume of viscous fluid subjected to an unsteady magnetic field, and the flow generated by the motion of the sphere was presented in the previous Chapter. In this Chapter, the influence of a nearby solid, planar boundary on both the flow field and the dynamic response of the sphere to the applied field was investigated in two cases; when the axis of rotation was (1) parallel to and (2) perpendicular to the surface normal of the boundary. Experimental details regarding the measurement of the sphere-wall separation are outlined in §4.1. The boundary effects, which arose when parallel and perpendicular planar boundaries were introduced into the system, are then discussed in §4.2 and §4.3 respectively.

4.1 Experimental Set Up

The orientation of the rotation of the sphere with respect to the boundary is described using the convention shown in Figure 4.1. When the axis of

rotation was parallel (perpendicular) to the surface normal of the boundary then the primary flow generated by the rotation of the sphere was in the plane parallel (perpendicular) to the boundary. In the experiments reported in this Chapter, the sphere was made to perform small-angle sinusoidal, torsional oscillations. The sphere-wall separation distance, h, was measured from the centre of the sphere to the boundary, along a line normal to the boundary. The thickness of the Stokes layer on the surface of the sphere, $\delta \sim \left(\frac{\nu}{\omega}\right)^{1/2}$, was measured radially from the surface i.e. from $r = a$, where r is the radial distance from the centre of the sphere and a is the radius of the sphere. The Stokes layer, also known as an oscillatory boundary layer, gives an estimate of the penetration depth of the fluid motion generated by the oscillations of the sphere [94]. The penetration depth is defined as a measure of the distance over which the amplitude of fluid motion decays exponentially to $1/e = 0.37$, of the initial value.

A Perspex plate of width 109 mm ($= 13.8a$), height 253 mm ($= 31.9a$) and thickness 11 mm ($= 1.4a$) was placed in the tank containing the viscous fluid held by a clamp stand. The transparent edges of the plate were blackened so that they could be detected in images which aided the measurement of the separation distance. When the rotational axis of the sphere was parallel to the normal to the surface, the boundary was less easily distinguished in the plane of illumination. Therefore, to obtain the separation distance, an image of the system was captured from above using a Nikon D300 SLR camera, with a spatial resolution of 0.0552 mm/pixel. When the rotational axis of the sphere was perpendicular to the surface normal, the boundary was evident in the illuminated plane and the separation distance was measured
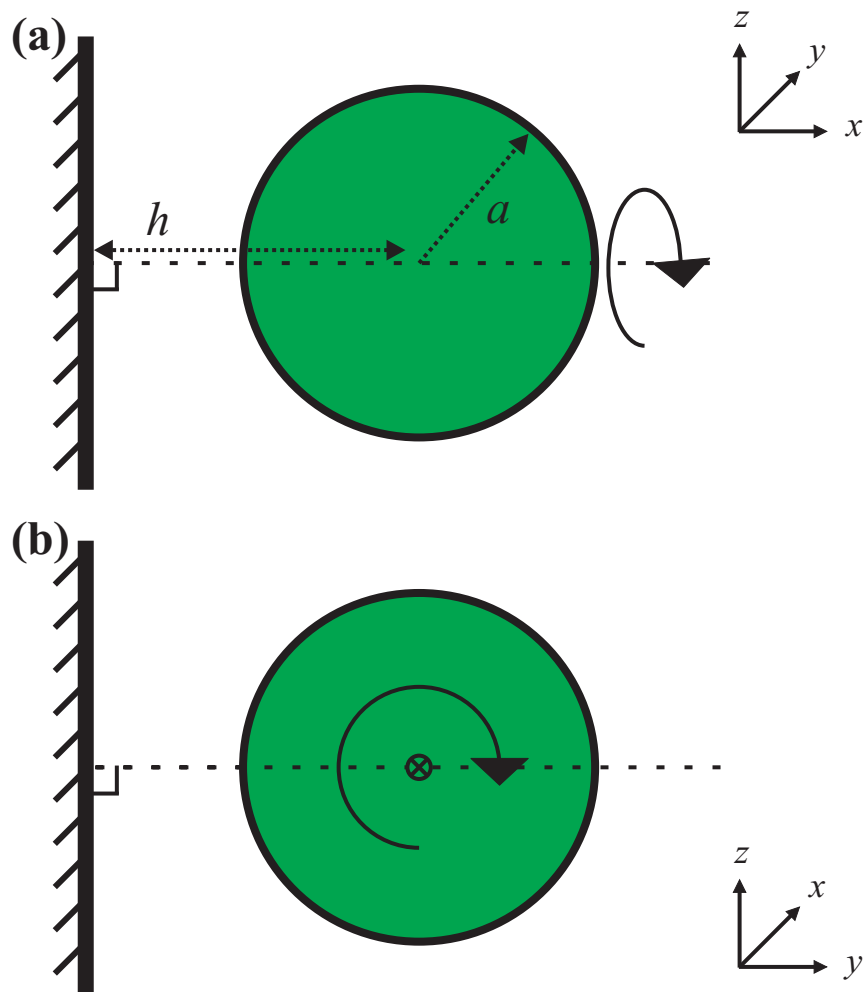
Figure 4.1: Schematic diagram of the orientation of the rotational motion of the sphere with respect to the bounding plane. The solid boundary is denoted by the thick line on the left-hand side of the image, the surface normal to the boundary is denoted by the horizontal dashed line to which the rotational axis of the sphere is (a) parallel and (b) perpendicular. The sphere-wall separation distance, h, is measured from the centre of the sphere to the surface of the boundary. The normal to the surface of the boundary is depicted by the dashed, black line. The rotation direction is depicted by the curved, black arrow and the radius of the sphere, a, is depicted in (a). The same figure is shown in Chapter 1.6 and has been reprinted here.

from images captured by the GenieCam/PCO camera used for observation.

The particular sphere used in the experiments in this Chapter was different to that used in the experiments reported in Chapter 3. The density of the sphere was $986.67 \pm 3.8\text{x}10^{-3}$ kgm^{-3}, the characteristic gravitational timescale associated with the gravitational torque acting on the sphere was $T_0 = 3.14 \pm 0.05$ s, and the magnetic-dipole axis of the sphere sat at an angle of ~ 5.6 degrees from the horizontal for zero applied field. Measurements of the instantaneous fluid velocity were performed, using the PIV technique outlined in §2.6.1, at various sphere-wall separation distances in the range $1.3 - 2.5a$. The influence of the boundary on the flow are presented in the following sections and discussed with reference to changes in the dynamic response of the sphere.

4.2   Parallel Boundary

For oscillations of a sphere about an axis parallel to the surface normal of a planar wall, PIV measurements were performed in the equatorial plane of the sphere at sphere-wall separations of $h = 2.44a$, $2.12a$, $1.84a$, $1.46a$, and $1.31a$. The results were compared with the effectively unbounded case discussed in Chapter 3 for which the distance between the centre of the sphere and the container walls was $\sim 8a$. For all sphere-wall separations, the flow in the equatorial plane was qualitatively the same as the unbounded case with fluid moving in arcs prescribed by concentric circles around the axis of rotation. The fluid moved in a direction which was determined by the instantaneous rotation of the sphere and with a velocity which decreases with increasing radial distance from the sphere. As in the case of the unbounded sphere,

Figure 4.2: The fluid velocity measured as a function of radial distance from the centre of the sphere for separation distances $h = 8a$, $2.44a$, $2.12a$, $1.84a$, $1.46a$, and $1.31a$ from a planar, parallel boundary.

the observed symmetry of the flow around the rotational axis allowed the velocity to be calculated, as a function of radial distance, by averaging over $360°$ of a velocity vector field.

The instantaneous fluid velocity, v, measured as a function of radial distance, r, is shown in Figure 4.2 for the aforementioned sphere-wall separation distances. The fluid velocity was measured at various phases in the oscillation cycle. The results obtained at $3\pi/10$ in the oscillation cycle were considered to be typical and are depicted on the Figure. Error bars correspond to the

standard deviation of the measurements of fluid velocity. The magnitude of the fluid velocity decreases with decreasing sphere-wall separation which suggests that, in addition to other forces, a resistive hydrodynamic torque was introduced into the system by the boundary which increased as the sphere was placed closer to the boundary. The symmetry of the primary flow about the rotational axis was not broken and therefore the functional dependence of the measured fluid velocity on radial distance was qualitatively similar for all separation distances.

The effect of the boundary on the dynamic response of the sphere was investigated by measuring the amplitude of torsional oscillations, θ_A, as a function of separation distance, h, for $\Gamma = \frac{Bm}{8\pi\mu a^3\omega} = 0.1213 \pm 0.0003$, $\hat{\epsilon} = \frac{\epsilon}{8\pi\mu a^3\omega} = 0.1011 \pm 0.0002$, and a drive frequency of 0.5 Hz, as shown in Figure 4.3. The red, dashed line indicates the Stokes layer thickness $\delta \sim (\frac{\nu}{\omega})^{1/2} = 2.16a$ measured from the sphere surface at $r = a$. When the boundary was separated from the centre of the sphere by a distance greater than the Stokes layer thickness, $h > \delta + a \sim 3.16a$, the effects of the boundary on the driven sphere dynamics were negligible and the amplitude of torsional oscillation was independent of sphere-wall separation distance. For $h < \delta + a$, the planar boundary intersects the Stokes layer and the effects of the no-slip condition on the stationary boundary, which ensures that the velocity reduces to zero at the boundary, become significant. As the sphere was moved towards the boundary, the amplitude of oscillation decreased until it was approximately 1 degree less than for the unbounded case. The reduction in amplitude results from increased viscous effects induced by the boundary, which act to oppose the magnetic torque driving the sphere. Effectively, the sphere has to drag

96
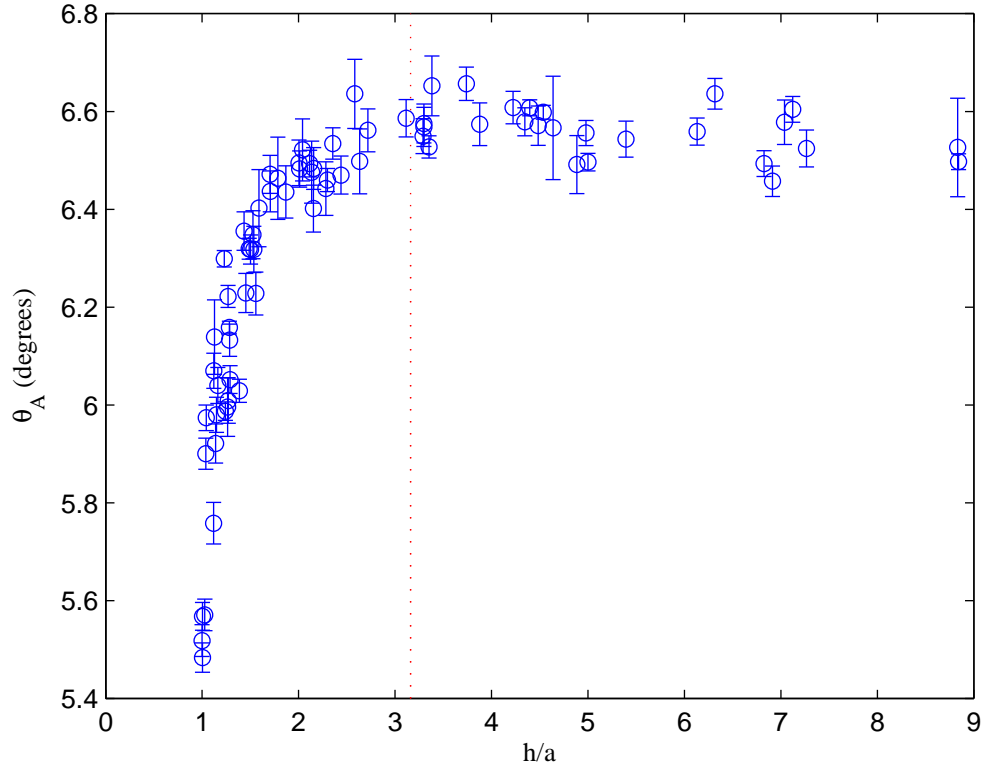
Figure 4.3: The amplitude of torsional oscillation measured as a function of separation distance from a parallel, planar boundary for $\Gamma = 0.1213 \pm 0.0003$, $\hat{\epsilon} = 0.1011 \pm 0.0002$, and a drive frequency of 0.5 Hz. The error bars denote the standard deviation of the measurements and the red, dashed line depicts the extent of the Stokes layer, the thickness of which is $\delta \sim 2.16a$, measured from the sphere surface at $r = a$.

fluid across the surface of the planar boundary and this viscous shear effect suppresses the torsional oscillation of the sphere.

The fluid velocity data obtained from the PIV measurements was normalised by the instantaneous surface velocity of the sphere, v_S. The functional dependence of the fluid velocity on radial distance is qualitatively the same for various separation distances, as shown in Figure 4.4. This suggests both the fluid and the sphere are subject to a hydrodynamic torque which arises from viscous effects introduced by the boundary. Furthermore, the viscous torque resists the fluid motion and the rotation of the sphere, and the effect increases with decreasing separation distance. Although all the data shown in Figure 4.2 collapses on to a single curve, only the data obtained at sphere-wall separations of $2.44a$, $1.46a$, $1.31a$ and the unbounded case, for which $h \sim 8a$, are presented in Figure 4.4 for visual clarity. The error bars on the experimental data points represent the standard deviation of the measurements. The effects of the introduction of a perpendicular boundary into the system are now examined.

4.3 Perpendicular Boundary

When the rotational axis of the sphere was perpendicular to the surface normal of the planar boundary, the boundary intersects the plane of the primary flow generated by the motion of the sphere. Therefore, when in close proximity to the boundary, the flow generated by the sphere was significantly altered. The fluid velocity was constrained to zero on the surface of the boundary as a consequence of the no-slip condition and the primary flow was no longer axisymmetric about the rotational axis of the sphere. The
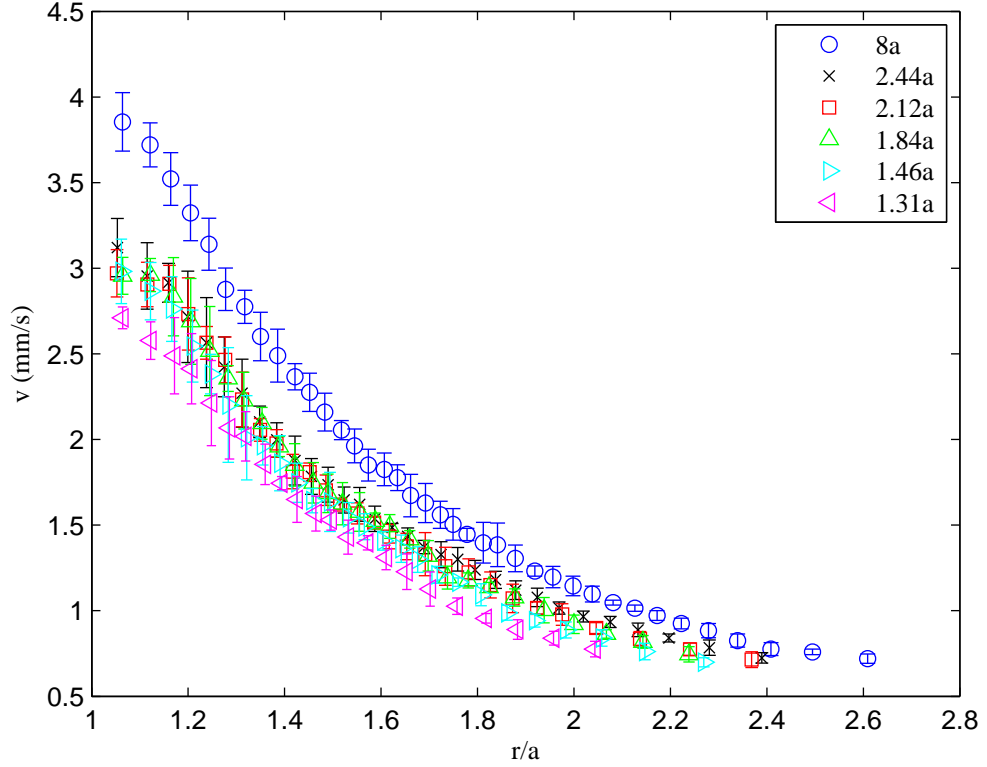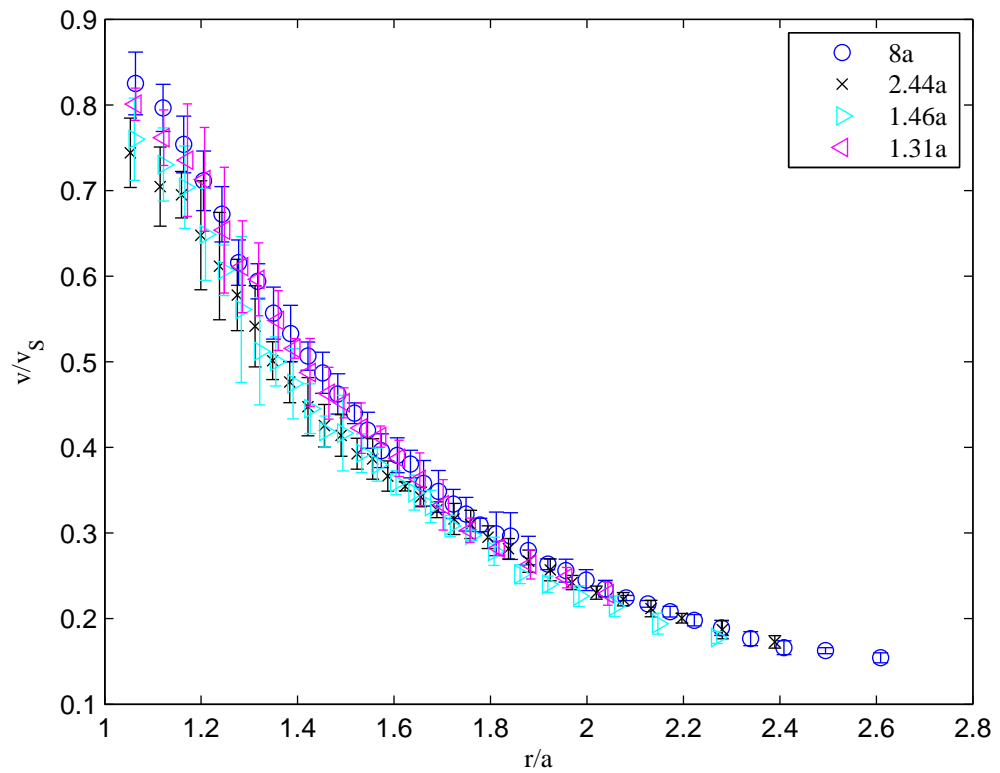
Figure 4.4: The normalised fluid velocity measured as a function of radial distance from the centre of a sphere for separation distances $h = 8a$, $2.44a$, $1.46a$, and $1.31a$ from a parallel, planar boundary. The fluid velocity has been normalised by the instantaneous velocity of the surface of the sphere.

trajectories of fluid elements in the primary flow were directed towards, and away from, the boundary so that there stagnation points developed in the flow.

An example of the instantaneous flow field produced by the interaction between a torsionally oscillating sphere and a perpendicular, planar boundary is shown in Figure 4.5. The arrowed lines in the image represent the instantaneous particle paths, and the colour contours the magnitude of the fluid velocity which ranges from $0 - 3.25$ mms^{-1}. This particular flow field corresponds to the clockwise rotation of the sphere at $3\pi/10$ in the oscillation cycle. The centre of the sphere was $1.36a$ from the solid, planar boundary which is depicted by the left-hand bounding line of the image. The primary flow is directed towards and away from the boundary which creates stagnation points in the flow adjacent to the boundary above and below the sphere. Good qualitative agreement is found between the instantaneous, experimental particle paths and numerical stream surfaces generated by a sphere undergoing steady rotation in proximity of a planar, perpendicular boundary [41], which are shown in Figure 4.6.

The distribution of fluid velocity across the gap between the sphere surface and the wall was measured along the surface normal joining the boundary and the centre of the sphere. Instantaneous PIV measurements were performed at $3\pi/10$ in the oscillation cycle of the sphere for sphere-wall separations of $3.00a$, $2.26a$, $1.90a$, $1.76a$ and $1.36a$ and then compared to the unbounded case where the container walls were $\sim 8a$ from the centre of the sphere. The measured fluid velocity effectively gives the velocity profile across the gap. The measured fluid velocity, v, was normalised by the in-
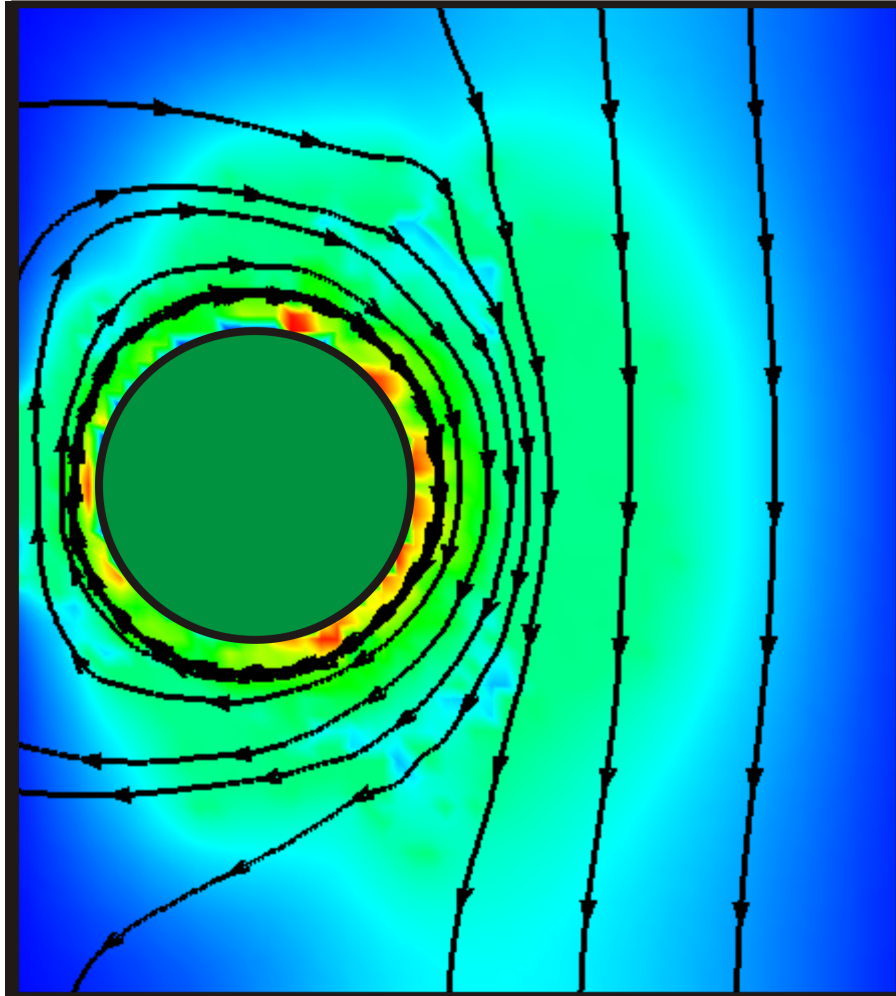
Figure 4.5: The instantaneous flow field, in the equatorial plane, generated by a sphere rotating clockwise, at $3\pi/10$ in the torsional oscillation cycle, in close proximity to a solid, planar boundary. The separation distance $h = 1.36a$ and the boundary is depicted by the left-hand bounding line of the image. The arrowed lines represent instantaneous particle paths and the colour contours represent the magnitude of the fluid velocity which ranges from 0 (dark blue) to 3.25 mms^{-1} (dark red).
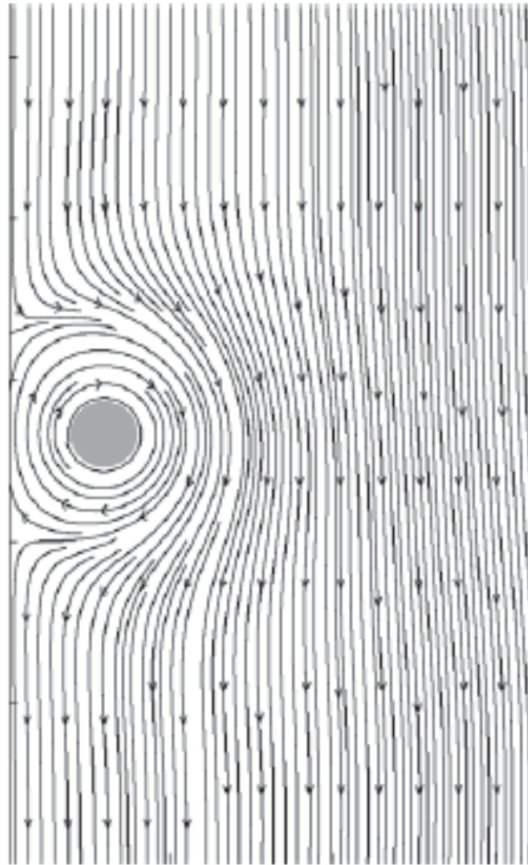
Figure 4.6: Numerically computed stream surfaces, in the equatorial plane, for a sphere rotating near a wall around an axis perpendicular to the surface normal and in the clockwise direction for $Re = 1$ [41]. The boundary is depicted by the solid line on the left-hand side of the image. The sphere-wall separation is $3a$.
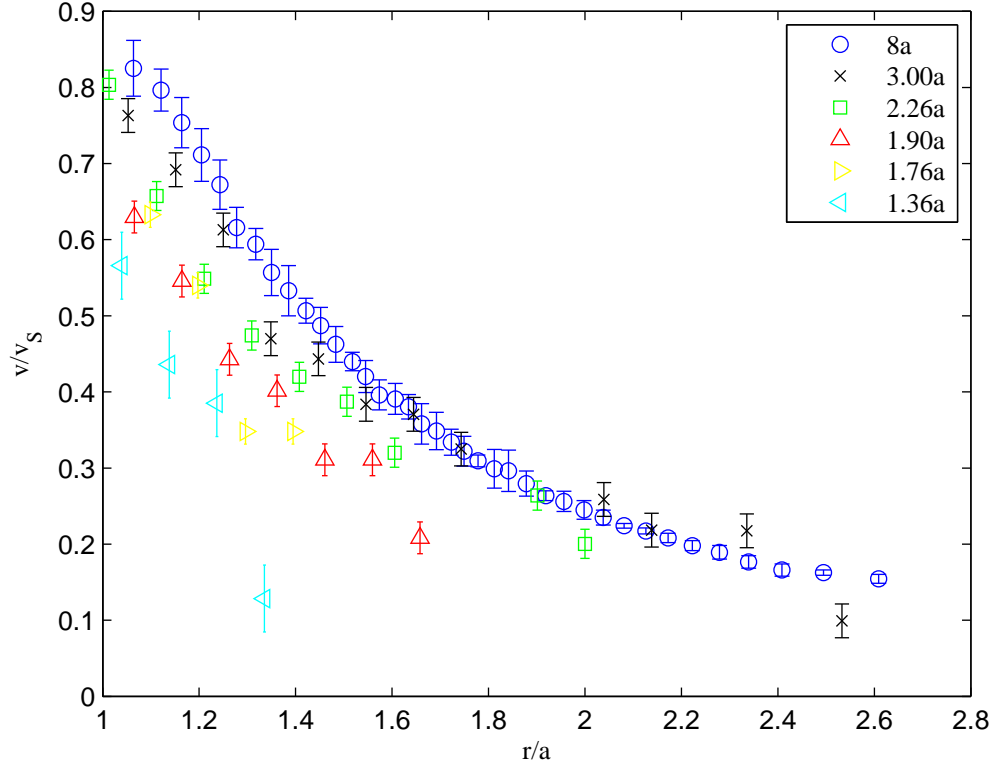
Figure 4.7: The normalised fluid velocity measured as a function of radial distance for separation distances $h = 8a$, $3.00a$, $2.26a$, $1.90a$, $1.76a$ and $1.36a$ from a planar, perpendicular boundary.

stantaneous velocity of the surface of the sphere, v_S and is shown in Figure 4.7 as a function of radial distance, r, from the centre of the sphere.

As in the case of the parallel boundary, the fluid velocity at all radial distances decreases with decreasing sphere-wall separation distance, h. The dimensionless data does not collapse when scaled, by the instantaneous tangential velocity of the surface onto a single curve. This demonstrates that the primary flow generated by the motion of the sphere is significantly altered by the presence of a perpendicular boundary. The no-slip condition applies on

103

the surface of the boundary which changes the functional dependence of the fluid velocity with radial distance. This change in the functional dependence of the fluid velocity reflects an increase in viscous shear and is particularly evident for the small separation $h = 1.36a$.

The amplitude of torsional oscillation, θ_A, was measured as a function of separation distance, h, to investigate how the resistance introduced by a perpendicular, planar boundary affects the driven sphere dynamics. The results for $\Gamma = 0.1175 \pm 0.0006$, $\hat{\epsilon} = 0.0997 \pm 0.0003$ and a drive frequency of $f = 0.5$ Hz are shown in Figure 4.8. The greater variance of the data points obtained when the sphere is in intermittent contact with the boundary was attributed to surface roughness disrupting the otherwise smooth, sinusoidal oscillation of the sphere. The dashed, red line denotes the thickness of the Stokes layer on the sphere $\delta \sim (\frac{\nu}{\omega})^{1/2} = 2.17a$, measured from the surface of the sphere at $r = a$.

When the sphere-to-wall separation is greater than the thickness of the Stokes layer, $h > \delta + a$, the effects of the perpendicular boundary on the driven sphere dynamics are negligible. Once the separation distance is sufficiently small, the boundary intersects the Stokes layer of the sphere, $h < \delta + a$, and the amplitude of torsional oscillation reduces as the sphere approaches the wall, as $h \to a$. The amplitude of the torsional oscillation of the sphere when close to the boundary is reduced by approximately a factor of 2 compared to when far from the boundary, i.e. for $h > \delta + a$. The suppression of torsional oscillation of the sphere at small separation distances is greater for a perpendicular boundary than for a parallel boundary.

The greater reduction in amplitude is a consequence of the flow field

generated by the rotation of the sphere being more significantly modified by the boundary in this case. The intersection of the boundary layer by the plane breaks the axisymmetry of the primary flow generated by the sphere motion and constrains the fluid velocity to zero on the surface of the plane. The resistance introduced by these viscous layer effects opposes the magnetic torque acting on the sphere suppressing the torsional oscillation of the sphere, θ_A.

In summary, a viscous torque has been observed to oppose the motion of the driven sphere and a viscous shear has been identified between the moving and stationary surfaces. A pressure will also be generated as the fluid is squeezed through the narrowing gap between the surfaces and will become significant for very narrow gaps. In numerical models of a sphere undergoing steady rotation near a perpendicular boundary, Liu and Prosperetti observed a pressure-driven force develop which was directed away from the boundary [41]. No motion of the sphere in a direction parallel to the surface normal of the boundary was resolved in the experiments. However, for $h/a \lesssim 1.5$, a manifestation of the more significant wall-parallel force was observed. For small separation distances, the viscous shear induced by the boundary generates a force which displaced the sphere in the z-direction, i.e. in the vertical direction parallel to the bounding surface, in accord with the numerical findings of Liu and Prosperetti for a sphere undergoing steady rotation [41]. In the experiments, the sphere performed unsteady rotation hence the induced displacement of the sphere was oscillatory.

The induced translational oscillation of the sphere is sinusoidal in form and in phase with the torsional oscillation of the sphere. The amplitude of the
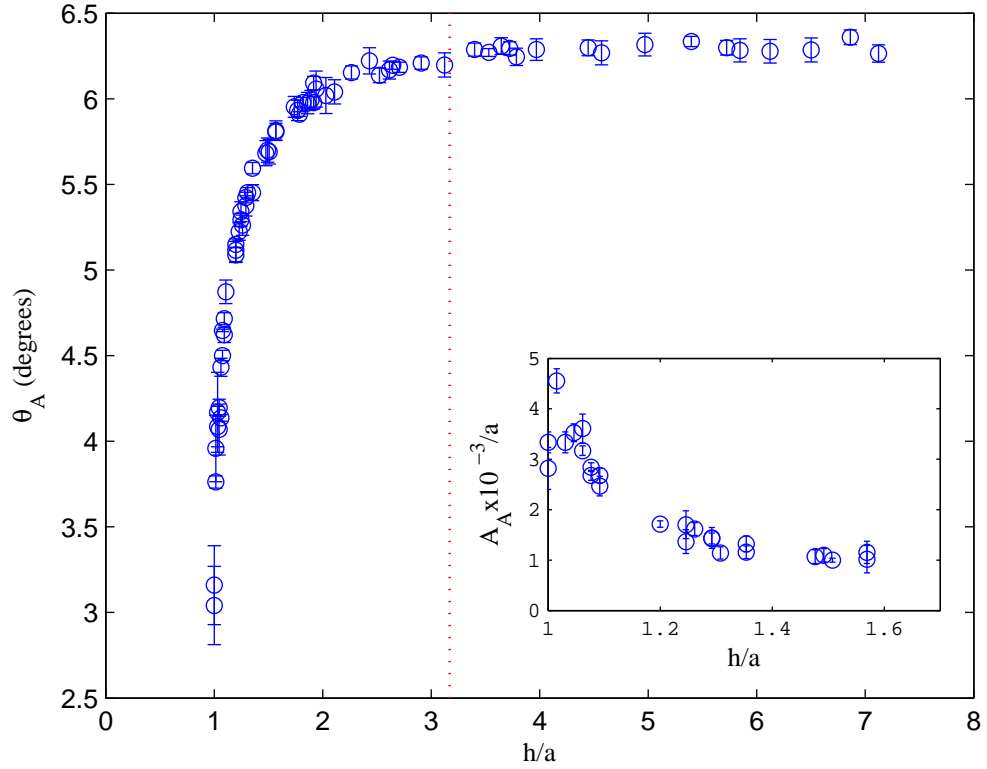
Figure 4.8: The amplitude of torsional oscillation of the sphere measured as a function of separation distance from a planar, perpendicular boundary for a frequency of applied magnetic field of 0.5 Hz. The dashed, red line denotes the Stokes layer thickness ($\delta \sim 2.17a$) measured from the surface of the sphere at $r = a$. Inset: The amplitude of translational oscillation of the centre-of-mass of the sphere measured as a function of separation distance from a planar, perpendicular boundary. The data was obtained for $\Gamma = 0.1175 \pm 0.0006$ and $\hat{\epsilon} = 0.0997 \pm 0.0003$. The error bars on the data points denote the standard deviation of the measurements.

translational oscillation of the sphere, A_A, is shown as a function of separation distance, h, in the inset to Figure 4.8. The amplitude increases as the sphere approaches the boundary, as $h \to a$, which suggests that the wall-parallel force increases as the viscous shear increases. As $h \to a$, the amplitude of translational oscillation reaches $\sim 40~\mu$m, which is approximately half the amplitude of the arc length subtended in a torsional oscillation of the sphere. However for $h \sim a$, the amplitude of oscillation reduces to $\sim 25~\mu$m because of frictional effects which arise when the rough surfaces of the sphere and boundary are in intermittent contact.

Confirmation that the suppression of torsional oscillation occurred when the planar boundary intersected the Stokes layer of the sphere, δ, was obtained by changing the frequency of applied magnetic field which changed the thickness of the Stokes layer. The amplitude of torsional oscillation of the sphere, θ_A, measured as a function of separation distance, h, from a planar, perpendicular boundary is shown in Figure 4.9 for drive frequencies of 1 Hz (top) and 0.25 Hz (bottom). For a drive frequency of 1 Hz, empirical data were obtained for $\Gamma = 0.1195 \pm 0.0017$ and $\hat{\epsilon} = 0.0499 \pm 0.0002$, and the Stokes layer thickness (denoted by the dashed, red line) was $\delta \sim 1.54a$. For a drive frequency of 0.25 Hz, empirical data were obtained for $\Gamma = 0.1187 \pm 0.0012$, $\hat{\epsilon} = 0.1982 \pm 0.0004$ and $\delta \sim 3.08a$.

The thickness of the Stokes layer varied between the two sets of experimental measurements by a factor of 2, as does the separation distance below which suppression of torsional oscillation occurs. The data sets therefore support the hypothesis that the intersection of the Stokes layer on the sphere by the planar boundary is responsible for the suppression of the torsional oscilla-

107
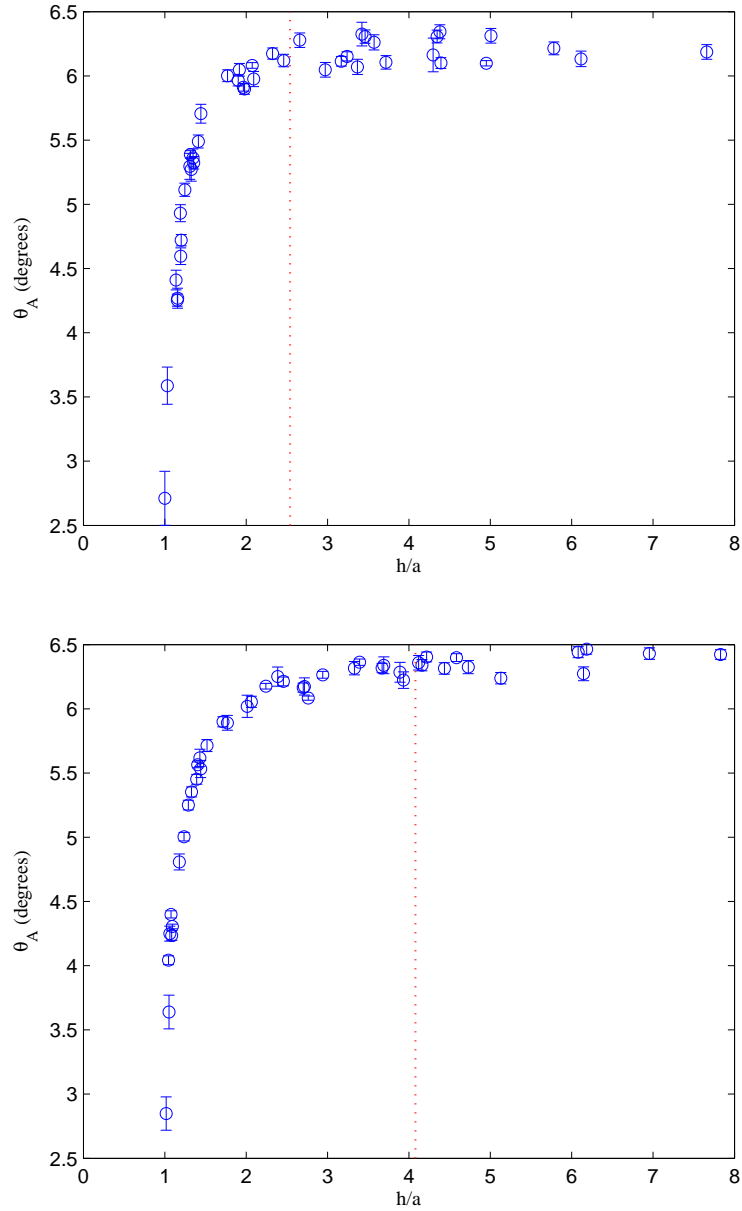
Figure 4.9: The amplitude of torsional oscillation of the sphere measured as a function of separation distance from a perpendicular planar boundary for applied magnetic fields of frequency 1 Hz (top) and 0.25 Hz (bottom). The dashed, red line denotes the Stokes layer thickness ($\delta \sim 1.54a$) (top) and ($\delta \sim 3.08a$) (bottom) measured from the sphere surface at $r = a$.

tion of the sphere. The no-slip condition on the planar boundary introduces a hydrodynamic resistance which opposes the magnetic torque acting on the sphere, thereby suppressing the torsional oscillation of the sphere. These viscous layer effects increase as the sphere approaches the boundary.

The slight difference in the amplitude of oscillation when far from the boundary for different drive frequencies, see Figure 4.8 and Figure 4.9, results from differences in the dimensionless gravitational torque term, $\hat{\epsilon}$, and the magnitude of the magnetic torque, Γ. Furthermore, the scatter in the data for $f = 1$ Hz, see Figure 4.9 (top), results from the greater deviation of dimensionless magnetic torque Γ compared to the data for drive frequencies of 0.5 and 0.25 Hz. The frequency of applied field was limited by the attenuation of the magnetic field strength which occurred above 4 Hz (see §2.4.2).

4.4   Summary

The viscous effects which arise from the presence of a planar boundary, and the no-slip condition which applies on the surface of a boundary, introduced a resistive torque which acted on the driven sphere and the surrounding fluid when the wall-sphere separation was less than the extension of the Stokes layer from the surface of the sphere, $h < \delta + a$. The resistive torque experienced by a sphere undergoing steady rotation near a boundary was previously observed in experiments conducted using optical tweezers [37]. In the experiments reported in this Chapter, the resistive torque induced by a presence of a boundary was dependent on the angular velocity of the sphere and was, therefore, time-modulated. The resistance introduced by a perpendicular boundary was more significant than the resistance introduced by a parallel

boundary. Furthermore, in both cases, the resistance was dependent on the sphere-wall separation distance and increased as the sphere approached the boundary.

The presence of a boundary with its surface normal perpendicular to the rotational axis of the sphere significantly altered the primary flow generated by a torsionally oscillating sphere, while a boundary with surface normal parallel to the rotational axis had minimal effect. The perpendicular boundary intersected the plane of the primary flow which broke the axial symmetry of the system and introduced stagnation points into the flow field. As $h \rightarrow a$, viscous shear effects increased and resulted in the generation of a force which displaced of the centre-of-mass of the sphere in the vertical direction.

The induced translational motion of the sphere was smaller than the arc length subtended by the surface of the rotating sphere. The translation of the sphere was oscillatory in nature and therefore did not result in net translational motion. In Chapter 5, the results obtained from studying the hydrodynamic interaction of a torsionally oscillating sphere and a planar boundary are used to provide insight into the interaction between pairs of spheres.

Chapter 5

Two Spheres

In this Chapter, the hydrodynamic interaction between a sphere performing torsional oscillations and a second, stationary sphere is discussed. The specific methods used and other experimental details will be described in §5.1. The predominant dynamic behaviour which resulted from the interaction of an active sphere performing small-amplitude torsional oscillations in a viscous fluid and a non-magnetic, passive sphere of equal radius is discussed in §5.2. This includes a description of the effects which only occur for small separation distances, in §5.2.2. In §5.3, the results outlined in §5.2 are generalised for particle-pairs of unequal radii and for driven spheres performing large-amplitude torsional oscillations. Finally, in §5.4, the possibility of inertial effects in the system was investigated by significantly reducing the Re of the system.

5.1 Experimental Details

The experiments concerned the dynamic interaction of an active sphere with a nearby passive sphere. An active sphere is a neutrally buoyant sphere with a magnetic dipole axis that is aligned approximately horizontally with zero applied magnetic field. When subjected to an alternating field, applied in the vertical direction, the sphere performed torsional oscillations about its centre generating a flow in the viscous fluid. A neutrally buoyant passive sphere was placed at various distances from the oscillating sphere and was observed to be driven by the flow.

The centre of the passive sphere was positioned in the plane of the primary flow of the active sphere, i.e. in the equatorial plane of the driven, active sphere. The centres of the spheres were aligned using a laser sheet which was positioned above the fluid filled tank. Observations were made along a line parallel to the rotational axis of the active sphere as shown in Figure 5.1. Figure 5.1 also includes indications of the modes of oscillatory motion of the two interacting spheres. The separation between the spheres, h, was measured from the centres of each sphere so that, when the spheres were very close to contact, the separation distance was the sum of the radii of the spheres, i.e. for spheres of equal radii the minimum separation distance $h_{min} = a_A + a_P$, where a_A is the radius of the active sphere and a_P is the radius of the passive sphere. Previous measurements of polypropylene spheres indicated that the surface roughness of the spheres was of the order of tens of μm [95]. Markings were present on the surface of all of the spheres which enabled the tracking of the translational and rotational motion of the active and passive spheres in image sequences.

112
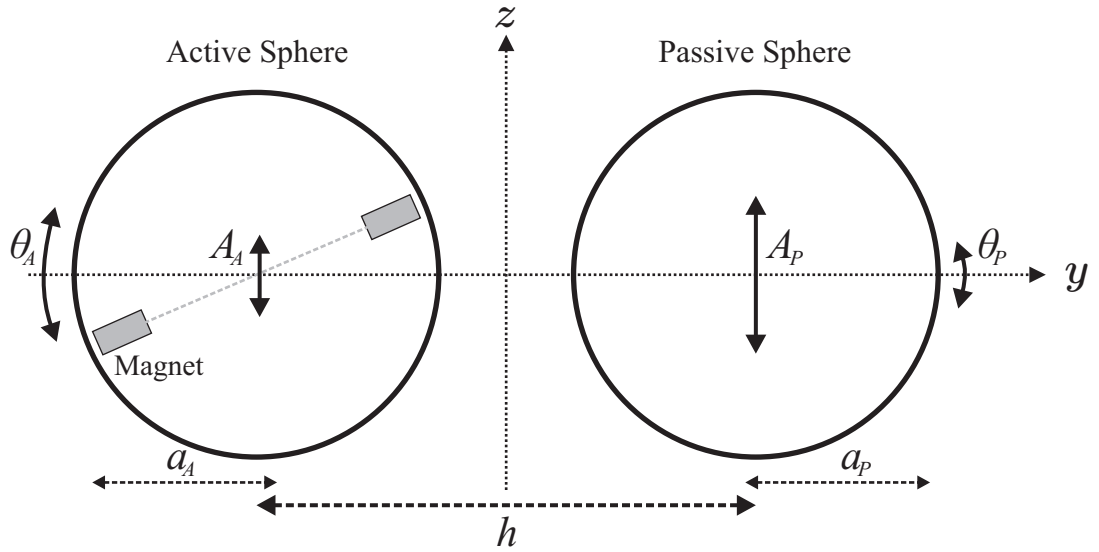
Figure 5.1: Schematic diagram of the two-sphere system, as viewed by the observer, indicating the position and direction of rotation of the active sphere and the position of the passive sphere in the $y - z$ plane. The magnetic-dipole axis of the active sphere is depicted in the diagram, as is the radii of the active and passive spheres, a_A and a_P respectively, and the separation distance between the centres of the spheres, h. The solid, arrowed lines indicate the modes of rotational, θ_A and θ_P, and translational, A_A and A_P, motion of the active and passive spheres, respectively.

In the following section, §5.2, the hydrodynamic interaction between an active sphere performing small-amplitude torsional oscillations and a passive sphere of equal diameter, 15.86 ± 0.01 mm, will be presented. The results will then be extended, in §5.3, to the interactions between:

- An active sphere of diameter 15.86 ± 0.01 mm and passive spheres of diameter 12.70 ± 0.01 mm, 9.53 ± 0.01 mm, and 6.34 ± 0.01 mm.

- An active sphere of diameter 12.70 ± 0.01 mm and passive spheres of diameter 12.70 ± 0.01 mm and 15.86 ± 0.01 mm.

- An active sphere of 15.86 ± 0.01 mm performing large-amplitude torsional oscillations and passive spheres of 15.86 ± 0.01 mm and 12.70 ± 0.01 mm.

The physical properties of the spheres are outlined in Table B.1 for each of the two-sphere combinations, see Appendix B. Table B.1 includes the following information: the radii of the active sphere (a_A) and the passive sphere (a_P), the average density of the spheres, the fluid viscosity, the magnetic and gravitational torque parameters to which the active sphere was subjected, the time-scale associated with the gravitational torque acting on the active sphere, the approximate amplitude of torsional oscillations of the active sphere when solitary in the fluid and subjected to the applied field, and the angle at which the magnetic-dipole axis of the active sphere resides when subjected to zero applied field. The frequency of the applied field was chosen to be 0.5 Hz and observations were made at 50 frames per second so that the motion of the spheres was sampled at 100 times the drive frequency.

5.2 Spheres of Equal Radii

This section describes the dynamic behaviour which results from the hydrodynamic interaction between an active sphere performing small-amplitude torsional oscillations and a passive sphere of equal radius, $a_A = a_P = a = 7.93$ mm. The minimum separation distance between the spheres was $h_{min} = 2a$. The primary effects which were observed for all separation distances are detailed in §5.2.1. Secondary effects, which occurred for small separation distances, are described in §5.2.2. The secondary effects will be discussed with reference to the influence of a perpendicular boundary on the dynamic behaviour of a torsionally oscillating sphere in a viscous fluid, as outlined in §4.3.

5.2.1 Primary Effects

The dominant effect which resulted from the hydrodynamic interaction of an active sphere and a passive sphere, both of diameter 15.86 ± 0.01 mm, was that the rotary motion of the active sphere generated a flow which displaced the passive sphere. The displacement of the passive sphere was in a straight line orthogonal to a line joining the centres of the sphere, i.e. in the vertical direction if in the configuration the particles were separated horizontally. By way of contrast, a tracer particle in the fluid executed a oscillatory trajectory along an arc defined by a circular path which is concentric to the rotational axis of the sphere, see §3.5. Passive spheres subjected to the flow generated by larger diameter active spheres were also observed to follow arc-like trajectories, see §5.3. The change in trajectory between tracer particles and larger passive spheres is discussed further in §5.3.
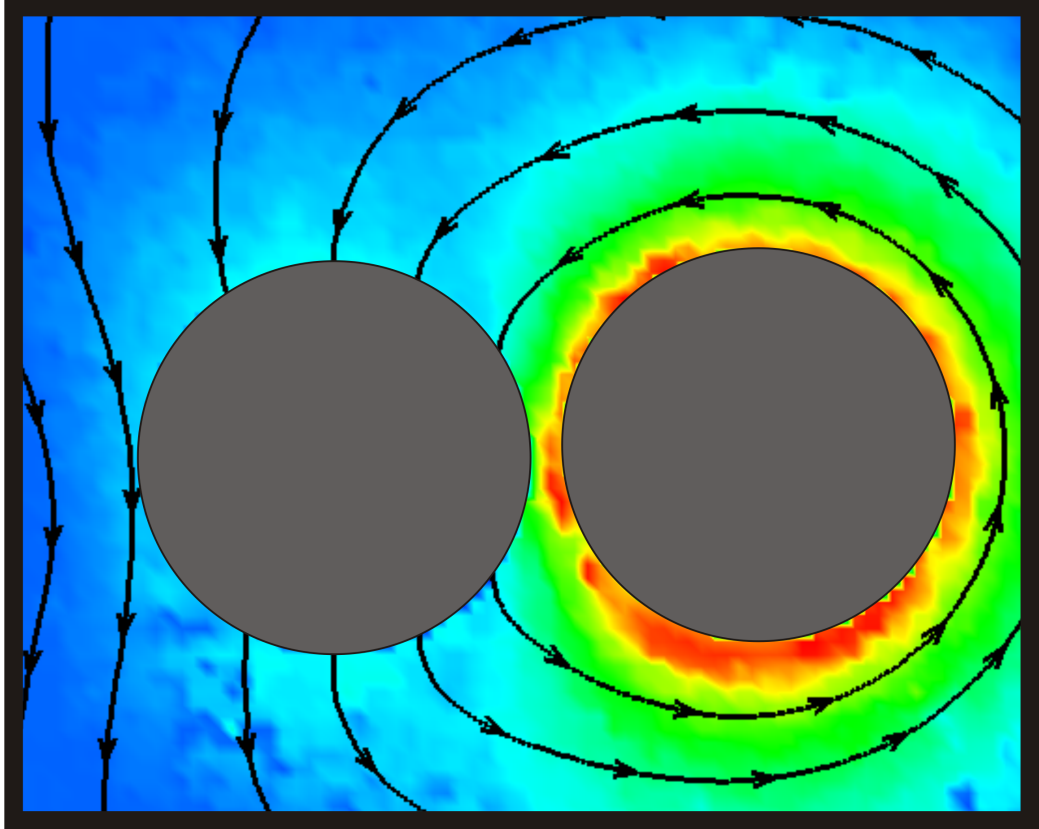
Figure 5.2: The instantaneous flow field resulting from the interaction be-
tween a rotating sphere (on the right-hand side) and a passive sphere at
$\sim 10\pi/6$ in the torsional oscillation cycle. The particle paths are depicted by
the black, arrowed lines and the magnitude of the fluid velocity by the colour
contours (where blue = 0 mms^{-1} and red = 9.98 mms^{-1}). The separation
distance, h, between the two spheres is $2.25a$, where a is the radii of the
spheres.

Instantaneous flow visualisation of the interaction between the driven and passive spheres of equal radii was conducted using the PIV technique outlined in §2.6.1. A flow field obtained at $\sim 10\pi/6$ in the oscillation cycle is shown in Figure 5.2. The grey circles correspond to the spheres, with the active sphere on the right-hand side of the image and the separation distance between the spheres is $h = 2.25a$. The magnitude of the fluid velocity is represented by the colour contours (where dark blue $= 0$ mms^{-1} and dark red $= 9.98$ mms^{-1}) and the arrowed lines in the image depict particle paths. Particle paths, the trajectories which particles in the fluid would follow, were shown to be concentric circles around a single unbounded rotating sphere in §3.5 but here are found to be affected by the presence of the nearby passive sphere. The deformation of the particle paths as they pass close by the passive sphere shows that the fluid displaced the passive sphere in the vertical direction.

Lateral motion of the passive sphere, along a line joining the centres of the spheres, was not resolved in the experiments. Even for small separations, for which the pressure generated between the spheres may have been thought to be significant, the passive sphere was only observed to translate in the vertical direction. The functional dependence of the amplitude of the translational oscillation of the passive sphere on separation distance is shown in Figure 5.3. The amplitude, A_P, decreases with increasing separation distance, h, more rapidly than a inverse square relationship. A least-squares fit to the experimental data (blue markers) has the form $A_P = 0.1488h^{-2.5340} + 0.0007$ and is depicted by the red line. Deviation of the experimental data from the fitted curve occurs for small separations, $h \approx h_{min}$, and may be understood by considering the induced motion of the active sphere which occurs for

$h \rightarrow h_{min}$ and is discussed further in §5.2.2.

The decay of the amplitude of the motion of the passive sphere with increasing separation distance allows an estimate of the penetration depth to be made. The penetration depth was calculated from the fit to be $1.02a$. In other words, at a sphere-sphere separation distance of $h = 3.02$, the amplitude of motion of the passive sphere was ~ 0.37 of its value at $h_{min} = 2a$. A sphere-sphere separation of $3.02a$ is approximately equal to the calculated extent of the Stokes layer from the surface of the active sphere into the fluid, $\delta + a = 3.16a$. Furthermore, this separation distance between spheres was comparable to the sphere-wall separation distance below which the torsional oscillations of an active sphere were suppressed by boundary effects, see §4.3, for an applied field of 0.5 Hz.

The small phase difference, σ, between the torsional oscillations of the active sphere and the translational oscillations of the passive sphere increases linearly with increasing separation distance, h, and is shown in the inset to Figure 5.3. A linear least-squares fit to the experimental data (blue markers) has the form $\sigma = 0.2182(h/a) - 0.2942$ and is depicted by the red line. A passive sphere which is further away from the active sphere is displaced by the generated flow at a later time. This phase lag between the motion of the active sphere and the response of the passive sphere was believed to arise from the unsteady motion of the active sphere generating a wave in the fluid and is discussed further in §5.4.

The flow generated by the rotational motion of the active sphere forced the passive sphere to perform small-amplitude rotational oscillations. The passive spheres rotated with an amplitude that approached 5% of the am-

Figure 5.3: The amplitude of the translational oscillation of the passive sphere measured as a function of separation distance from an active sphere performing torsional oscillations of amplitude $\theta_A \sim 6°$. The blue markers denote the experimental data, the standard deviation of which is represented by the error bars, and the red line corresponds to the least-squares fit to the data which has the form $A_P = 0.1488h^{-2.5340} + 0.0007$. Inset: The phase difference between the torsional oscillations of the active sphere and the translational oscillations of the passive sphere measured as a function of separation distance. The red line represents a least-squares fit to the experimental data (blue markers) which has the form $\sigma = 0.2182(h/a) - 0.2942$. Error bars are not included for visual clarity.

119

Figure 5.4: The amplitude of the torsional oscillation of the passive sphere measured as a function of separation distance from an active sphere performing torsional oscillations of amplitude $\theta_A \sim 6°$. Inset: The amplitude of the torsional oscillation of the passive sphere measured as a function of separation distance from an active sphere performing torsional oscillations of amplitude $\theta_A \sim 54°$. The blue markers denote the experimental data, the standard deviation of which is represented by the error bars.

plitude of rotation of the active sphere as the spheres were positioned very close to one another. The direction of rotation of the passive sphere was counter-clockwise to the torsional motion of the active sphere and the oscillations were approximately in antiphase. The torsional motion of the passive sphere was induced by a shear which resulted from the no-slip condition on the surface of the sphere and the velocity gradient acting across the finite size body. The velocity gradient is a consequence of the generated fluid velocity decreasing with radial distance from the surface of the active sphere. The amplitude of the torsional oscillations of the passive sphere, θ_P, decreased with increasing separation distance, h, because of the non-linear decay of the fluid velocity with distance from the active sphere, see Figure 5.4. The deviation of results for $h \to h_{min}$ is attributed to the induced motion of the active sphere which occurs at small separation distances, as is discussed further in §5.2.2.

For $h > 3.5a$, the small rotary response of the passive sphere to torsional oscillations of the active sphere could not be resolved in the experiments. However, this phenomenon did not only occur at small separations distances. For large-amplitude torsional oscillations of the active sphere, the rotary response of the passive sphere was observed for separation distances greater than $3.5a$. The amplitude of torsional oscillations of the passive sphere, θ_P, was measured as a function of separation distance, h, for large-amplitude torsional oscillations of the active sphere ($\theta_A \sim 54°$), see the inset to Figure 5.4. The relative magnitude of θ_P, and the decrease in θ_P with increasing separation distance, is consistent with the results obtained for small-amplitude oscillations of the active sphere. The results obtained for large-amplitude

torsional oscillations of the active sphere are discussed further in §5.3. In the following section, the phenomena which occur for small separation distances $h < \delta + a$, where δ is the thickness of the Stokes layer on the surface of the active sphere, are discussed.

5.2.2 Secondary Effects

For large separation distances, the amplitude of the torsional oscillation of the active sphere, θ_A, was independent of the separation distance from the passive sphere. In other words, for $h > \delta + a$, the presence of the passive sphere does not affect the dynamic response of the active sphere to the applied field. However, for $h < \delta + a$, viscous effects introduce a resistance to motion which reduces the amplitude of torsional oscillation of the active sphere. This effect is similar to that of a perpendicular boundary in close proximity to an active sphere, which was described in §4.3. The surface of the passive sphere intersected the plane of the primary flow generated by the torsionally oscillating sphere, breaking the axisymmetry of the flow field, and constrained the fluid velocity to the local velocity on the surface of the passive sphere. For $h < \delta + a$, the amplitude of the torsional oscillation of the active sphere, θ_A, decreases as the minimum separation distance is approached, as $h \rightarrow 2a$, see Figure 5.5. However, the suppression of the torsional oscillation of the driven sphere is not as significant as the suppression which results from the interaction of a active sphere and a planar, perpendicular boundary because of the curvature and finite size of the passive sphere.

Furthermore, for small separation distances, the viscous shear which develops between the two spheres generates a force which displaces the active
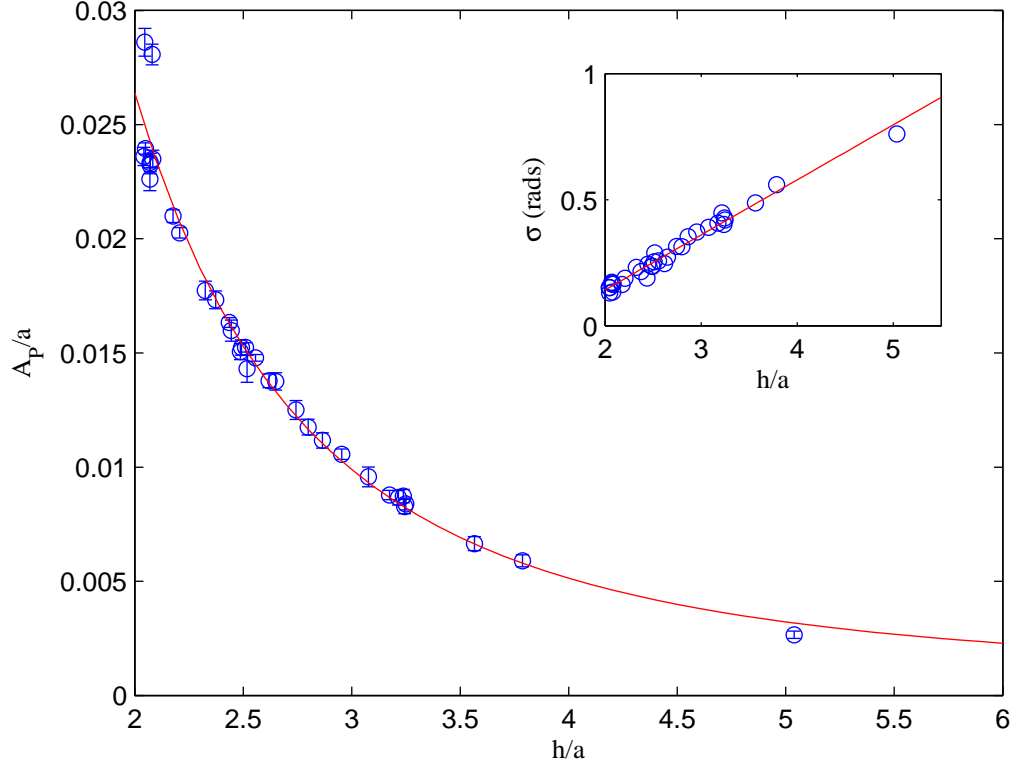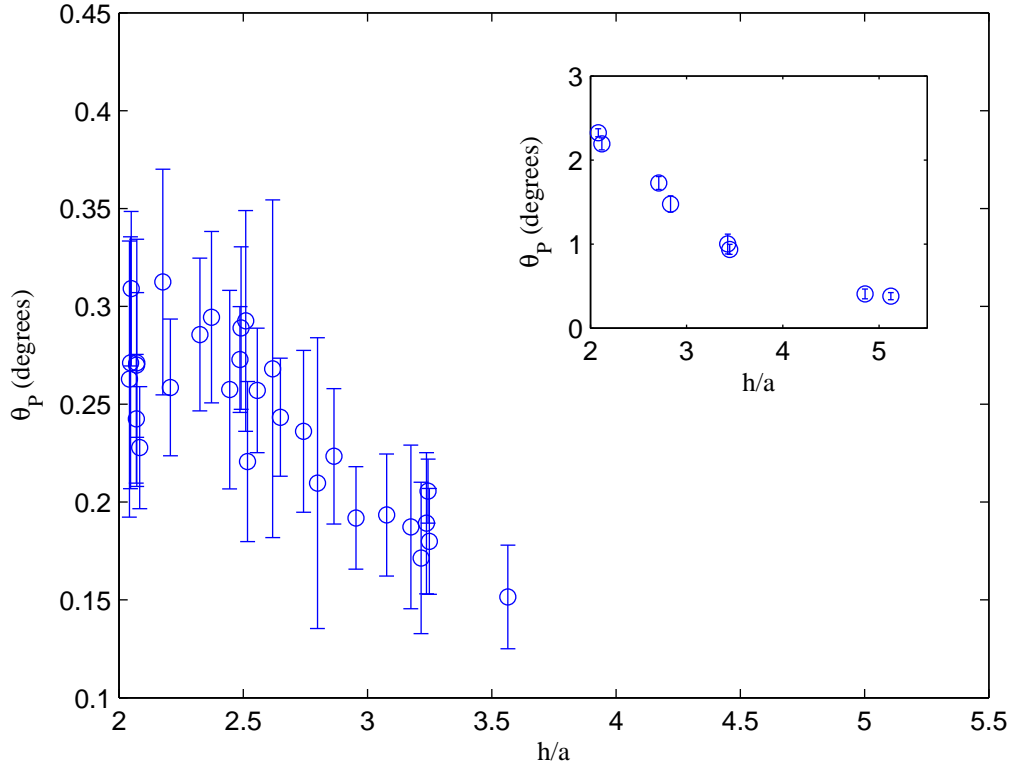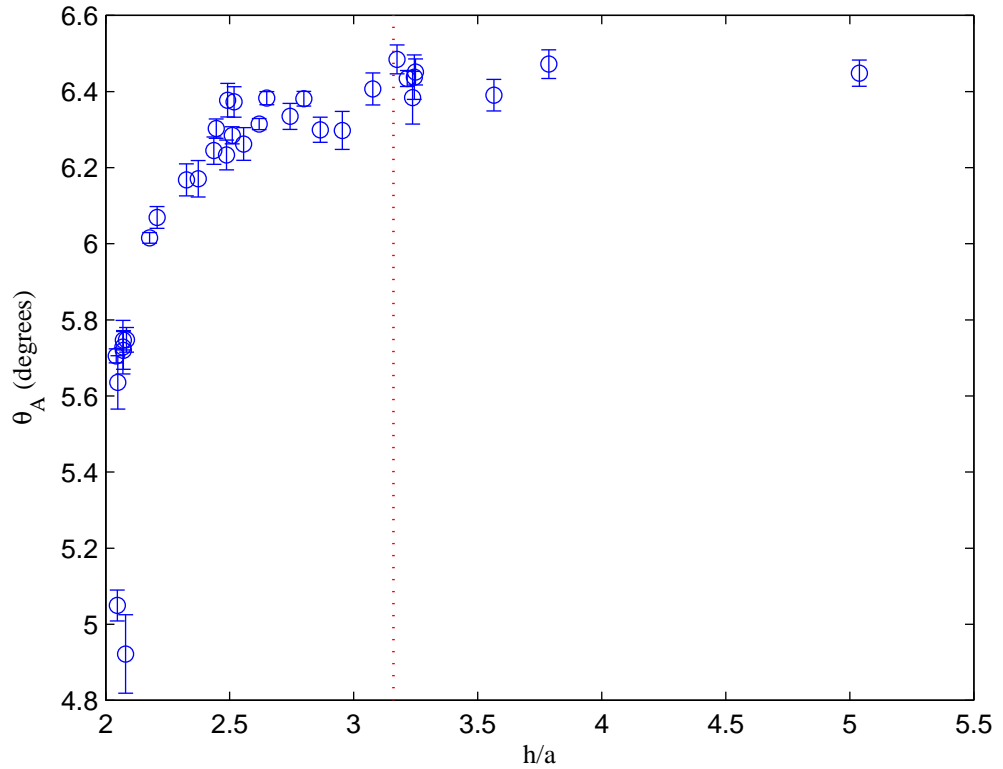
Figure 5.5: The amplitude of torsional oscillation of the active sphere measured as a function of separation distance from the passive sphere. The error bars on the data markers denote the standard deviation of the measurements. The dashed, red line denotes the thickness of the Stokes layer ($\delta \sim 2.16$) measured from the surface of the active sphere at $r = a$.

sphere in a direction perpendicular to a line joining the centres of the spheres, i.e. in the vertical direction. This induced motion of the active sphere is observed for $h < 3a$, in accord with the wall-parallel force which develops between a steady rotating sphere and a perpendicular boundary [41]. The displacement of the active sphere is in a direction opposite to that in which the passive sphere is displaced, orthogonal to the line joining the centres of the spheres. The amplitude of translational oscillation of the active sphere, A_A, increases with decreasing separation distance, see Figure 5.6. The substantial increase in the translational motion which occurs as $h \to h_{min} = 2a$ is attributed to the hydrodynamic slip which results when the separation distance is small enough that a lubrication layer forms between the two spheres. As $h \to 2a$, the active sphere moves approximately a quarter of the distance that the passive sphere moves because of the actively generated flow. This phenomena is analogous to the translational displacement of an active sphere which occurs for small separation distances from a planar, perpendicular boundary. In fact, the displacement of an active sphere in close proximity to a passive sphere is greater than the displacement of an active sphere when in close proximity to a perpendicular boundary. This suggests that a feedback mechanism exists between the two dynamic spheres which is not present in the interaction of a sphere and a stationary boundary.

The normalised amplitudes of translational oscillation of both the passive sphere, A_P, and the active sphere, A_A, are shown in the inset to Figure 5.6 for comparison. The amplitude of the translational oscillation has been non-dimensionalised by the amplitude of arc length subtended by an active sphere subject to the corresponding drive parameters in an unbounded fluid.

124

Figure 5.6: The amplitude of the induced translation oscillation of the active sphere measured as a function of separation distance from the passive sphere. The standard deviation of the data is represented by the error bars on the markers and the dashed, red line denotes the extent of the Stokes layer from the surface of the active sphere. Inset: The non-dimensionalised amplitude of translation oscillation of the passive sphere ($\square$) and the active sphere (o) measured as a function of separation distance. The amplitude of translational oscillation has been non-dimensionalised by the amplitude of arc length subtended by an active sphere subject to the corresponding drive parameters in an unbounded fluid. The amplitude of torsional oscillation of such a sphere was numerically calculated to be $\theta_A^* = 6.74°$ which corresponds to an amplitude of arc length of $s = a\theta_A^* = 0.93$ mm.

The amplitude of torsional oscillation of such a sphere was calculated numerically, using the model described in §3.3, to be $\theta_A^* = 6.74°$ which corresponds to an amplitude of arc length of $s = a\theta_A^* = 0.93$ mm. Although this non-dimensionalisation provides a measure of the translational oscillation of the spheres relative to the arc length subtended by an active sphere, it does not account for the suppression of torsional oscillation which occurs at small separation distances. Therefore, to include the suppression of torsional oscillation, further measurements, presented in §5.3, of the amplitude of the translational motion of the passive sphere, A_P, will be non-dimensionalised by the corresponding, empirical measurement of the amplitude of arc length subtended by the active sphere $s = a_A\theta_A$. Non-dimensionalisation of the amplitude of translational motion in this manner enables the primary interaction effects observed for spheres of equal radii to be generalised to spheres of unequal radii and thus unequal curvature.

5.3   Spheres of Unequal Radii

In this section, the results are reported for an investigation of spheres of unequal radii and for active spheres performing large-amplitude torsional oscillations. A list of the size combinations used is outlined in Table 5.1.

The observed dynamics were qualitatively the same for all of the investigated combinations of particle-pairs. The following behaviour was observed regardless of whether the active sphere was larger than the passive sphere, $a_A > a_P$, or *vice versa*, and whether the active sphere performed small-amplitude torsional oscillations of $\theta_A \sim 6°$ or torsional oscillations of amplitude $\theta_A \sim 50°$. The predominant effect was the displacement of the passive

a_A (mm)	a_P (mm)	θ_A (degrees)	marker
7.93	7.93	~ 6	o
7.93	4.77	~ 6	x
7.93	3.17	~ 6	□
6.35	6.35	~ 5	△
7.93	4.77	~ 30	◁
7.93	7.93	~ 54	▷
6.35	7.93	~ 6	▽

Table 5.1: Details of the particle-pair combinations studied in §5.3, including; the radii of the active and passive spheres, a_A and a_P, respectively; the approximate amplitude of torsional oscillation of the active sphere, θ_A, when far from the passive sphere; and the corresponding data marker used in Figures 5.7 and 5.8. The dimensionless parameters associated with the applied magnetic field, which result in differences in θ_A, are documented in Appendix B.

sphere by the flow generated by the rotary motion of the active sphere. The amplitude of translational motion of the passive sphere decreased exponentially with increasing separation distance between the two spheres. The phase difference between the torsional oscillations of the active sphere and the translational motion of the passive sphere increased linearly with increasing separation distance. As well as translating, the passive sphere was observed to rotate, a consequence of the velocity gradient acting across its finite-sized body.

For small separation distances, the torsional oscillations of the active

sphere were suppressed because the no-slip condition on the surface of the passive sphere introduced viscous effects that opposed the magnetic torque acting on the active sphere. For separation distances approaching $h \approx a_A + a_P$, the active sphere performed translational oscillations in antiphase to the motion of the passive sphere. The translational motion of the active sphere changed the flow field from that produced by a purely rotating sphere.

The following distinction in dynamics was apparent for passive spheres of various sizes. The radius of curvature of the arc-like trajectory that the passive spheres followed when displaced by the flow increased with increases in the radius of the sphere. In §3.5, tracer particles of 13.9 μm mean diameter were shown to follow a circular arc around the active sphere. However, passive spheres of diameter 15.86 mm were found to follow a straight line when in the presence of an active sphere of equal diameter performing small-amplitude torsional oscillations. This change in trajectory was attributed to the deformation of particle paths as they come into contact with the surface of the passive sphere. As the radius of the passive sphere increases this deformation effect increases and results in the increased radius of curvature of the translational trajectory of the passive sphere. In summary, the trajectory of a displaced passive sphere was dependent on how much the flow field generated by the active sphere was deformed by the presence of the passive sphere itself. The arc-like trajectories of passive spheres were not attributed to a repulsive force which could have resulted from a build up of pressure between the two spheres.

For all combinations of active and passive spheres, the amplitude of the translational oscillation of the passive sphere decreased with increasing
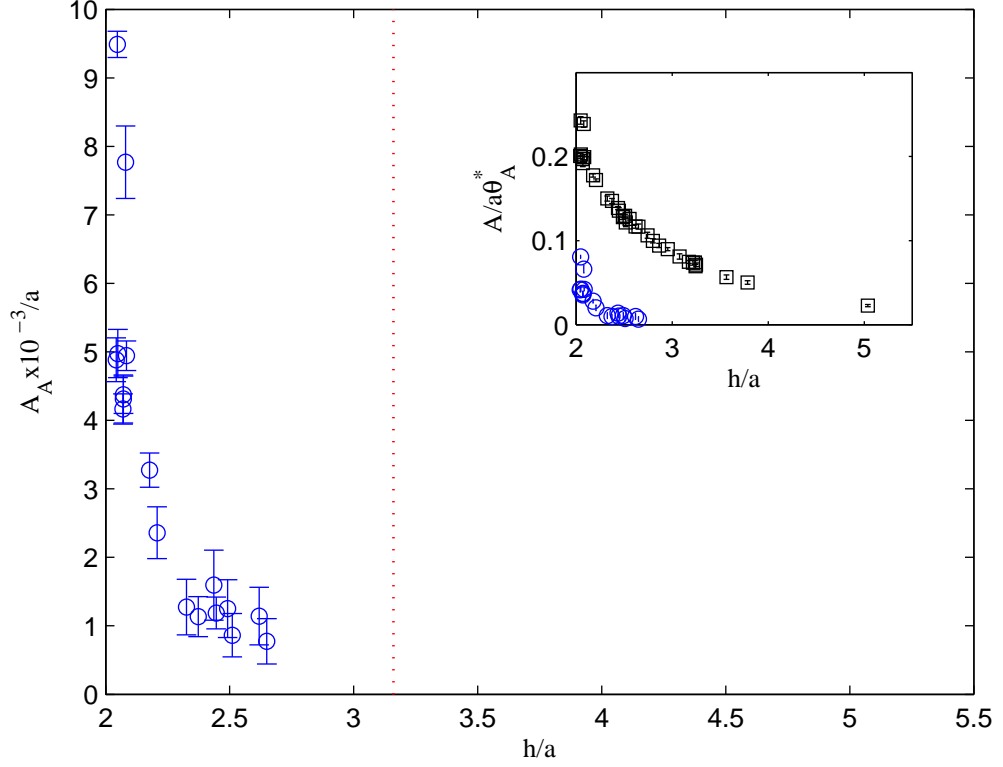
Figure 5.7: The amplitude of translational oscillation of the passive sphere measured as a function of the separation distance for various combinations of spheres. The amplitude of translational oscillation has been non-dimensionalised by the arc length subtended by the active sphere in a torsional oscillation, and the separation distance between the centres of the spheres has been non-dimensionalised by the radius of the active sphere. For each combination, the radii of the spheres, the approximate amplitude of torsional oscillation of the active sphere and the corresponding data marker are detailed in Table 5.1.

sphere-sphere separation distance. The amplitude of the translational oscillation of the passive sphere, A_P, was non-dimensionalised by the amplitude of the arc length subtended by the active sphere in a torsional oscillation, $s = a_A \theta_A$. This gave collapse of the experimental data onto a single curve, as shown in Figure 5.7, when plotted as a function of the separation distance, h, non-dimensionalised by the radius of the active sphere, a_A. For each of the combinations of spheres, the radii of the spheres, the approximate amplitude of torsional oscillation of the active sphere and the corresponding data marker are detailed in Table 5.1. Non-dimensionalisation of A_P by s incorporates the suppression of θ_A which occurs for small separation distances. Collapse of the data onto a single curve indicates that the generated flow is qualitatively the same for all particle-pair interactions.

A least-squares fit to the experimental data has the form:

$$\frac{A_P}{a_A \theta_A} = 1.1917 \left(\frac{h}{a_A}\right)^{-2.2548} - 0.0060 \tag{5.1}$$

and is depicted by the black line in Figure 5.7. As the separation increases the motion of the passive particle decays more rapidly than the flow generated by a solitary active sphere which follows an inverse square relationship with distance, see §3.5. The fit suggests that a passive particle of negligible size in contact with the surface of the active sphere would be translated a distance $\sim$ 18% greater than the arc length subtended by the active sphere (if frictional and lubrication effects are ignored). Deviations from the exponential curve occur for separation distances $h \approx a_A + a_P$ for which translational oscillations of the active sphere are observed. The combined translational and rotational motion of the active sphere results in a significantly different flow field to that of an active sphere performing rotary motion alone. The change in flow field

and the interaction between the two translating spheres leads to a complex dynamic behaviour which is not captured by the scaling used in Figure 5.7.

The phase difference, σ, between the torsional oscillations of the active sphere and the translational oscillations of the passive sphere increases linearly with increasing separation distance, h, as shown in Figure 5.8. A linear fit to the data has the form $\sigma = 0.2075(h/a_A) - 0.2577$. The fit to the data suggests that, within experimental error, there would be zero phase lag between the torsional oscillations of a sphere and the translational oscillations of a particle of negligible size adjacent to the surface of the rotating sphere. An explanation of the phase difference was provided by a theoretical model of the system that is described in Appendix C. The model is based on a oscillating rotlet singularity and shows that the phase difference is a consequence of the unsteady motion of the active sphere which generates a wave in the fluid. As in the case of a wall oscillating in a semi-infinite fluid [94], the generated wave decays exponentially in space and has an associated phase. However, the small non-zero phase difference may also be an inertial effect as the experiments were conducted in the range $0.01 \lesssim Re \lesssim 0.1$ and hence were only an approximation to the idealisation of Stokes flow. An investigation into the possible influence of inertial effects is presented in the following section.

5.4   Reduced Reynolds Number

In order to investigate the influence of inertia in the experiments, the Re of the system was reduced. The reduction in Re was achieved by increasing the viscosity of the fluid in which the spheres were submerged.

131

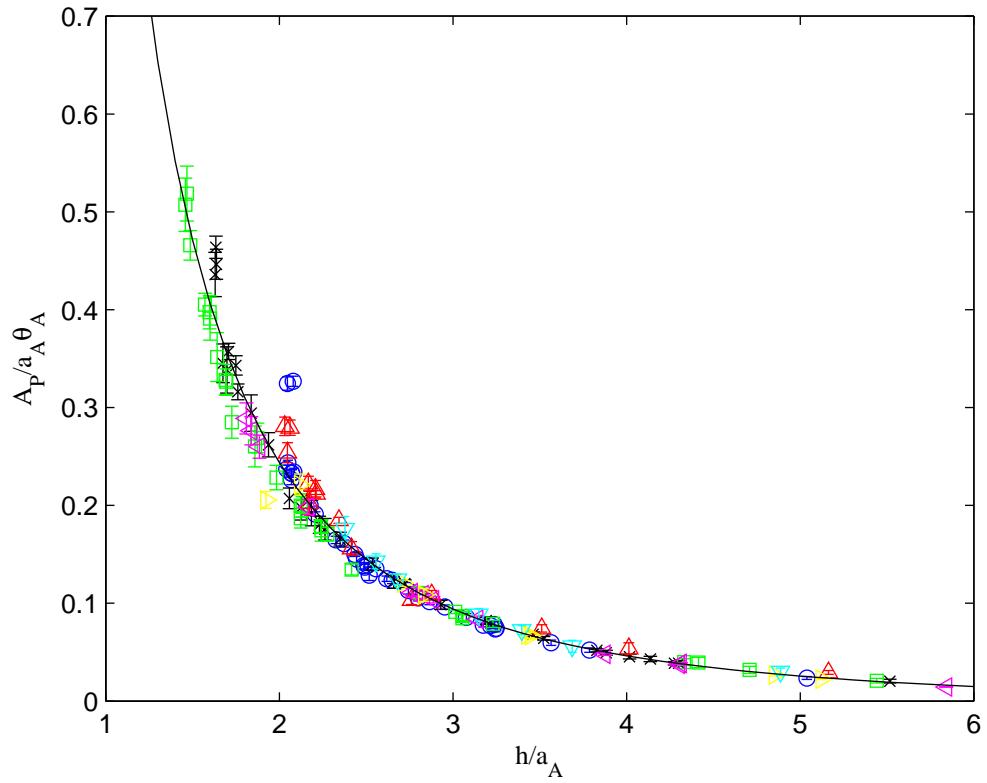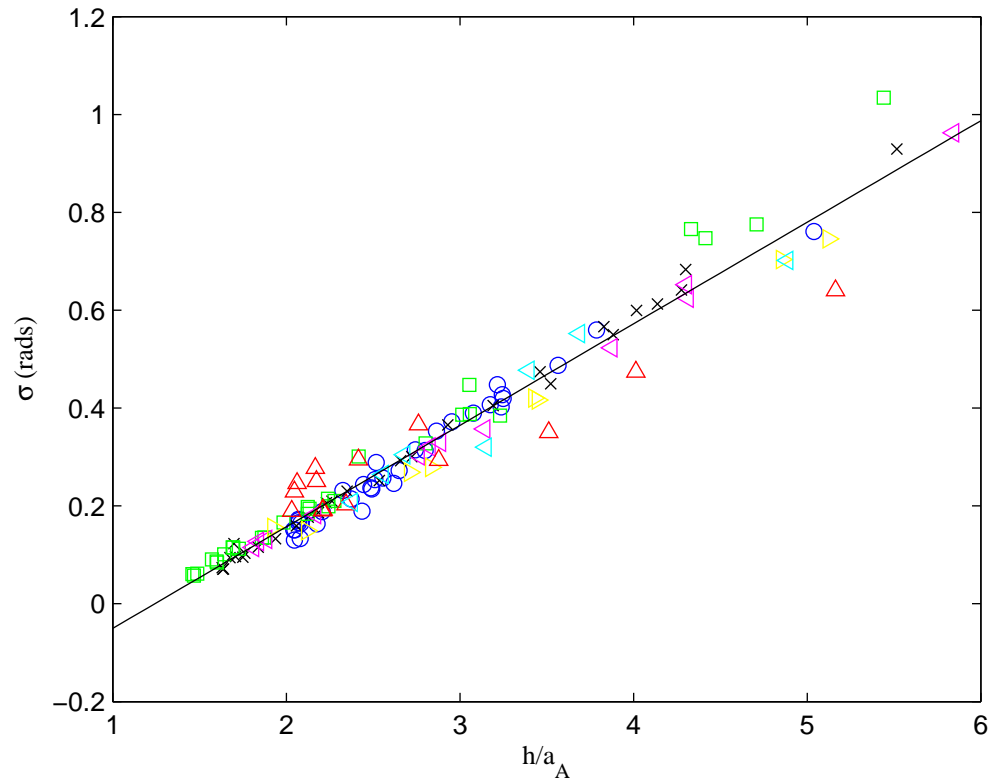Figure 5.8: The phase difference between the torsional oscillations of the active sphere and the translational oscillations of the passive sphere measured as a function of the separation distance for various combinations of spheres. For each combination; the radii of the spheres, the approximate amplitude of torsional oscillation of the active sphere and the corresponding data marker are detailed in Table 5.1. Error bars are not included for visual clarity.

The experiments were performed with the equal diameter active and passive spheres which were of diameter 15.86 ± 0.01 mm, as used in §5.2. The fluid was silicone oil (Basildon Chemical Company Limited, Oxfordshire, UK). The temperature inside the Mumetal canister was measured to be 19.56 ± 0.08 °C. At 19.56 °C, the viscosity of the fluid was found to be $\nu = (1.3976 \pm 0.0036) \text{x} 10^4$ mm^{2}s^{-1} and the density was found to be 975 ± 1 kgm^{-3}.

The increase in viscosity meant that the time-scale associated with the gravitational torque, which acted on the sphere to return it to the zero-field position, increased to $T_0 = 39.43 \pm 0.31$ s. Furthermore, an applied field of greater strength (~ 2.7 mT) was required to produce small-amplitude torsional oscillations of the active sphere. For a frequency of applied field of 0.5 Hz, $\Gamma = 0.0995 \pm 0.0002$, and $\hat{\epsilon} = 0.0081 \pm 0.0001$, the active sphere performed torsional oscillations of amplitude 6.5° in the more viscous fluid. The maximum Re of this system was calculated to be $\approx 5 \text{x} 10^{-4}$.

Lowering the Re resulted in a change in the dependence of the phase lag on separation distance as shown in Figure 5.9. The red line denotes the least-squares linear fit to the low-Re experimental data (represented by the blue markers) and has the form $\sigma = 0.0558(h/a_A) - 0.0954$. The black line has the form $\sigma = 0.2075(h/a_A) - 0.2577$ and denotes the least-squares linear fit to the data presented in Figure 5.8 for which $0.01 \lesssim Re \lesssim 0.1$. The reduction in phase lag that occurred for a reduction of Re suggests that inertial effects are present in the experiments. This is because, although the oscillatory motion of the sphere results in a phase difference that is dependent on distance, the phase difference is not dependent on viscosity and should not, therefore, be

133

Figure 5.9: The phase difference between the torsional oscillations of the active sphere and the translational oscillations of the passive sphere measured as a function of the separation distance for $Re < 5\mathrm{x}10^{-4}$. The red line denotes the least-squares linear fit to the low-Re data (represented by the blue markers) and has the form $\sigma = 0.0558(h/a_A) - 0.0954$. The black line denotes the least-squares linear fit to the data presented in Figure 5.7 which has the form $\sigma = 0.2075(h/a_A) - 0.2577$.

altered by a reduction in Re. The non-zero phase difference obtained in the experiments may also, however, be attributed to the spheres drifting in the fluid because of convection in the tank or slight differences in density which result in buoyancy effects.

Although the reduction in Re suppressed inertial effects in the system, the flow field which resulted from the interaction of the two spheres remained qualitatively the same. The amplitude of the translational oscillations of the passive sphere, A_P, was shown to decrease with increasing separation distance, h, as shown in Figure 5.10. The low-Re experimental data is denoted by the blue markers and the black line denotes the fit to the data presented in Figure 5.7 for which $0.01 \lesssim Re \lesssim 0.1$. When non-dimensionalised accordingly, the low-Re data collapses onto the curve obtained in §5.3 which suggests that the flow field is qualitatively the same for both scenarios. This indicates that although not negligible, inertial effects are small.

5.5 Summary

The interaction between an active sphere performing torsional oscillations and a passive sphere in a viscous fluid has been studied. Qualitatively similar behaviour was observed for spheres of equal and unequal radii and this behaviour was independent of whether the active sphere was larger or smaller than the passive sphere. The motion of the passive sphere was determined by the flow field of the actively rotating sphere.

The active sphere executed rotary oscillations which resulted in translational and rotational oscillations of the passive sphere. The translational motion of the passive sphere followed an arc-like trajectory, the radius of

135
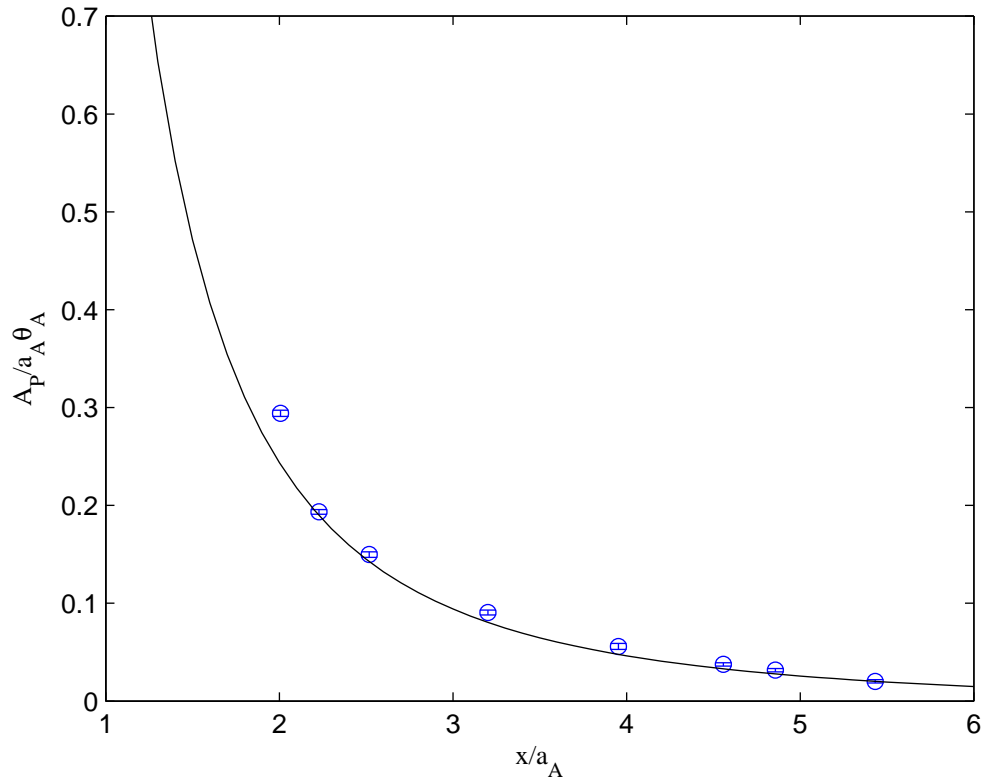
Figure 5.10: The amplitude of translational oscillation of the passive sphere measured as a function of the separation distance for $Re < 5 \text{x} 10^{-4}$. The amplitude of translational oscillation has been non-dimensionalised by the arc length subtended by the active sphere in a torsional oscillation, and the separation distance between the centres of the spheres has been non-dimensionalised by the radius of the active sphere. The amplitude of the torsional oscillations of the active sphere was $\sim 6°$. The experimental data is denoted by the blue markers and the black line denotes the fit to the data presented in Figure 5.7.

curvature of which increased with the radius of the passive sphere until, for a sphere of diameter 15.86 ± 0.01 mm, oscillations were only observed along a straight line in the vertical direction. The amplitude of the translational motion of the passive 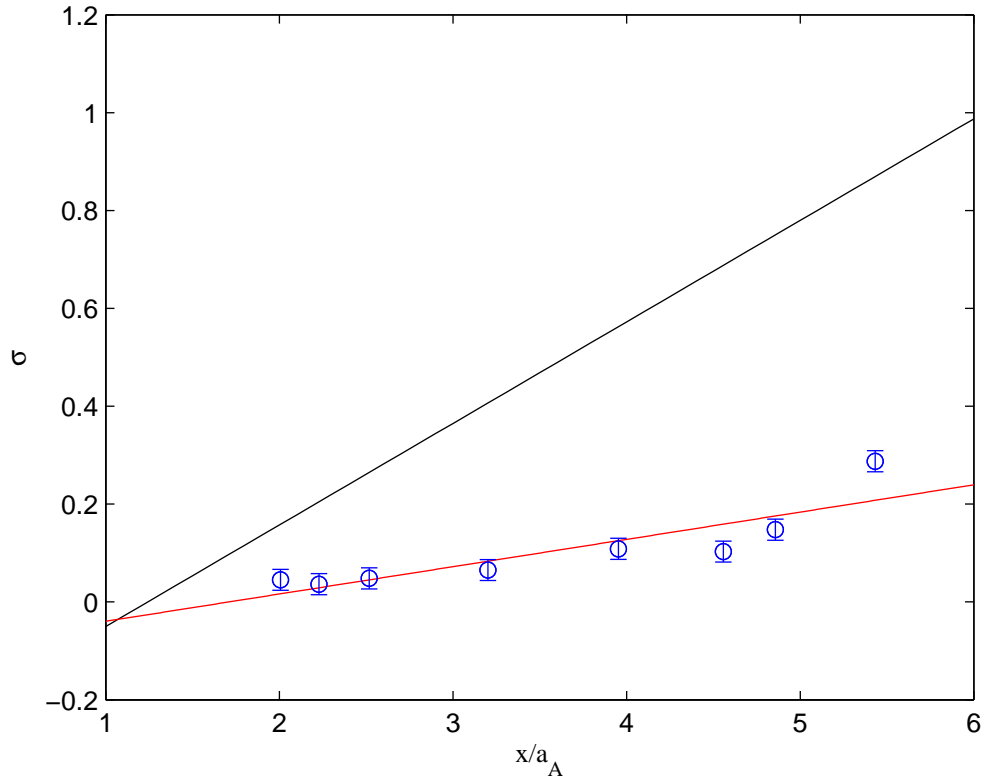sphere, A_P, decreased with increasing separation distance between the spheres. A phase lag between the torsional oscillations of the active sphere and the translational oscillations of the passive sphere was detected and shown to increase with increasing separation distance. The phase difference was attributed to a wave that forms in the fluid because of the unsteady motion of the active sphere. Small inertial effects, however, may also contribute to the phase lag. The amplitude of rotation of the passive sphere was smaller than that of the active sphere and also decreased with increasing separation distance.

For small separation distances, a suppression of the amplitude of rotation of the active sphere was observed and comparable in magnitude to that found when a perpendicular boundary was in close proximity to an actively rotating sphere. The suppression was a consequence of the viscous effects which arise because of the no-slip condition on the surfaces of the two spheres. As the spheres were brought even closer together so that they were almost in contact, $h \rightarrow h_{min}$, the active sphere was observed to perform small translational oscillations in the direction perpendicular to the line joining the centres of the two spheres. The force driving the motion of the active sphere was thought to arise from the viscous shear which develops between the two spheres at small separations. The induced translation of the active sphere was greater when nearby a passive sphere than a stationary, planar boundary which suggests that the motion of the two dynamic spheres was closely coupled.

Non-dimensionalisation of A_P by the arc length subtended by the active sphere, $s = a_A \theta_A$, led to a collapse of the experimental data onto a single curve. This suggested the flow field was similar for spheres of equal and unequal radii. Deviation from this curve occurred for small separation distances at which the active sphere performed translational oscillations as well as torsional oscillations. In these instances, the flow field was different to that produced by an active sphere solely rotating in a viscous fluid. Having generalised the dynamic behaviour of an active and a passive sphere interacting in a viscous fluid, the effect of tethering the two spheres together on the dynamics of the system is investigated in Chapter 6.

Chapter 6

Tethered Spheres

In this Chapter, results are presented for an investigation of spheres connected together by thin tethers. In §6.1, the dynamics of a pair of tethered spheres is studied by comparing and contrasting tethers of different lengths and materials. In §6.2, a specific arrangement of connected spheres is described that comprises two active spheres and one passive sphere connected by elastic tethers of unequal length. When subjected to an applied, alternating magnetic field this multi-body configuration of spheres was observed to propel itself through a viscous fluid. The complex behaviour of this magnetically-actuated swimmer is detailed and its locomotive mechanism is described.

6.1 Two Tethered Spheres

Experiments on tethered spheres were conducted using an active and a passive sphere of equal diameter, 12.70 mm, tethered together by glass, elastic or cotton connectors. The rigid glass rods were of circular cross-section, of

diameter 1.8 ± 0.1 mm and lengths 2.8 ± 0.1, 6.9 ± 0.1 and 12.7 ± 0.1 mm. The elastic struts were segments of silicone rubber which had a cross-section of 1.2 ± 0.1 mm x 1.2 ± 0.1 mm and lengths 3.2 ± 0.1, 6.1 ± 0.1, 10.0 ± 0.1, 15.0 ± 0.1, 21.0 ± 0.1 and 25.2 ± 0.1 mm. The flexible cotton string had an approximately circular cross-section of diameter 1.4 ± 0.1 mm and lengths 3.4 ± 0.1, 6.5 ± 0.1, 12.2 ± 0.1 and 19.7 ± 0.1 mm were used. The two ends of each connection were glued to the surfaces of the two spheres such that the major axis of the connecting tether was approximately parallel to the axis of magnetic dipole of the active sphere. The tethered spheres were submerged in the fluid with $\nu \sim 922$ mm^{2}s^{-1} and subjected to an applied magnetic field of frequency 0.5 Hz, for which $\Gamma = 1.1521 \pm 0.0070$ and $\hat{\epsilon} = 0.0357 \pm 0.0001$.

A striking consequence of linking the spheres was that the reaction to the actuation of the tether caused the reorientation and displacement of the active sphere. Hence, rather than performing rotational oscillations about a fixed position, the active sphere oscillated whilst moving through the fluid. Thus, both spheres prescribed a periodic trajectory and the fluid motion was a consequence of the coupled motion of the spheres. The period of the trajectories was determined by the frequency of the applied field. The trajectories traced out by the spheres were determined by tracking the positions of the centres of mass of the individual spheres in y-z coordinates. The glass rods, elastic struts and cotton tethers are studied individually as a function of length in §6.1.1, §6.1.2 and §6.1.3, respectively, prior to a discussion of the effect of the material of the tether on the collective behaviour of the two spheres in §6.1.4.

Figure 6.1: The trajectories of the active (left) and passive (right) spheres, connected by a rigid glass rod of length 2.8 mm, throughout 8 periods of oscillation.

6.1.1 Glass Connector

The simplest orbits were exhibited by the spheres connected by rigid glass rods. The magnetic torque acting on the magnet embedded in the active sphere caused the spheres to pivot about their collective centre of mass which was located approximately half-way along the rod connecting the spheres. Hence, the two spheres performed a see-saw motion about this fulcrum, each sphere prescribing an arc-like orbit through the fluid. The qualitative shape of the trajectories of the spheres was found to be independent of the length of the tether connecting the spheres. The trajectories shown in Figure 6.1 are the positions, in y-z coordinates, of the respective centres of mass of the active and the passive sphere through 8 periods of oscillation when connected by a glass rod of length 2.8 mm.

6.1.2 Elastic Tether

The flexibility and resistance to curvature introduced by the elastic tether led to both the active and the passive spheres prescribing more complex trajectories than those observed for the spheres tethered by glass rods. Furthermore, the trajectories were qualitatively different for short and long elastic tethers.

For elastic tethers of length $l_T \geq 10.0$ mm, the projection of the trajectory of the active sphere in the y-z plane contained a cross-over point where the sphere appeared to cross over the path it had already traced, as shown in Figure 6.2. The trajectories shown in Figure 6.2 are the positions of the centres of mass of the active and passive spheres, connected by an elastic strut of length 25.2 mm, over 10 periods of oscillation. The cross-over arose because the increased flexibility of the longer elastic strut introduced a small 3D component into the periodic trajectory of the sphere. For short, less flexible elastic connections, $l_T \leq 6.1$ mm, the sphere orbits are very similar to that of the rigid connection; the cross-over in the orbit of the active spheres was not observed, as shown in Figure 6.3 for a elastic strut of length 3.2 mm. The distance travelled by the passive sphere in one orbit increased as the length of the connecting tether was reduced because it experienced less viscous drag. The asymmetry in the orbits shown in Figures 6.2 and 6.3 was thought to arise because the zero field orientation of the magnetic-dipole axis of the active sphere was not precisely orthogonal to the applied field, $\theta_0 \neq 0$, and the tether was not precisely parallel to the magnetic-dipole axis.
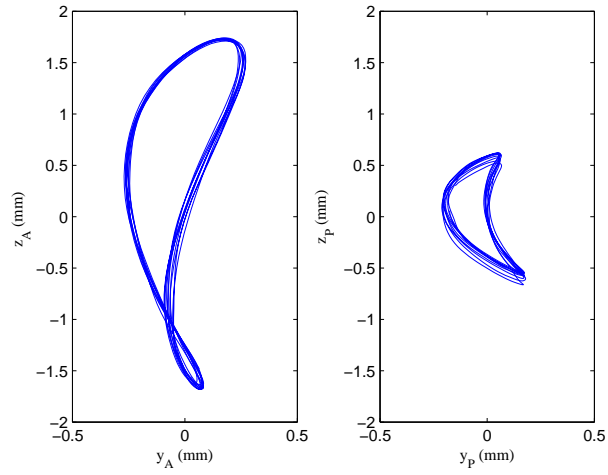
Figure 6.2: The trajectories of the active (left) and passive (right) spheres, connected by an elastic strut of length 25.2 mm, throughout 10 periods of oscillation.
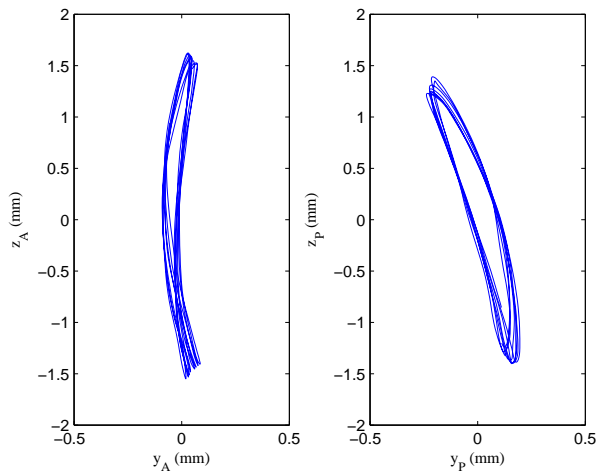
Figure 6.3: The trajectories of the active (left) and passive (right) spheres, connected by an elastic strut of length 3.2 mm, throughout 8 periods of oscillation.

6.1.3 Cotton Tether

The flexibility of the cotton tether resulted in trajectories of the active sphere which were qualitatively similar to those observed for an active sphere tethered by an elastic strut. However, since there was no elastic restoring force acting to separate the spheres this resulted in orbits of the passive sphere which were unlike those exhibited by passive spheres tethered by an elastic strut.

The trajectories shown in Figures 6.4 and 6.5 are for spheres connected by flexible, cotton tethers of length 19.7 mm and 3.4 mm, respectively. For a long cotton tether, $l_T \geq 12.2$ mm, the projection of the orbit of the active sphere contains a cross-over point. Whereas, for short cotton tethers, $l_T \leq 6.5$ mm, the cross-over was not observed in the trajectory of the active sphere. The orbit of the passive sphere was approximately in a straight line for both short and long tethers. This behaviour was a consequence of the one-sided constraint present in the system: the tether was not extensible and the separation between the spheres could not exceed the length of the tether, however no restoring force acted to maintain the separation between the spheres.

Though initially taut, because of the one-sided constraint the tether may have momentarily slackened and effects of the flow on the motion of the passive sphere may have become more significant. The noise in the trajectory data of the passive sphere was attributed to tightening and slackening of the tether, and the competition between the effects of the tether and the flow on the motion of the passive sphere.
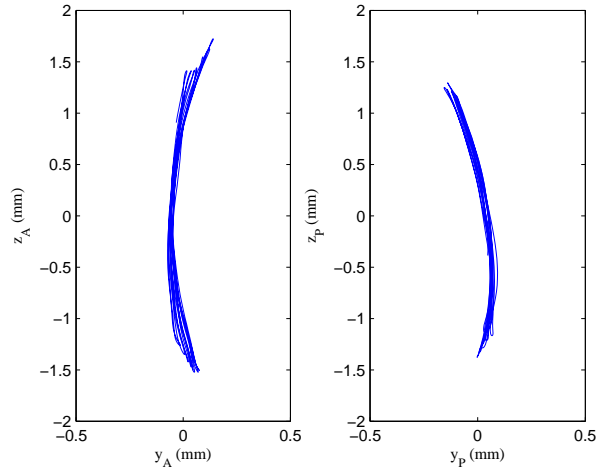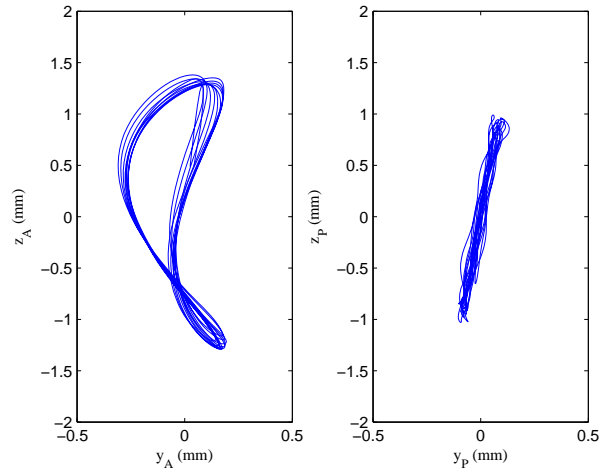
Figure 6.4: The trajectories of the active (left) and passive (right) spheres, connected by a cotton tether of length 19.7 mm, throughout 10 periods of oscillation.
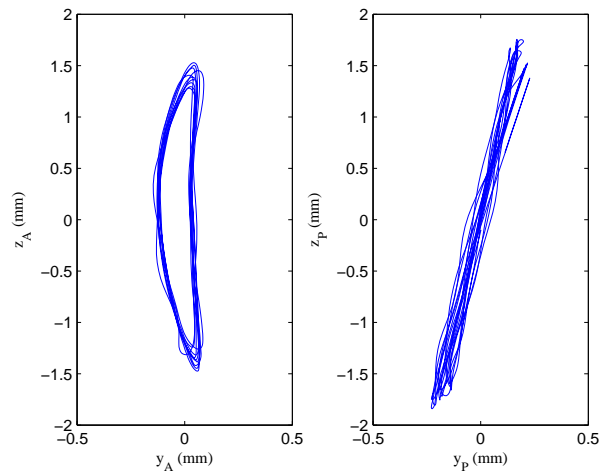
Figure 6.5: The trajectories of the active (left) and passive (right) spheres, connected by a cotton tether of length 3.4 mm, throughout 10 periods of oscillation.

6.1.4   Discussion

The introduction of a tether connecting two interacting spheres alters the dynamics of two interacting spheres. The reaction forces which arose from the actuation of the tether caused the displacement of the active sphere such that it prescribed a periodic trajectory whilst simultaneously performing torsional oscillations. The passive sphere was dragged through the fluid by the actuated tether. Contributions to the motion of the passive sphere from the flow were small compared to the effects of the moving tether, except for a momentarily slackened cotton tether which allowed a greater contribution to result from the flow.

Interestingly, the total distance travelled in one orbit by both the active and the passive sphere, C, increased with decreasing length of connecting tether, l_T, as shown in Figure 6.6. This suggests longer connections were subjected to greater viscous drag and/or bent more (in the case of non-rigid connections). A manifestation of the viscous drag acting on the tether and passive sphere was the reduction of the torsional motion of the active sphere. All connections reduced the torsional response of the active sphere to the applied field by at least a factor of two compared to a single, free sphere subjected to the same applied field. A rigid connection reduced the torsional response of the active sphere most significantly, and an elastic tether reduced the torsional motion more than a flexible cotton tether, which suggests that increases in flexibility of the connecting material allowed greater rotary motion of the active sphere. Furthermore, the torsional motion executed by the active sphere reduced with decreasing length of the connecting tether.

The bending of a non-rigid connection resulted in the active and passive
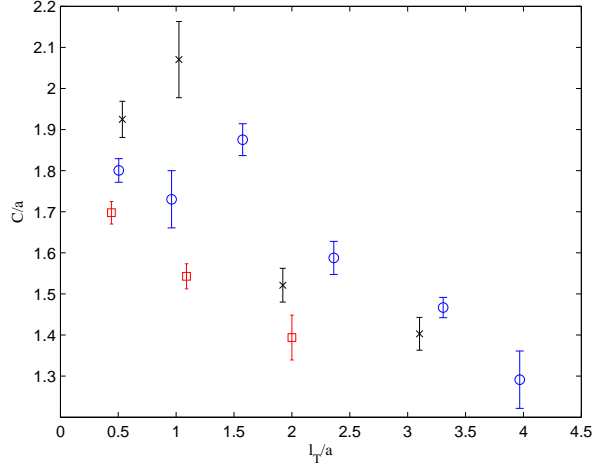
Figure 6.6: The total distance travelled by the active and passive sphere in one orbit measured as a function of length of the connection between the two spheres. Data shown for cotton tethers (x), elastic struts (o) and rigid glass rods ($\square$).

sphere prescribing more complex orbits than was observed for the spheres connected by glass rods. For non-rigid tethers, a qualitative change in the dynamic behaviour of the active sphere was observed for $l_T \lesssim a$ and $l_T \gtrsim a$, where a is the radii of the two spheres. For $l_T \gtrsim a$, a cross-over point was observed in the projection of the orbit of the active sphere and attributed to the increased flexibility of the longer struts causing out-of-plane motion of the active sphere.

The flexibility of the non-rigid connections also introduced a phase difference between the actuation of the active sphere and the response of the passive sphere. The phase difference increased with increasing length of tether and was greater for the elastic tethers than for the cotton tethers of the same length. Furthermore, the increased flexibility of the longer tethers

147

caused the passive sphere to orbit a smaller trajectory as the tether would bend more. Struts with $l_T \lesssim a$ were less flexible and the collective motion of the spheres was more similar to that of spheres connected by rigid tethers.

The motion of two tethered spheres was found to be reciprocal and would not, therefore, result in the propulsion of the configuration at low Re [55]. Although it must be noted that if two spheres were connected by a sufficiently long and flexible tether then, on actuation of the active sphere, bending waves would propagate along the tether towards the passive sphere [76]. The non-reciprocal motion of such a tether, and the flow it would induce, may result in the propulsion of the configuration.

In §6.2, the understanding gained from studying the interaction of tethered, and untethered, active and passive spheres in a viscous fluid is used to provide insight into the locomotive mechanism of a magnetically-actuated swimmer developed by Endao Han during the course of his MPhys project [96]. The swimmer consisted of an arrangement of active and passive spheres tethered with elastic struts and was observed to self-propel itself in an experimental realisation of a Stokes flow. Elastic struts were deemed to be suitable connections because they were flexible yet resisted curvature and therefore introduced a restoring force which acted to maintain the separation between the spheres.

6.2 Swimmer

For a body to swim in a Stokes flow it must deform in a periodic, non-reciprocal manner [55]. The non-reciprocal motion of multi-body configurations of moving spheres has been studied extensively in mathematical models

and provided simple designs for synthetic swimmers [58–62]. Generally, however, such designs have relied on internal motors that control the motion of the constituent spheres and have, therefore, proved difficult to realise experimentally. The potential for *in vivo* applications means that the development of synthetic swimmers is of bio-engineering importance, as well as of scientific interest [57]. A novel method of fabricating and actuating the non-reciprocal motion of a multi-body configuration of connected spheres is detailed §6.2.1. In §6.2.2, measurements are presented of the motion of the spheres and the generated flow field. A discussion of how the motion of the spheres results in locomotion in a Stokes flow is presented in §6.2.3.

6.2.1 Experimental Design

The swimmer comprised three 12.7 mm diameter spheres which were connected to each other by two thin, silicone rubber struts in the configuration shown in Figure 6.7. The elastic struts had a cross-section of 1.2 ± 0.1 x 1.2 ± 0.1 mm and were 3.0 ± 0.2 and 6.0 ± 0.2 mm long. The inequality of the strut lengths introduced a geometrical asymmetry into the configuration which was the source of the non-reciprocal deformation of the swimmer. Both the end spheres contained a single, cylindrical neodymium magnet and the middle sphere was passive but weighted with copper wire, as shown in Figure 6.7, so it had the same average density as the end spheres. The density of the swimmer was finely adjusted by gluing a few 0.5 mm stainless steel balls to the surface of each sphere so that it was horizontally balanced and neutrally buoyant in the viscous fluid. The walls of the tank were sufficiently far from the swimmer that they had negligible effect on the motion of the swimmer.

The results were mainly obtained using a fluid of viscosity $\nu \sim 922$ mm^{2}s^{-1} in which the swimmer was observed to move with a speed of 1.8 mm per minute when subjected to an applied field of strength 1.1 mT and frequency 0.5 Hz. The swimmer was also observed to self-propel itself in fluid of viscosity $\nu \sim 1.4 \times 10^4$ mm^{2}s^{-1} at a rate of 0.08 mm per minute when subjected to an applied magnetic field of strength 2.8 mT and frequency 0.1 Hz. Observation of the self-propulsion of the swimmer at $Re \sim 10^{-4}$ indicated that the locomotive mechanism was maintained when the configuration was a close approximation to a Stokes flow.

The magnetic-dipole axes of the two active, end spheres were aligned orthogonal to the applied field and the dipole moments of the two magnets were opposite to each other such that the torque induced by the applied field resulted in the rotation of the spheres in opposite directions. Rotation of the end spheres caused the middle sphere to be displaced in the vertical direction. However, the end spheres did not just perform rotary oscillations about a fixed point in the fluid when subjected to an applied field. As a consequence of the interaction between the actuated spheres and the connecting struts, the two end spheres prescribed a trajectory in the fluid whilst simultaneously performing torsional oscillations. The orbits were periodic, with a period equal to that of the torsional oscillations.

The combined result of the motion of the two active, end spheres and the displaced middle sphere was the buckling of the swimmer. When subjected to a sinusoidally-alternating magnetic field, the swimmer buckled periodically in a non-reciprocal, spatially asymmetric manner which propelled the swimmer in the direction of the longest strut. The buckling cycle is depicted in the
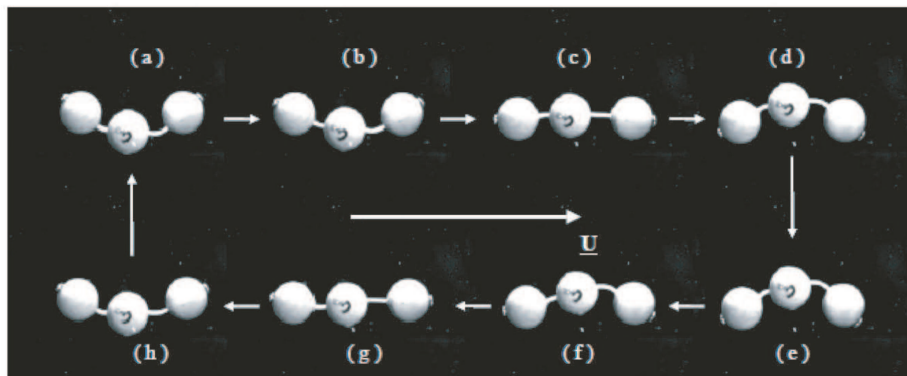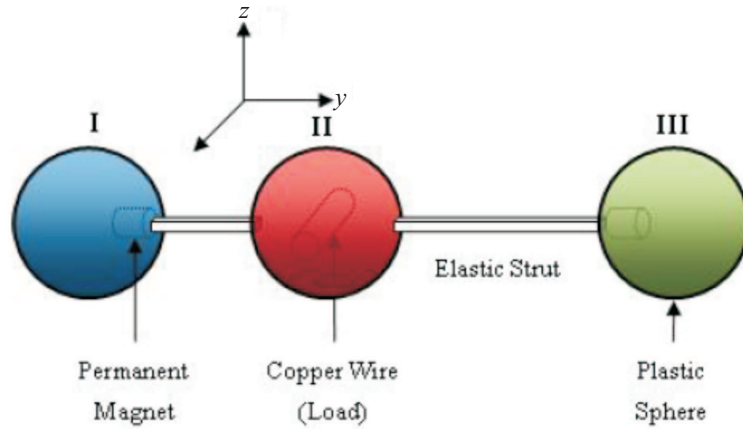
Figure 6.7: Schematic diagram of the swimmer consisting of three spheres connected by elastic struts of unequal length. Permanent magnets were embedded in the active, end spheres (I and III) and the passive, middle sphere (II) was weighted with copper wire. The vertical and horizontal directions of sphere motion were defined to be orthogonal to the observational plane. Eight stages of the non-reciprocal buckling cycle of the swimmer are shown below. The large, white arrow in the centre of the images denotes the direction of the velocity of the swimmer [96].

sequence of images in Figure 6.7. The swimmer in this image was subjected to an alternating field with a frequency of 0.5 Hz and the time interval between images was 0.25 s. The white arrow in the centre of the image denotes the direction of the travel of the swimmer.

6.2.2 Results

The flow fields produced by the rotation of the end spheres and the deformation of the swimmer at $\pi/2$, π and $3\pi/2$ in the non-reciprocal buckling cycle are shown in Figure 6.8. The top and bottom images correspond to the maximum buckling of the swimmer body, and the middle images shows the swimmer in an intermediate state. The individual spheres are depicted by the grey circles and the longer strut connects the middle sphere to the right-hand sphere, as in the schematic shown in Figure 6.7. The black arrowed lines represent the instantaneous particle paths in the fluid and the magnitude of the fluid velocity is represented by the colour contours which range from dark blue (0 mms^{-1}) to dark red (21.5 mms^{-1}). The spatial asymmetry in the flow field is evident throughout the buckling cycle of the swimmer. In the top and bottom images, in particular, more particle paths are directed towards the sphere connected by the longer strut (sphere III). Furthermore, the magnitude of fluid velocity is consistently greater on the longer-strut side of the middle sphere throughout the buckling cycle.

A set of time-series of the amplitude of the applied magnetic field and the individual sphere motion in the horizontal and vertical direction are shown in Figure 6.9. The motion of the spheres are denoted by the blue, red and green data points, in the convention depicted in Figure 6.7. The time-series
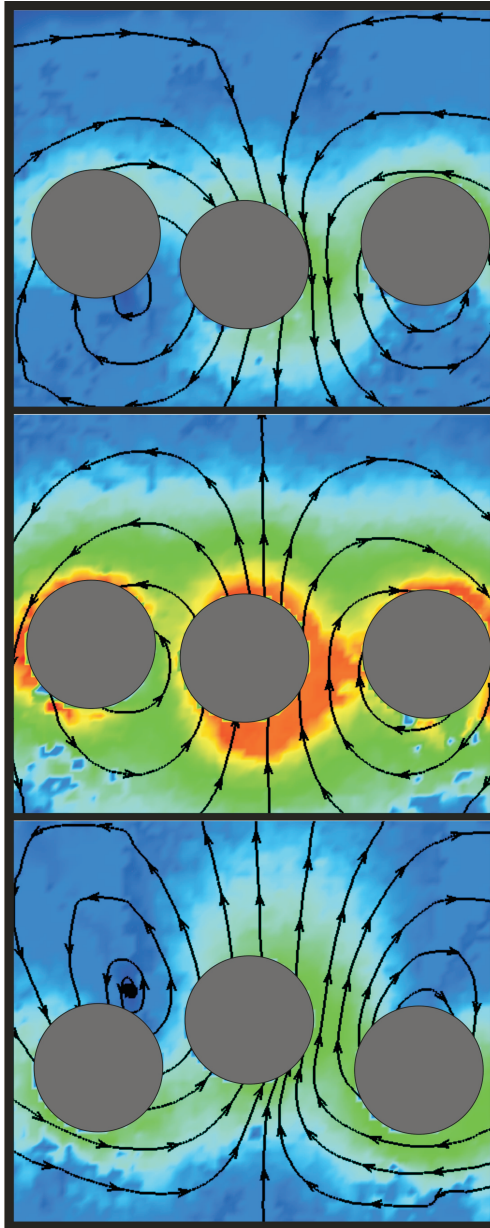
Figure 6.8: Flow visualization of the swimmer at $\pi/2$ (top), π (middle) and $3\pi/2$ (bottom) in the buckling cycle. The spheres are depicted by the grey circles. The black arrowed lines represent the instantaneous particle paths and the colour contours represent the magnitude of the velocity which ranges from 0 (dark blue) to 21.5 mms^{-1} (red).

were obtained for an applied magnetic field with a frequency of 0.5 Hz, the magnitude of which is depicted by the black line.

The horizontal motion of the two active, end spheres are in antiphase (and delayed with respect to the applied field by $\sim \pi/4$) which suggests a longitudinal compression and relaxation of the swimmer about its centre. The horizontal motion of the middle sphere was not time-reversible. The longitudinal motion of the multi-body configuration of sphere was, therefore, non-reciprocal. This is best understood by considering the peak amplitude of the motion of each sphere. After the sphere connected to the shorter strut (sphere I) reaches its maximum positive horizontal displacement, the middle sphere (sphere II) then reaches its maximum positive horizontal displacement and then the sphere connected to the longer strut (sphere III) reaches its maximum[1]. However, after sphere III reaches its maximum negative displacement, spheres I and II reach their maximum negative displacement almost simultaneously.

The vertical motion of the end spheres delays the applied field by $\sim \pi/4$. However, the vertical motion of sphere III has a time-varying phase. The vertical motion of the middle sphere is approximately in antiphase to the other two spheres which confirms that the end spheres react to the applied field and rotate, the rotation of the end spheres then drags the middle sphere through the fluid because of the connecting tethers. The trajectories of the individual spheres in y-z coordinates, through two periods of the buckling cycle, are shown in Figure 6.10. This data was taken with a frequency of applied magnetic field of 0.5 Hz. The spatial asymmetry in the motion of the

---

[1]Convention is that positive displacement in the y-direction is in the direction of the longer strut.

154
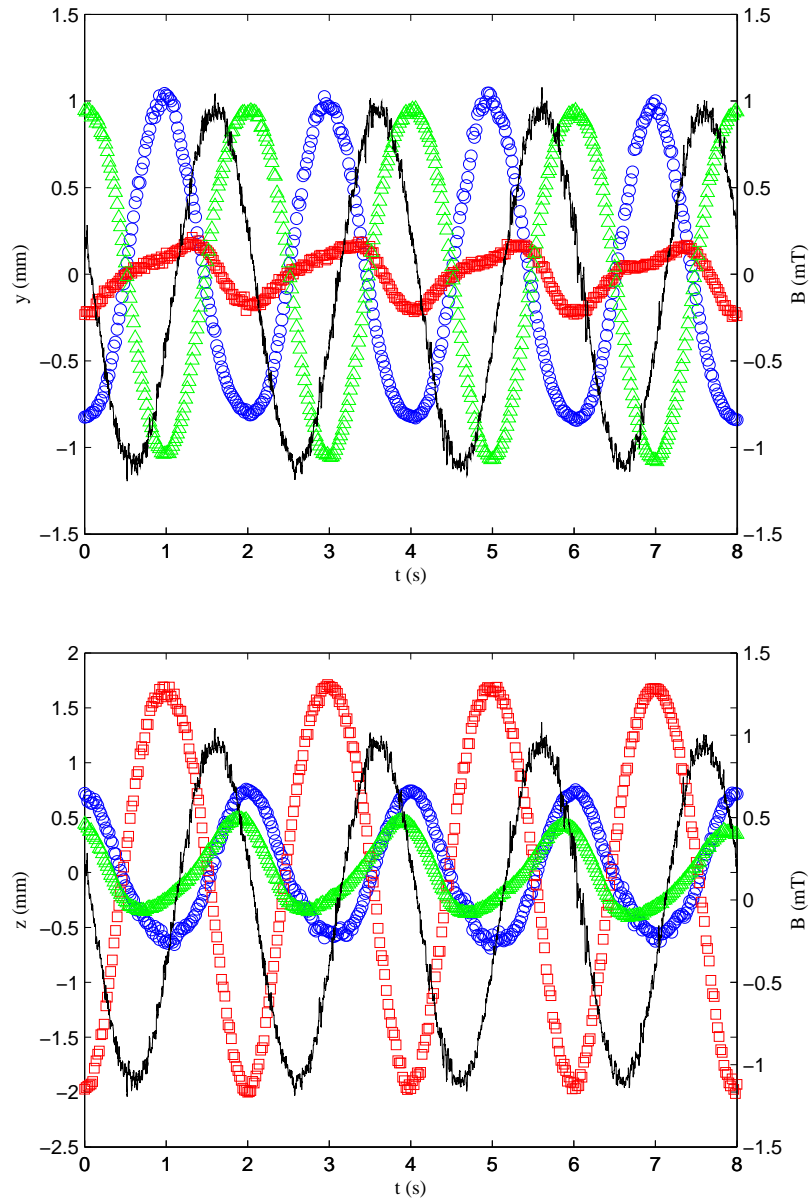
Figure 6.9: Time-series of the horizontal (top) and vertical displacement (bottom) of the three spheres. The motion of active sphere I is denoted by the blue circles (o), passive sphere II by the red squares (□) and active sphere III by the green triangles (△). The applied magnetic field strength is represented by the black line.
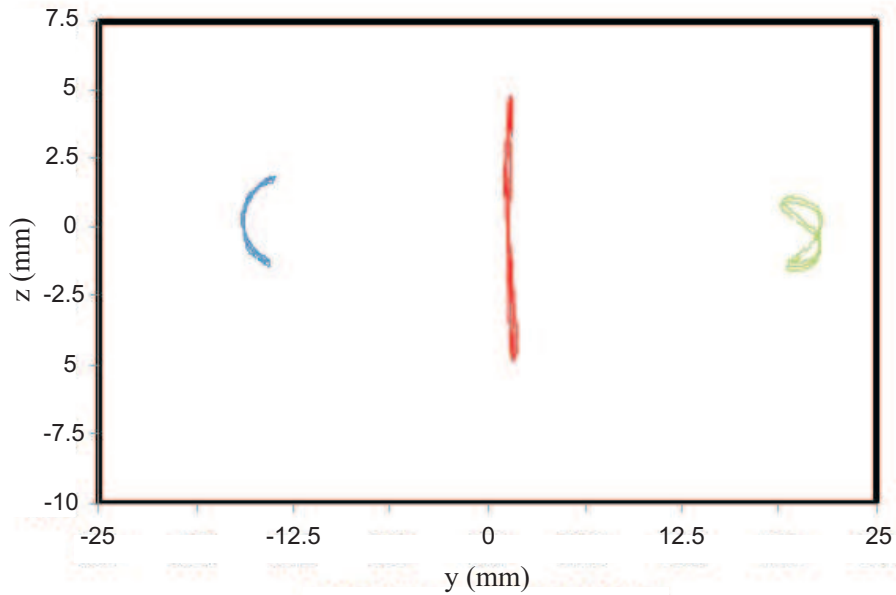
Figure 6.10: The trajectories of sphere I (blue), sphere II (red) and sphere III (green) over two periods. This data was taken with a frequency of applied magnetic field of 0.5 Hz.

individual spheres is evident and determined the direction of the swimmer motion, towards the longer strut and sphere III.

Considering the increased complexity of the arrangement of the three tethered spheres, striking similarities can be made to the simpler arrangement of two spheres tethered by an elastic strut. The projection of the trajectory of the end sphere connected by the longer strut (sphere III) contains a cross-over point and is qualitatively similar to the trajectory of an active sphere connected to a passive sphere by a long, elastic strut. Furthermore, the trajectory of the end sphere connected by the shorter strut (sphere I) is similar to the trajectory exhibited by an active sphere tethered to a passive

156

sphere by a short elastic strut. The contrasting trajectories emphasise the increased flexibility of the longer strut.

6.2.3 Discussion

The inequality in the length of the connecting elastic struts was the source of the geometrical asymmetry in the configuration and the source of the non-reciprocality in the periodic deformation of the swimmer. Kinematic reversibility broke down because the motion of the middle sphere induced by sphere III was delayed with respect to the motion induced by sphere I. The periodic sequence of shapes displayed by the swimmer did not, therefore, satisfy kinematic reversibility and nor did the generated flow. Two contributions to the phase difference between the effects of the end spheres on the middle sphere have been identified:

1. The motion of both end spheres contributes to the dragging of the middle sphere through the fluid. The increased flexibility of the longer strut connecting sphere III, however, results in a phase delay in the dragging of the middle sphere by sphere III compared to the dragging of the middle sphere by sphere I.

2. In the case of two, non-tethered, interacting spheres, the translational oscillations of a passive sphere lag the torsional oscillations of an active sphere that generates the displacing flow, as shown in §5.3. The phase difference was found to be a function of separation distance which implies that the middle sphere responds to the flow generated by sphere I prior to the flow generated by sphere III.

157

The middle sphere, therefore, experiences the combined effects of the motion of the sphere connected by the shorter strut (sphere I) before the effects of the motion of the sphere connected by the longer strut (sphere III). The phase difference between the effects of the end spheres on the middle sphere is not, however, the only effect introduced by the unequal strut lengths.

The difference in strut length has several consequences for the dynamic buckling of the swimmer. As a result of the increased stiffness of the shorter connecting strut, sphere I rotated less and attained a lower angular velocity than sphere III. This suggests the surrounding fluid was displaced with greater speed by the rotation of sphere III than sphere I. However, the increased flexibility of the longer connecting strut resulted in the middle sphere being pulled through the fluid less by sphere III. Furthermore, the separation distance between sphere I and sphere II was small enough that the motion of the passive middle sphere may have induced translational motion of the active end sphere (sphere I); a feedback effect that was observed for two non-tethered interacting spheres at small separations and discussed in §5.2.

Finally, the motion of an end sphere has an indirect effect on the bending of the elastic strut to which it is not connected and the motion of the other end sphere. Therefore, the relative phases of the bending of the individual struts vary as a function of time throughout one period of oscillation. The combination of these effects introduce net geometrical asymmetries into the motion of the spheres, the flow field and the buckling cycle of the swimmer.

One can envisage a swimmer comprising three spheres connected by elastic struts of equal length. The bending amplitude and phase of each strut would be equal and the middle sphere would be driven simultaneously and

equally by the two end spheres. Furthermore, the flow generated by the rotation of the two end spheres would be equal and symmetric about the middle of the configuration, and the middle sphere would be forced in the vertical direction only. This would lead to periodic, reciprocal and spatially symmetric motion throughout the buckling cycle, which would not result in propulsion. Attempts at fabricating a symmetrical swimmer were made, however small asymmetries in the configuration remained and resulted in swimming but at a greatly reduced velocity.

In conclusion, the application of a magnetic field generated a torque which acted on the magnets embedded in the end spheres of a linked chain. The orientation of the magnets was set so that the spheres rotated in opposite directions. The motion of the end spheres transfered a force along the connecting struts and generated a flow which combined to displace the middle sphere. As a consequence of the different lengths of connecting struts, the motion of the two end spheres and their respective displacement of the middle sphere were different. This was a source of net spatial asymmetry in the periodic buckling cycle of the swimmer which determined the directionality of the swimmer motion. The middle sphere responded to the effects of the two end spheres at difference phases in the oscillation cycle. This was a source of non-reciprocality in the periodic buckling cycle of the swimmer which broke the time-reversal symmetry and resulted in self-propulsion. Viewed continuously, a bending wave travelled along the swimmer body from sphere I to sphere III through one period of the buckling cycle. The propagation of this bending wave was in the same direction as the self-propulsion of the swimmer. In other words, the swimmer dragged itself through the fluid.

6.3 Summary

The results of an investigation into the effects of tethering together active and passive spheres have been presented. For the case of a pair of interacting spheres, the introduction of a tether reduced the amplitude of torsional oscillation of the active sphere but also caused the active sphere to prescribe a trajectory in the fluid instead of oscillating about a stationary point in the fluid. The passive sphere also prescribed a trajectory in the viscous fluid. The simplest trajectories were exhibited by spheres connected by rigid tethers. The flexibility of non-rigid tethers introduced a phase delay between the actuation of the active sphere and the response of the passive sphere. Longer non-rigid tethers bent more and thus the passive sphere would prescribe a smaller orbit yet the phase difference between actuation and passive sphere motion was greater.

A swimmer which consisted of an arrangement of tethered active and passive spheres was then studied. The swimmer comprised three spheres connected by elastic struts of unequal length. The two end spheres were active and the middle sphere was passive. On application of an alternating magnetic field the swimmer was observed to buckle in a non-reciprocal manner and self-propel itself through the viscous fluid in the direction of the longest strut. The flow field generated by the swimmer was obtained using PIV and the motion of the individual spheres was detailed. The geometrical asymmetry in the configuration, introduced by the tethers of unequal length, was shown to be the source of net spatial asymmetry and non-reciprocality in the buckling cycle of the swimmer that resulted in propulsion. This novel approach to swimmer design enables the development of a range of multi-

body configurations of oscillating spheres. Furthermore, as the actuation of the swimmer is controlled completely by the interaction of hard magnets and an external field, it would be possible to reproduce the swimmer design at the microscale.

Chapter 7

Summary and Outlook

This study has been concerned with a sphere performing torsional oscillations in a Stokes flow. A systematic experimental investigation was conducted using a novel approach where motion was induced using a non-contact method. Systems of increasing complexity were considered beginning with a single sphere in an effectively unbounded fluid and culminating in the development of a swimmer comprised of an arrangement of connected spheres. The knowledge gained from studying the viscous effects which result from the introduction of nearby boundaries, from asymmetrical systems and from interactions with otherwise stationary spheres provided insight into the locomotive mechanism which propelled the swimmer. In this Chapter, the results are summarised and ideas for future research are outlined.

7.1   One Sphere

A novel experimental set up was developed which enabled the control of the torsional oscillations of a neutrally buoyant sphere in a viscous fluid

through application of an alternating magnetic field. Permanent magnets were embedded into the surface of the sphere and acted as a magnetic-dipole axis which experienced a magnetic torque when subject to an applied field. This magnetic torque acted to align the magnetic-dipole of the sphere with the applied field resulting in the rotational motion of the sphere. Application of a alternating magnetic field resulted in the sphere performing torsional oscillations in the fluid.

This novel experimental approach gives distinct advantages over the use of other methods, such as a torsion pendulum, as it removes from the flow field the uncharacterised effects which are introduced by the motion of the supporting fibre or rod [3–6]. Having developed an experimental technique that enables the control of the torsional oscillations of a free sphere in a viscous fluid, it would be instructive to conduct an investigation of the flow field at high Re and compare the results to the work of Hollerbach et $al.$ [3] in order to determine what effect, if any, the connecting rod has on the resulting flow field.

A model of a a single sphere subjected to an applied field, developed from a balance of the torques acting on the sphere, was described and quantitative agreement was found between the theory and experiments. Two dimensionless parameters were identified that determined the response of the sphere: (1) the magnetic torque term $\Gamma = \frac{Bm}{8\pi\mu a^3\omega}$, where B is the magnetic field strength, m is the magnetic moment of the sphere, μ is the dynamic viscosity of the fluid, a is the radius of the sphere and ω is the angular frequency; and (2) the gravitational torque term $\hat{\epsilon} = \frac{\epsilon}{8\pi\mu a^3\omega}$, where ϵ is the gravitational torque that acts to return the sphere towards the zero applied field orienta-

tion. The gravitational torque term was a consequence of the non-uniform mass distribution within the sphere. Individual spheres had different mass distributions and the model incorporated this accordingly. The angular displacement of any sphere could thus be characterised in terms of Γ and $\hat{\epsilon}$.

Instantaneous measurements of the flow generated by a sphere performing small-amplitude torsional oscillations showed the fluid to move along concentric, circular trajectories around the sphere, and the fluid velocity to decrease with radial distance from the sphere surface. The functional dependence of the fluid velocity on radial distance was compared with the analytical solution for a sphere undergoing steady rotation in an infinite viscous fluid. The quantitative agreement found validated the system as an experimental realisation of a Stokes flow with which previously unstudied flow phenomena could be investigated.

7.2 Boundary Effects

The influence of solid, planar boundaries on the flow field and the motion of the sphere were investigated. Two scenarios were considered: when the normal to the bounding surface is (1) parallel to and (2) perpendicular to the rotational axis of the sphere.

The presence of a parallel boundary in the system did not break the axial symmetry of the system about the rotational axis of the sphere. The no-slip condition on the surface of the boundary introduced a resistive viscous torque which became significant for sphere-wall separation distances $h < \delta + a$, where δ is the thickness of the Stokes layer on the surface of the sphere and a is the radius of the sphere. The viscous torque increased as the sphere approached

the parallel boundary and resulted in the reduction of the velocity of the primary flow and the suppression of amplitude of oscillation of the sphere. In effect, fluid was dragged across the planar surface of the boundary.

The perpendicular boundary intersected the plane of the primary flow generated by the sphere and thus broke the axial symmetry of the system. The primary flow was directed towards and away from the surface of the boundary, where the fluid velocity was constrained to be zero, which resulted in the generation of stagnation points in the flow field. Such stagnation points have been reproduced numerically at $Re = 1$ which indicates the robustness of the flow feature [41]. For sphere-wall separations less than $\delta + a$, the sphere was subjected to a greater viscous torque than in the case of a parallel boundary. For situations where $h \to a$, a viscous shear developed in between the sphere and the boundary and resulted in a wall-parallel force that displaced the sphere in the vertical direction. No evidence was seen for a wall-normal force which may result from a build-up of lubrication pressure and act to separate the sphere from the wall [41]. Frictional effects, however, were observed and resulted from intermittent contact of rough surfaces. This suggests that the effects of surface roughness dominated before a lubrication layer, or a cavitation bubble [44], formed.

The results obtained on the interaction of a torsionally oscillating sphere and a bounding surface could be further investigated by considering a sphere in close proximity to a free surface or a deformable elastic surface. The flow-induced deformation of an interface may led to locomotion driven by the reciprocal motion of the sphere [97]. A viscometer could be developed which comprises a torsionally oscillating sphere in a viscous fluid enclosed by

a concentric spherical shell. This would remove the effects of the mechanical rod or torsion fibre used in similar viscometer designs [7]. When subject to an applied magnetic field, the angular deflection of the sphere would provide an estimate of the viscosity of the fluid.

7.3   Two Spheres

The interaction of a torsionally oscillating sphere and a non-magnetic, passive sphere was studied for combinations of spheres and the observed dynamics were qualitatively similar, independent of whether the active sphere was larger than the passive sphere or *vice versa*.

The flow generated by the active sphere caused the passive sphere to move along an arc-like trajectory. The distance travelled by the passive sphere was comparable to the length of the arc subtended by the active sphere and decreased with increasing sphere-sphere separation distance, h. Appropriate non-dimensionalisation led to the collapse of the data onto a single curve from which the following scaling was obtained: $A_P/a_A\theta_A \sim (h/a_A)^{-2.25}$, where A_P is the amplitude of the translational oscillation of the passive sphere, a_A is the radius of the active sphere and θ_A is the amplitude of torsional oscillation of the active sphere. This generalisation of the motion of the spheres indicates that the flow field was qualitatively similar for the various combinations of sizes of spheres. The gradient in the velocity field induced a shear which resulted in the relatively small rotational motion of the passive sphere in a direction opposite to the torsional motion of the active sphere. Furthermore, the wave induced by the oscillatory motion of the active sphere causes the translational oscillations of the passive sphere to lag the torsional oscillations

of the active sphere.

For small separation distances, $h < \delta + a$, the torsional motion of the active sphere was suppressed by the resistive torque that resulted from the no-slip condition on the surface of the passive sphere. The suppression of rotation increased with decreasing separation distance but was less significant than the reduction in rotation observed in the case of an active sphere near a perpendicular boundary because of the finite size and curvature of the passive sphere. However, the induced translational motion of the active sphere found when the spheres were almost in contact was greater than was observed in the case of the interaction between an active sphere and a perpendicular boundary. This suggests the motion of the passive sphere induced a flow which disturbs the flow field created by the torsional oscillations of the active sphere. This feedback effect rapidly decays with increasing separation and is reminiscent of the higher-order effects which occur in hydrodynamic interactions between pairs of cells [76]. The deviations from the above scaling that occur at very small separations may be attributed to the disturbance flow induced by the passive sphere altering the flow field of the active sphere.

7.4   Tethered Spheres

The effect of linking active and passive spheres was studied using various tethers. As well as being subject to the flow caused by the motion of the active sphere, the passive sphere was dragged through the fluid by the moving tether. The interaction between the actuated sphere and the tether caused the reorientation and displacement of the active sphere. Hence, when tethered together, both spheres prescribed trajectories in the fluid. Elastic teth-

ers were found to be suitable for magnetically-actuated swimming devices as they were flexible yet acted to maintain a separation distance between the spheres by resisting curvature. Furthermore, the bending of elastic tethers introduced a phase delay between the actuation of the active sphere and the response of the passive sphere.

An understanding of the hydrodynamic interaction of untethered and tethered spheres provided insight into the locomotive mechanism of a swimmer which comprised three spheres connected by elastic struts of unequal length with two active end spheres and a passive middle sphere. When subjected to an alternating magnetic field, the swimmer buckled as the two end spheres rotated in opposite directions and displaced the middle sphere in the vertical direction. The buckling cycle of the swimmer was non-reciprocal and a net spatial asymmetry was observed in the generated flow field. The non-reciprocality and net spatial asymmetry were attributed to the unequal strut length and resulted in the self-propulsion of the swimmer.

A more comprehensive investigation into the effects of tethering spheres together is required for better understanding how the length, material properties and geometry of the tether change the complex dynamics of the interacting spheres. It would be informative to study the fluid-structure interaction of a single, active sphere connected to a rod or tether prior to the inclusion of a second, passive sphere. A simple swimmer comprised of an active sphere attached to an elastic filament and subjected to an alternating magnetic field may result. Numerical studies [75] showed that a magnetic dipole with a flexible tail behaves as a swimmer when subject to AC magnetic fields. The torsional oscillations of the swimmer body would actuate

the elastic tail, generating a bending wave that propagates along the elastic filament and propels the swimmer through the fluid [76]. Previously, synthetic swimmers of a similar design have developed by Wiggins *et al.* [77] and Yu *et al.* [78].

Finally, an investigation into the optimal difference in the strut length, and/or material, which results in maximal locomotion of the swimmer is desirable. Furthermore, assembly of a magnetically-actuated swimmer from an arrangement of active and passive spheres leaves opportunities for the development of new swimmers from different configurations of tethered spheres. As a proof of the principle, a second swimmer was produced which swam at a slower rate than the swimmer reported in §6.2. The second swimmer consisted of three spheres connected by elastic struts of equal length. One end sphere and the middle sphere contained magnets, whilst the other end sphere contained no magnet. This meant that the geometrical asymmetry in the configuration resulted from the positioning of the active spheres. The flow field produced at two points in the buckling cycle of the swimmer was obtained using the PIV technique and is shown in Figure 7.1. The spheres are depicted by the grey circles. The sphere on the left-hand side of the image was passive while the other two spheres were active. Net displacement of the swimmer was observed in the direction of the active end sphere i.e. towards the right-hand side in Figure 7.1. The black arrowed lines represent the instantaneous particle paths and the colour contours represent the magnitude of the velocity which ranges from 0 (dark blue) to 9.5 mms^{-1} (red). The asymmetry in the flow field is evident in the direction of net displacement suggesting that the swimmer pulled itself through the viscous fluid. Devel-

opment of a second swimmer constructed from active and passive spheres suggests a multitude of swimmers could be produced using asymmetrical arrangements of connected spheres.
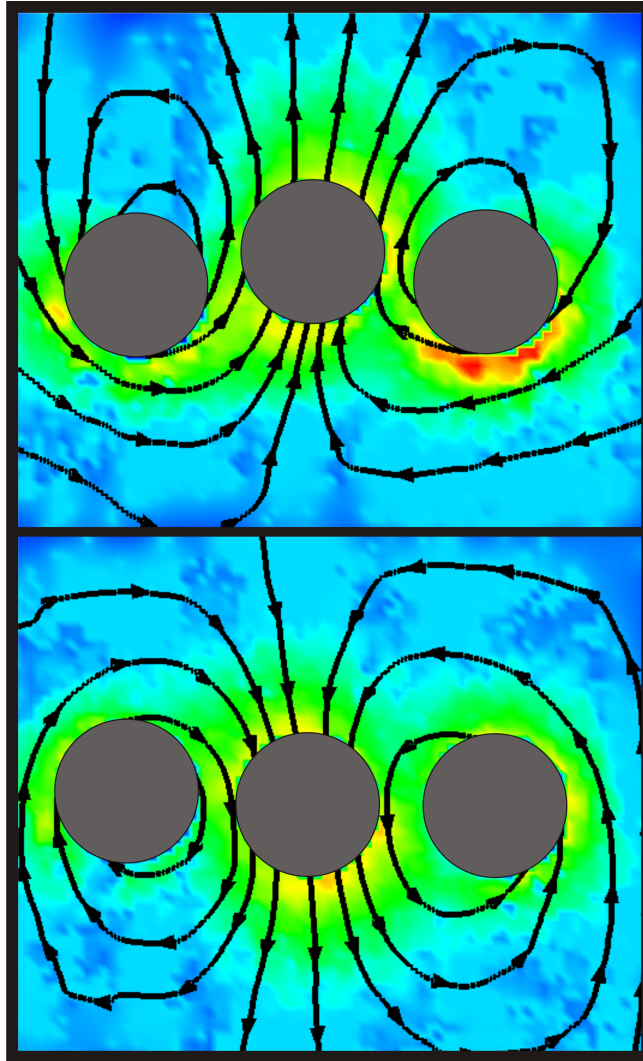
Figure 7.1: Flow visualisation of the second swimmer at $\pi/2$ and $3\pi/2$ in the oscillation cycle. The spheres are depicted by the grey circles. The black arrowed lines represent the instantaneous particle paths and the colour contours represent the magnitude of the velocity which ranges from 0 (dark blue) mms^{-1} to 9.5 mms^{-1} (red). Development of a second swimmer constructed from active and passive spheres suggests a variety of swimmers could be produced using asymmetrical arrangements of connected spheres.

Appendix A

Background Magnetic Field

This appendix concerns a comparative study of the dynamic response of an active sphere with a magnetic-dipole axis to an applied magnetic field with and without magnetic shielding. The background field inside the laboratory was measured and found to be appreciable in direction and magnitude to the geomagnetic field which varies from 25 to 65 μT [81] and, in Manchester, is orientated towards magnetic North and inclined at $\approx 70°$ [98] from the vertical. The Mumetal canister used to shield the experimental system from the background field is described in §2.4 and consistently reduced the strength of this magnetic field by an order of magnitude to less than 5 μT. The strength of the applied fields used in the experiments were typically $0.2 - 3$ mT. All measurements were performed inside the Mumetal canister except flow visualisation measurements because of the technical difficulties involved in simultaneously illuminating and imaging the experimental system whilst the shielding canister was in place. An investigation into the effects of the background field on the dynamic response of the sphere is therefore required to validate the quantitative flow visualisation measurements.

The most significant effect of the background field on an active sphere was to induce a torque which acted to align the magnetic-dipole axis of the sphere parallel to the background field and hence define the plane of rotation. With reference to the coordinate system detailed in Figure 3.1 of §3.2, the background magnetic field perturbed the magnetic-dipole axis of the sphere in the ϕ-direction and the θ-direction. The perturbation in the ϕ-direction resulted from the component of the background field orthogonal to the applied field direction and could be accounted for by positioning the observing camera orthogonal to the component of the background field in the ϕ-direction such that $\phi = 0$. In contrast, when shielded the orientation of the magnetic-dipole axis in the ϕ-direction could be controlled and the sphere was positioned orthogonal to the observation point prior to experimentation such that $\phi = 0$. An orientation of $\phi = 0$ was required in order to image the rotational plane of the sphere. When shielded and subject to zero applied field, a neutrally buoyant sphere sat in the viscous fluid with its magnetic-dipole axis at some angle θ_0 because of the gravitational torque acting on the non-uniform distribution of mass within the sphere. In contrast, when unshielded the initial angular orientation of the sphere in the θ-direction would be a result of the combined gravitational and perturbing, magnetic torque acting on the sphere.

As a consequence of the differences in initial angular orientation of the sphere, a comparative investigation of the response of the sphere to the applied magnetic field required attaining an initial state which was reproducible with and without the magnetic shield. The reproducible initial state was attained by application of a constant, non-zero magnetic field, $\boldsymbol{B_{DC}}$ (of ~ 0.4

mT), in the vertical direction which induced a magnetic torque that resulted in approximate alignment of the spheres magnetic axis with the applied field. Through the superposition of the two magnetic fields, $\boldsymbol{B} = \boldsymbol{B_{AC}} + \boldsymbol{B_{DC}}$, it was then feasible to study the angular response of an active sphere, from the aligned position, as a function of amplitude and frequency of applied, alternating magnetic field.

The angular displacement of the sphere as a function of the frequency of the applied magnetic field was thus measured in both cases, and the results are shown in Figure A.1. The amplitudes of the applied magnetic fields were $B_{DC} = 0.3681 \pm 0.0064$ mT and $B_{AC} = 1.759 \pm 0.0095$ mT for the unshielded case, and $B_{DC} = 0.3952 \pm 0.0084$ mT and $B_{AC} = 1.7194 \pm 0.0062$ mT for the shielded case.

The agreement between the results for the shielded and unshielded cases suggests that, provided the observing camera was positioned such that $\phi = 0$, the components of the perturbing background field which induced or opposed the rotation of the sphere were small enough to be considered negligible and neglected. This validates conducting flow visualisation measurements without the magnetic shield. Provided an appropriate magnetic field was applied to ensure small-angle, sinusoidal oscillations of the sphere then direct comparisons between the two systems is justified. Furthermore, throughout the thesis flow visualisation measurements are presented in terms of the instantaneous surface velocity or angular displacement of the sphere, rather than the applied magnetic field strength of frequency so that the mechanism responsible for driving the sphere need not be considered.
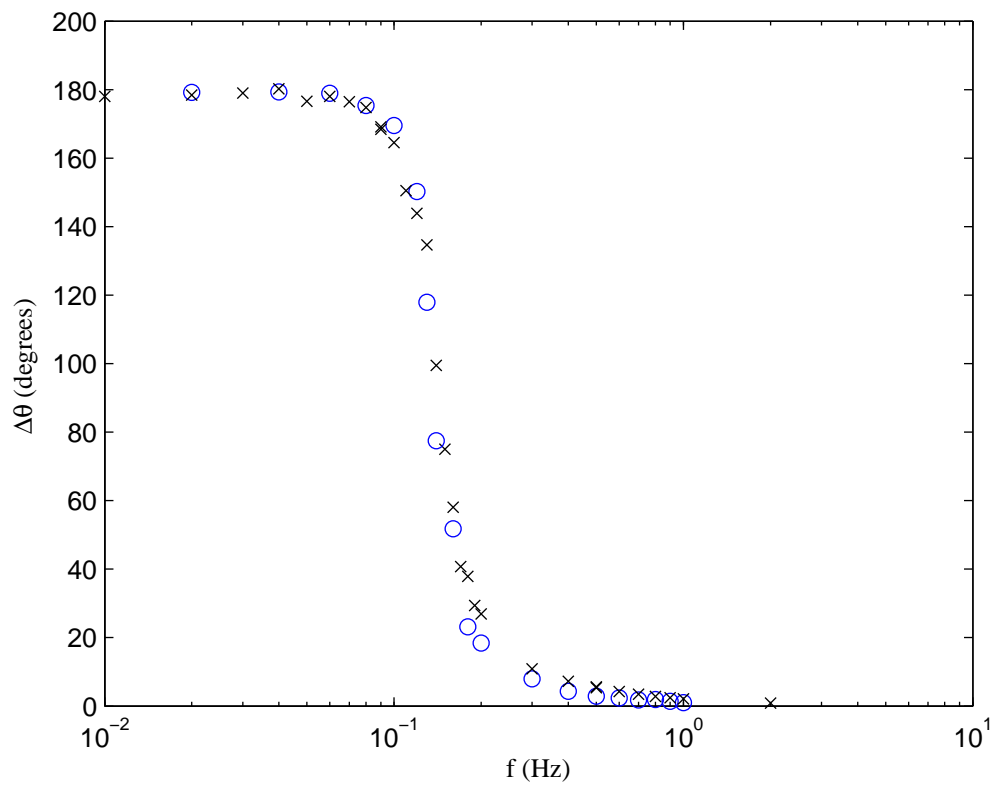
Figure A.1: The total angular displacement of the sphere from the aligned position measured as a function of the frequency of the applied, alternating magnetic field with (o) and without (x) magnetic shielding.

Appendix B

Two Sphere Data

In §5.3, various combinations of equal and unequal radii spheres were studied. The results regarding the motion of the passive sphere and the phase difference between it and the torsional motion of the actively driven sphere were presented in Figures 5.7 and 5.8, respectively. The physical properties of the system are detailed in Table B.1, below, for each of the combinations of spheres. Table B.1 includes the following information: the radii of the active sphere (a_A) and the passive sphere (a_P), the density of the spheres, the fluid viscosity, the magnetic and gravitational torque parameters to which the active sphere was subjected, the time-scale associated with the gravitational torque acting on the active sphere, the approximate amplitude of torsional oscillations of the active sphere when solitary in the fluid and subjected to the applied field, and the angle at which the magnetic-dipole axis of the active sphere resides when subjected to zero applied field.

a_A (mm)	a_P (mm)	ρ_A (kgm^{-3})	ρ_P (kgm^{-3})	ν (cSt)	Γ	$\hat{\epsilon}$	T_0 (s)	θ_A (degrees)	θ_0
7.93	7.93	986.7	983.3	920.11±1.70	0.1191±0.0002	0.1010±0.0002	3.14±0.05	∼ 6	∼ 5.6
7.93	4.77	986.7	975.7	920.13±2.53	0.1247±0.0011	0.1010±0.0003	3.14±0.05	∼ 6	∼ 5.6
7.93	3.17	986.7	984.5	924.07±2.79	0.1152±0.0199	0.1006±0.0003	3.14±0.05	∼ 6	∼ 5.6
6.35	6.35	972.5	977.1	933.85±4.35	0.1257±0.0006	0.0355±0.0002	8.80±0.50	∼ 5	∼ 7.9
7.93	4.77	986.7	975.7	922.28±1.59	0.5923±0.0014	0.1008±0.0002	3.14±0.05	∼ 30	∼ 5.6
7.93	7.93	986.7	983.3	919.49±2.11	1.2241±0.0024	0.1011±0.0002	3.14±0.05	∼ 54	∼ 5.6
6.35	7.93	972.5	983.3	927.68±1.22	0.1655±0.0004	0.0358±0.0001	8.80±0.50	∼ 6	∼ 7.9

Table B.1: A table outlining the the physical properties of the particle-pair combinations studied in Chapter 5. The table includes the following information: the radii of the active sphere (a_A), the radii passive sphere (a_P), the density of the active sphere (ρ_A), the density of the passive sphere (ρ_P), the fluid viscosity (ν), the dimensionless magnetic torque parameter (Γ) and the dimensionless gravitational torque parameter ($\hat{\epsilon}$) to which the active sphere was subject, the time-scale (T_0) associated with the gravitational torque acting on the active sphere, the approximate amplitude of torsional oscillations of the active sphere (θ_A) when subject to the applied field and far from the passive sphere, and the angle at which the magnetic-dipole axis of the active sphere resides when subject to zero field (θ_0).

Appendix C

Model

As intended, the experimental results inspired theoretical collaborations. The author worked with Dr. Kiran Singh[1] who developed a model of the torsionally oscillating sphere interacting with nearby boundaries and passive spheres. The model is based on an oscillating rotlet singularity as is described in §C.1. In §C.2, the the model is developed to include the effects of nearby boundaries and compared with the experimental results presented in Chapter 4. Finally, in §C.3, the modelling process used to compute the interaction between two spheres is described and the predictions of the model are compared with experimental findings presented in Chapter 5.

---

[1] Oxford Centre for Collaborative Applied Mathematics, University of Oxford, UK.

C.1 Model of an Unsteady Body in a Viscous fluid

A particle oscillating in a fluid is subject to unsteady hydrodynamic forces, and therefore knowledge of the time history of the complete system is required in order to find solutions to the governing equations of motion. If the rate of change of fluid motion compared to the diffusion of vorticity is small, however, the particle may be considered to be oscillating in a quasi-steady manner and analytical progress can be made through linearisation of the Navier-Stokes equations [99].

To linearise the system of equations, it is required that the acceleration forces in the fluid dominate over the nonlinear inertia term. Defining an effective frequency parameter $\beta = a^2\omega/\nu$, the requirement is that $\beta >> Re = UL/\nu$, or $U/(a\omega) < 1$. The linearisation assumption requires that the maximum excursion of the fluid particle over a single period of motion must be less than the characteristic particle size, a. Therefore, if a convective tangential speed is defined as $U = \omega\theta_0 a$, the linearisation condition gives $\theta_0 < 1 \approx 57°$. Recalling that all the experimental results presented in Chapter 4, and virtually all the experimental results presented in Chapter 5, were performed at much smaller amplitudes of oscillation, the linearity assumption is valid for modelling purposes.

Following the approach developed by Pozrikidis [100], the quasi-steady linearised Stokes equations are given by

$$\frac{\partial \mathbf{u}}{\partial t} = -\nabla p + \frac{\nu L^2}{T}\nabla^2 \mathbf{u}, \quad \nabla \cdot \mathbf{u} = 0 \qquad (C.1)$$

where u and p are the dimensionless flow speed and pressure respectively,

L is a characteristic length scale ($L \equiv a$) and T a characteristic time scale ($T \equiv 1/\omega$).

The main benefit of the quasi-steady assumption is that many of the tools used to study steady Stokes flows can be applied. For instance, flow reversibility, reciprocal identities and uniqueness properties extend to the quasi-steady case [101].

The rotary oscillations of a sphere in a viscous fluid may be modelled using an unsteady rotlet rotating with angular speed $\Omega_0 e^{i\tilde{\omega}}$, where $\Omega_0 = \tilde{\omega}\theta_0$ and $\tilde{\omega}$ is the dimensionless frequency [100]. The flow speed induced in the fluid at position $\mathbf{r} = (r_1, r_2, r_3)$ from the rotlet is given as

$$\mathbf{U}_u = \mathbf{U}_s \frac{1 + \lambda r}{1 + \lambda} \exp(\lambda(1 - r) + i\tilde{\omega}t), \tag{C.2}$$

where

$$\mathbf{U}_s = \frac{\Omega_0 a^3}{r^3}(-r_2\mathbf{e}_1 + r_1\mathbf{e}_2) \tag{C.3}$$

is the expression for a steady flow generated by a spinning rotlet.

C.2   Rotating Sphere near a Solid Boundary

The experiments indicated that as the sphere was brought closer to a planar boundary, the flow in its vicinity was modified. In particular, the direction of rotation with respect to the wall normal modifies the resulting interactions. Blake *et al.* [102, 103] considered a similar problem of modified Stokes flows in the vicinity of a rigid boundary using a combination of singularities and an image system which enabled the flow field in the vicinity of the wall and the far-field to be established.
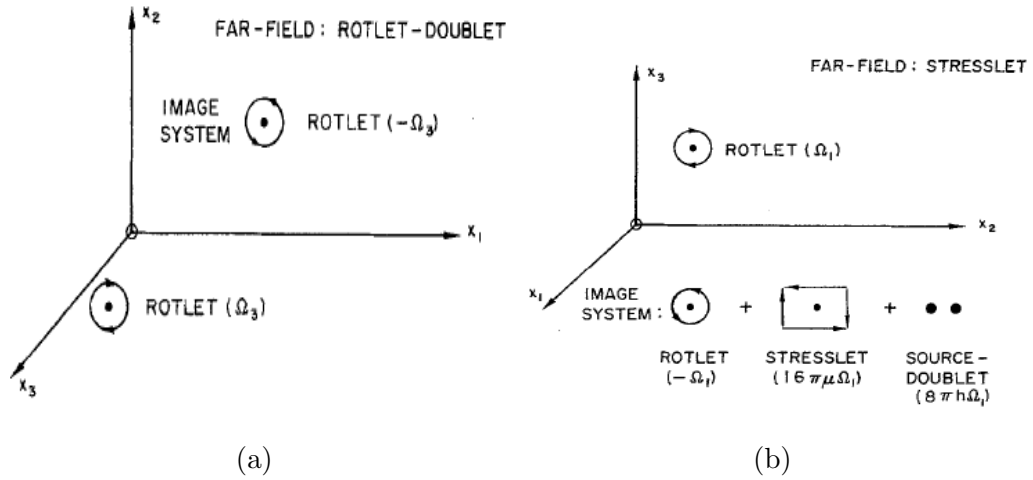
Figure C.1: Schematic diagram illustrating the model with rotlet singularity and corresponding image system for rotation about an axis (a) parallel and (b) perpendicular to the wall normal. In both cases the wall is the (x_1, x_2, x_3) plane [103].

When the oscillating rotlet, representing the sphere, is bought near a no-slip wall the flow field is modified, and the system of image singularities depends on the orientation of the the rotlet rotation axis with respect to the boundary, as shown in the schematic in Figure C.1. The experiments considered two particular cases, rotation about an axis (1) parallel and (2) perpendicular to the wall normal. Using the image system proposed by Blake [103] and including the oscillatory contribution of an unsteady rotlet the nature of the flow field in each case was established.

Case 1: rotlet with axis parallel to the wall normal

In this case the rotlet located in space at $\mathbf{y} = (0, 0, h)$ rotates about the $\mathbf{e}_3$ axis so $\boldsymbol{\Omega} = \Omega e^{i\tilde{\omega}t}\mathbf{e}_3$. The image of reflections yields an image rotlet at

$\tilde{\mathbf{y}} = (0, 0, -h)$ rotating in the opposite sense, so $\boldsymbol{\Omega}_I = \Omega_I e^{-i\tilde{\omega}t}\mathbf{e}_3$.

$$\Omega = \Omega_0 \frac{1 + \lambda r}{1 + \lambda} \exp[\lambda(1 - r)], \tag{C.4}$$

$$\Omega_I = -\Omega_0 \frac{1 + \lambda_I r}{1 + \lambda_I} \exp[\lambda_I(1 - r)], \tag{C.5}$$

where $\lambda = (1 - i)\tilde{\omega}a^2/2\nu$, $\lambda_I = (1 + i)\tilde{\omega}a^2/2\nu$.

The velocity field at an arbitrary point $\mathbf{r}$ from such an image system is

$$\mathbf{u}_{||} = \left(\frac{\Omega}{r^3} - \frac{\Omega_I}{R^3}\right)(-r_2\mathbf{e}_1 + r_1\mathbf{e}_2), \tag{C.6}$$

where $r_i = x_i - y_i$, $R_i = x_i - \tilde{y}_i$, $r = (\sum_{i=1}^{3} r_i^2)^{1/2}$, and $R = (\sum_{i=1}^{3} R_i^2)^{1/2}$.

Case 2: rotlet with axis perpendicular to the wall normal

When the axis of rotation is perpendicular to the wall normal $\boldsymbol{\Omega} = \Omega\mathbf{e}_1$, the flow field, given by

$$\mathbf{u}_\perp = (0, u_2, u_3), \tag{C.7}$$

where

$$u_2 = -\left(\frac{r_3\Omega}{r^3} - \frac{\Omega_I R_3}{R^3}\right) - 2h\Omega_I\left(\frac{1}{R^3} - \frac{3R_2^2}{R^5}\right) - 6\Omega_I\frac{R_2^2 R_3}{R^5} \tag{C.8}$$

$$u_3 = \left(\frac{r_2\Omega}{r^3} - \frac{\Omega_I R_2}{R^3}\right) + 6h\Omega_I\frac{R_2 R_3}{R^5} - 6\Omega_I\frac{R_1 R_2 R_3}{R^5} \tag{C.9}$$

is no longer symmetric in the equatorial plane. In this case the image system at $\tilde{\mathbf{y}} = (0, 0, -h)$ comprises not only an oppositely rotating rotlet, but a source doublet and a stresslet which dominates in the far-field.

Contour maps are shown in Figure C.2b of the instantaneous velocity field in the equatorial plane of a rotlet with its centre a distance $h/a = 1.36$ from the wall rotating about an axis parallel (a) and perpendicular (b) to the wall normal. These snap-shots of the flow field qualitatively capture the same flow phenomena observed experimentally for a sphere performing torsional oscillations nearby solid boundaries.
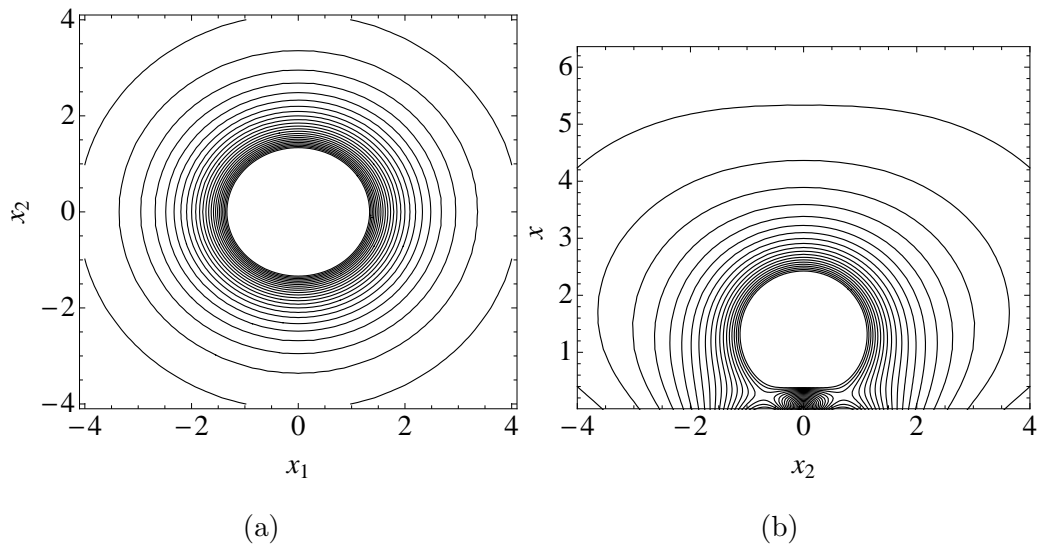
Figure C.2: Contour map of the instantaneous velocity field in the equatorial plane of a rotlet rotating about an axis (a) parallel (along $\mathbf{e}_3$) and (b) perpendicular (along $\mathbf{e}_1$) to the wall normal, where the wall normal is along $\mathbf{e}_3$. For both, the rotlet is a distance $h/a = 1.36$ from the wall, and for the oscillatory rotlet $\omega = 2\pi(0.15)$ rads^{-1}.

C.2.1 Wall Induced Suppression of Rotation

As found in the experiments, boundary effects influenced the amplitude of rotation of the sphere when the sphere was moved closer to the wall. For a fixed applied magnetic field, the amplitude of rotation, θ_0, reduced as the wall was approached. The model of the sphere as a rotlet renders it independent of a length scale. In order to account for finite size effects, the flow field is interrogated around the sphere at a unit radial distance from the centre which is equivalent to a measurement on the surface of the sphere. The flow field is treated as a linear superposition of the velocity field generated by the rotlet, $\mathbf{v}_\infty$, far away from the wall, with a perturbation velocity field, $\mathbf{v}$ generated by the sphere rotation in the vicinity of the wall. The net velocity vector is $\tilde{\mathbf{v}}(h) = \mathbf{v}_\infty + \mathbf{v}(h)$. Correspondingly, if θ_∞ is the amplitude of rotation when the sphere is far from the wall, the tangential velocity of the sphere far from the wall is $v_s = \theta_\infty \omega a$. As the wall is approached this surface velocity is modified to

$$\tilde{v}_s(h) = \omega a \tilde{\theta}_0 = v_s + \langle \mathbf{v}(h; r = a) \rangle \tag{C.10}$$

$$\tilde{\theta}_0(h) = \theta_\infty + \langle \mathbf{v}(h; r = a) \rangle / \omega a \tag{C.11}$$

where $\langle \mathbf{v} \rangle$ is the average velocity perturbation measured around the circumference of the sphere, in the equatorial plane, and $\tilde{\theta}_0$ is the effective amplitude of rotation of the sphere, where $\tilde{\theta}_0/\theta_\infty \to 1$ as $\mathbf{v} \to 0$.

In Figure C.3, the effect of the walls parallel and perpendicular to the rotation axis are compared. For both cases a reduction in $\tilde{\theta}_0$ as $h \to 1$ is observed. Qualitatively consistent with the experiments, in the perpendicular case the wall has a stronger influence in reducing the rotation amplitude and the velocity of the surface.
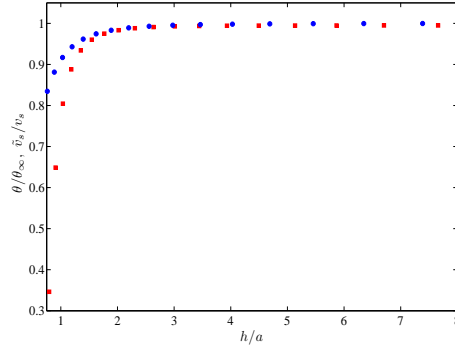
Figure C.3: The predicted, normalised amplitude of torsional oscillation and surface velocity of a sphere, measured as a function of separation distance from a wall, with its axis of rotation parallel (o) and perpendicular (□) to the wall normal.

C.2.2 Fluid Velocity Modified near the Wall

In the experiments spheres were positioned at varying distances, h, from the wall and measurements of the fluid velocity were taken in the equatorial plane of the sphere. The expression for the rescaled flow velocity from equations C.6-C.7 for $x \in (0, h-1)$ is

$$U_{||} = \frac{u_{||}(0, x, h)}{\tilde{v}_s} \tag{C.12}$$

$$U_{\perp} = \frac{u_{\perp}(0, 0, -x + h)}{\tilde{v}_s}. \tag{C.13}$$

In Figure C.4 the flow velocity variation with distance predicted by the model and the experimental findings as compared for the two cases. The agreement suggests that the linearised flow assumption was valid.

185
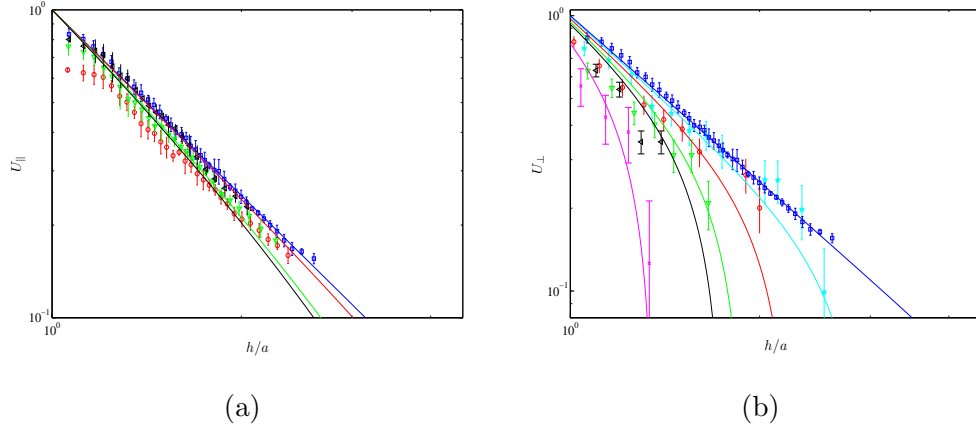
Figure C.4: Fluid velocity variation with distance from the sphere centre with axis of rotation (a) parallel and (b) perpendicular to the wall normal, for a sphere with centre h/a away from the wall. Symbols correspond to experimental data, solid curves indicate the oscillatory model.
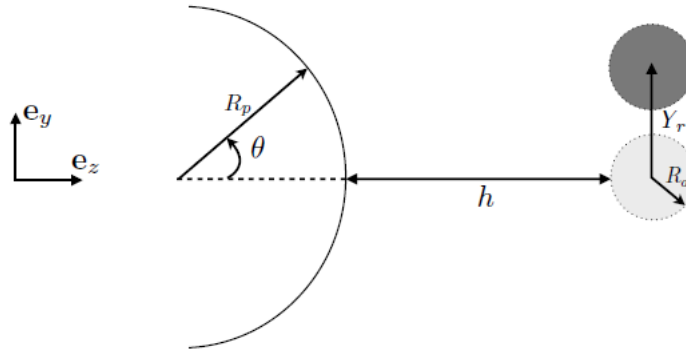
Figure C.5: Schematic diagram illustrating the active sphere (in grey) with radius R_a near a spherical boundary wall of radius R_p. When the centres of the spheres are aligned the rotlet to wall distance is $h + R_a$, if the centres are offset by Y_r, then the rotlet-wall distance increases by an amount $R_p(1-\sin\theta)$, where $\theta = \cos^{-1}(Y_r/R_p)$.

C.3 Two Sphere Interactions

The modelling of the coupled motion of the passive sphere and the active rotlet comprises three steps. First the passive sphere is treated as a curved moving boundary and its effects on the active sphere are computed. For reference, a sketch of the two sphere interaction is shown im Figure C.5. The rotating sphere (radius R_a) is positioned with its centre aligned with a spherical wall of radius R_p. The distance between the rotlet centre and the boundary wall (rescaled by R_a) is $1+h$. The horizontal distance of the rotlet from a passive sphere of radius R_p with its centre at $(0, Y_p, Z_p)$ is given by

$$z_r = 1 + h + \frac{R_p}{R_a}(1 - \sin\theta) + Z_p/R_a, \tag{C.14}$$

where

$$\theta = \cos^{-1}\left(\frac{Y_r - Y_p}{R_p}\right). \tag{C.15}$$

The instantaneous position of the rotlet is determined by applying the approach in the boundary element method [101], where a force free system with finite walls is treated as composed of a system of infinitesimal elements that respond to the applied external flow field. Interrogating the flow field where the surface of the sphere would be, and integrating the velocity of the sphere surface in time, determines the instantaneous position of the sphere. The instantaneous position is given by:

$$\mathbf{x}_r(t) = \int_0^t \int_0^{2\pi} \mathbf{u}(0, \sin\theta, z_r + \cos\theta; t')d\theta dt' \tag{C.16}$$

where $\mathbf{u} = (0, u_2, u_3)$ is found from equations C.8-C.9, assuming zero initial conditions.

The location of the passive sphere is then determined by treating it as a tracer particle moving under the influence of the rotlet, so its velocity is

given by

$$\mathbf{u}_p = \frac{\Omega}{r_p^3}(0, -r_{p,3}, r_{p,2}), \tag{C.17}$$

where $\mathbf{r}_p$ is the vector distance between passive and active sphere centres, and Ω is given by equation C.4. The updated position of the passive tracer (Y_p, Z_p) is determined by integrating equation C.17 in time, the rotlet position is recomputed and the process is iterated until convergence.

This iterative process was repeated for various separation distances, h, and experimental combinations of active and passive sphere radii, R_a and R_p respectively, and applied rotation angle θ_∞. The prediction of the model are compared with the experimental results for two-sphere interactions in Figure C.6 and Figure C.7. A legend denoting the data markers used in the Figures is given in Table C.1.

The translational motion of the passive sphere measured as a function of separation distance is shown in Figure C.6. The translational motion is scaled by the characteristic amplitude of the torsional oscillation of the active sphere in Figure C.6a. The unsteady rotlet model is in good quantitative agreement with the experimental findings. The agreement breaks down at very small separations for which, in the experiments, the disturbance flow generated by the motion of the passive sphere caused the active sphere to perform translational oscillations. Inclusion of lubrication effects in the model is currently underway in an attempt to resolve the discrepancy between theory and experiments at very small separations. Also note that as the amplitude of oscillation increases the linearisation assumption starts to break down at large inter-sphere distances, as can be seen more clearly in the unscaled Figure C.6b. A possible explanation for these discrepancies observed at large

(a)   (b)
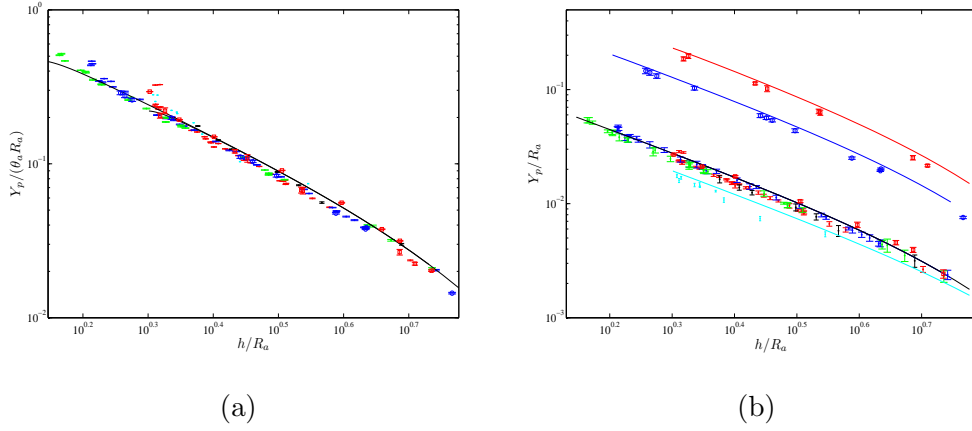
Figure C.6: Active-passive pair: Translational motion of the passive sphere as a function of separation distance. (a) Scaled by the characteristic amplitude of the torsional oscillation of the active sphere $R_a\theta_\infty$ (symbols indicate experiments). The curves are the predictions of the oscillatory rotlet model. Note the outliers at larger distance correspond to large amplitude cases as may be seen more clearly from the unscaled data in (b).

distances is that the amplitude of the oscillation approaches that which forms the condition for validity of the quasi-steady assumption, $\theta_0 < 57°$.

Another feature of the two-sphere interaction captured by the unsteady rotlet model is the suppression of torsional oscillation of the active sphere which occurs as it approaches the passive sphere, as shown in Figure C.7a. Furthermore, the linear dependence on distance of the phase difference between the torsional oscillations of the rotlet and the translational oscillations of the passive sphere agrees with the experimental finding, as shown in Figure C.7b. This suggests that the phase difference reported in §5.3 may not be solely an inertial effect. Instead it results from the unsteady behaviour of the active sphere which generates a wave in the fluid.

(a)   (b)
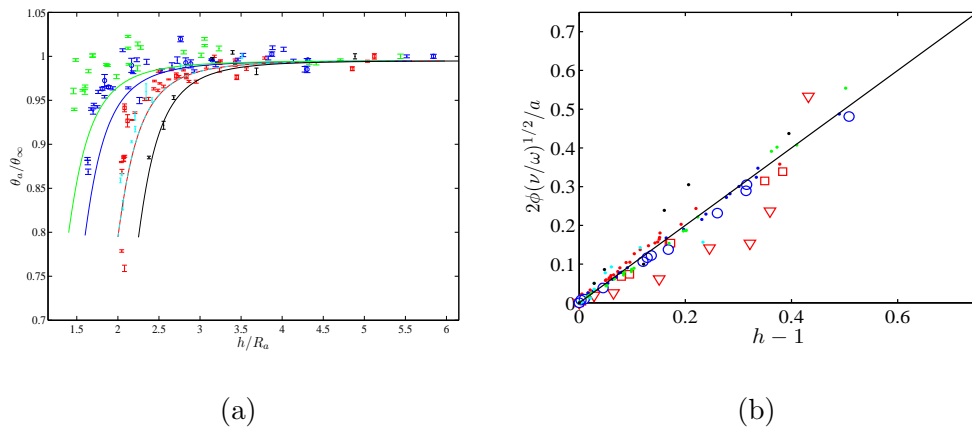
Figure C.7: Active-passive pair: (a) Suppression of rotational oscillations of the rotlet given by θ_a/θ_∞ for varying h and the various combination of parameters as indicated in the legend, are compared with the theoretical model (solid curves). (b) The experimentally measured phase difference, ϕ, scaled by δ/a, for various 2-sphere experiments collapse onto the predicted curve (solid, black line).

a_A (mm)	a_P (mm)	θ_A (degrees)	marker
7.93	7.93	~ 6	·
7.93	4.77	~ 6	·
7.93	3.17	~ 6	·
6.35	6.35	~ 5	·
7.93	4.77	~ 30	○
7.93	7.93	~ 54	□
6.35	7.93	~ 6	·
7.93	7.93	~ 6	▽

Table C.1: Details of the particle-pair combinations studied in and the corresponding data markers used in Figure C.6 and Figure C.7. Note that the data markers denoted by '▽' correspond to the experiments performed in fluid of viscosity $1.4 \mathrm{x} 10^4$ mm^{2}s^{-1}.

Appendix D

Publications

This appendix contains two publications to which the author contributed during the course of his PhD. The publications concern a global pattern switch which occurs in cellular materials under compression. First demonstrated in a elastomeric structure, the reversible pattern switch results from a buckling instability and transforms a square array of circular holes into a set of orthogonal ellipses [104]. For the first publication, which demonstrates the robustness of the pattern switch in a variety of soft cellular solids, the author fabricated the visco-elastic sample, performed experiments on the sample and contributed to the writing of the manuscript. The second publication demonstrates that the pattern switch can occur in plastic structures provided the compression is performed above a critical strain rate. The buckling instabilities present in elastic and plastic lattices are then compared and contrasted. For this publication, the author conducted all the experimental work and analysis, and contributed significantly to the writing of the manuscript.

OPINION

Pattern switching in soft cellular solids under compression

Cite this: *Soft Matter*, 2013, **9**, 4951

T. Mullin,* S. Willshaw and F. Box

It is becoming increasingly recognized that nonlinear phenomena give an opportunity to provide robust control of the properties of soft metamaterials. A class of elastic instabilities are discussed which arise when a soft cellular material is compressed. The global nature of the induced pattern switch makes it a prime candidate for controlling macroscopic photonic and auxetic properties of the material. We demonstrate the robustness of the phenomena using a range of soft materials and show how the shape of the repeat unit of the periodic pattern can be used to influence the global characteristics of the soft solid.

1 Introduction

Low density cellular solids are common in nature with examples ranging in scale from cancellous bone with high strength-to-weight ratio[1] to the intricate structures on the wings of butterflies which give them their iridescent colours.[2] Man has exploited these features in the design of complex structures ranging from spacecraft to photonic crystals.[3] When they are soft, cellular solids can be compressed using small strain fields and exhibit structural instabilities above a critical value of the applied strain.[1] The influence of instabilities on global material properties are important[4] in broadening the functionality of materials in terms of their wetting and photonic properties. A specific example of this is provided by a novel instability uncovered when a two-dimensional elastomer with a square lattice of holes is compressed.[5] The pattern switch which is involved is robust and has now been found at the nanoscale[6] and applied to the control of photonic devices.[3]

The purpose of this article is to report on a number of observations at the macroscale which demonstrate that the pattern switch is a robust geometrical effect which is independent of the details of the material properties of the matrix. The central idea being advanced here is that it is the symmetry of the geometry of the cellular structure which is key to the pattern switch. Specifically, the strong coupling of the square geometry forces a simple bifurcation so that details of the material properties of the matrix are of secondary importance. The geometrical theme is explored using a range of soft materials and the review is concluded by reporting on the influence of hole shape on the pattern switch.

Manchester Centre for Nonlinear Dynamics, The University of Manchester, Oxford Rd, Manchester M13 9PL, UK. E-mail: tom@reynolds.ph.man.ac.uk; Fax: +44 (0)161 275 4056; Tel: +44 (0)161 275 4070

2 Pattern switching in soft cellular solids

The original experiments[5] were performed using elastic specimens with circular holes which were accurately cut out of an elastomer sheet using water jets. The sample comprised a microstructure of a 10×10 square array of circular holes of 8.67 mm diameter with 9.97 mm center-to-center spacing, vertically and horizontally. The periodic lattice microstructures were cut from 9.4 mm thick sheets of the photoelastic elastomer PSM-4 using water jets and the samples were approximately 100 mm by
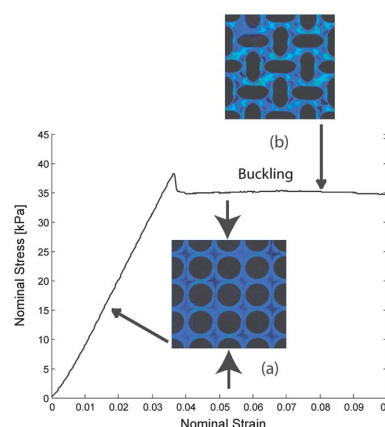
Fig. 1 Experimental results in the form of nominal stress *versus* nominal strain curves for a 10×10 square array of holes in a sheet of PSM-4 elastomer under compression. The dependence is approximately Hookean at small strains and all holes deform slightly as indicated in image (a) (here strain is applied uniaxially and is defined as $\varepsilon = \Delta h/h$ where h is the original height of the sample and Δh is the displacement). The departure from linearity is the result of an elastic buckling instability in the microstructure that triggers a pattern transformation to an array of orthogonal ellipses (b). The material is photoelastic and concentrated regions of stress are indicated by the light colouring.

100 mm. The material has a shear modulus of 3.25 MPa and is photoelastic so that the colour variation seen in Fig. 1(b) gives an indication of the stress field. The sample was held vertically between two close fitting 5 mm thick polymethylmethacrylate (PMMA) sheets to minimise out-of-plane buckling. An Instron compression testing machine was used to apply a quasi-static uniform displacement to the sample and record its response.

The results shown in Fig. 1 provide a typical example of a stress–strain response for cellular materials[1] where stress is approximately proportional to strain for small displacements and compression within the material is taken up by fore-shortening of interstitial vertical ligaments in the structure. Above a critical values of the strain (here ∼4%), buckling of the ligaments occurs and stress becomes approximately independent of strain. The buckling is coincident with the onset of the pattern switched state shown in Fig. 1(b). The new state appears rapidly and the transition is reversible and repeatable. Its global nature is a result of the coupling of the buckling throughout the square lattice and involves the counter-rotation of neighboring interstitial four pointed star-shaped ligatures between the holes and is predicted from theory.[7]

The patterned switched state exhibits a negative value of the Poisson's ratio[8,9] which is sometimes called 'Auxetic' behaviour. This is illustrated in the image shown in Fig. 2 where a square lattice of circular holes in a nominally two-dimensional silicone rubber elastomer has been compressed with a nominal strain of $\varepsilon = 0.25$. A clear indication of negative Poisson's ratio is that the lateral boundaries of the sample bend inwards under compression whereas a solid rubber sample will bulge. Indeed the results of a detailed numerical and experimental investigation are in good accord for this auxetic property.[9] A limitation is that the auxetic response only occurs under compression but it is robust, it is created in a controlled way by a simple modification to the material and it will work at the nanoscale.

A moulding process was also used to create samples containing 10×10 circular holes of diameter ∼10 mm in a set jelly. This material has Young's modulus of ∼10^3 Pa (ref. 10) and deforms in plane under its own weight when held between two chalk dusted PDMS sheets as shown in Fig. 3. As can be seen, a pattern switched state where the original square array of
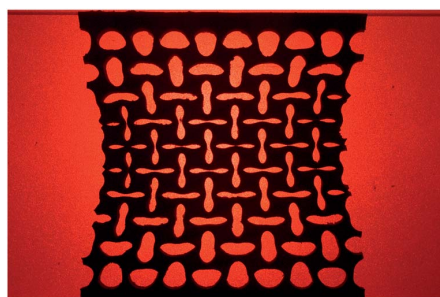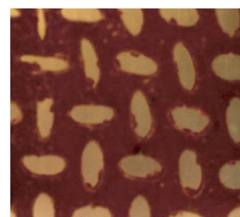

Fig. 3 Pattern switched state in a jelly which has deformed under its own weight. The initial state was a square lattice of circular holes which switched rapidly to the shown array of orthogonal ellipses when the sample was turned from lying horizontal to standing vertical.

circular holes was transformed into an array of orthogonal ellipses. The switch occurred as soon as the sample was oriented vertically.

Specific anisotropy was introduced into the jelly in a controlled yet simple manner. This is illustrated in the images shown in Fig. 4 where 8 mm long by 1 mm diameter aluminum rods were placed as shown in Fig. 4(a). They were positioned during the setting phase of the jelly. As in the case of the pure jelly, the material again deformed under its own weight but now two qualitatively different buckling modes are evident in Fig. 4(b and c). The pattern switch is clear in Fig. 4(b) where the rods are initially aligned in the direction of gravity ('g'). On the other hand, when the sample was rotated through ninety degrees so that the rods were in a direction orthogonal to 'g', the pattern switch was not found and instead shear bands formed under compression as in the example shown in Fig. 4(c). In this
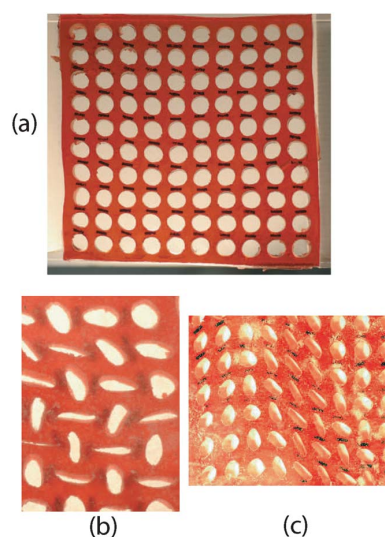
Fig. 4 Jelly samples where additional anisotropy has been introduced into the sample using a set of 8 mm long, 1 mm diameter aluminium (Young's modulus ∼ 70 GPa) rods which were placed above each hole during the moulding process. The initial undeformed state where the sample was laid flat and unstrained is shown in (a). (b) A patterned switched state which was formed when the sample was oriented with gravity ('g') parallel with the rods. (c) A shear band forms when the sample is oriented such that 'g' lies in a direction orthogonal to the rods.

Fig. 2 Two dimensional silicone rubber sample under vertical compression at $\varepsilon = 0.25$. The sample was held between two loose fitting PDMS plates which prevented out of plane buckling. The sidewalls of the initial rectangular sample moved inwards under compression indicating negative Poisson ratio behaviour.

case buckling was confined within the layers of rods and was not a global effect but remained localised.

A combination of two materials was used to manufacture the soft cellular solid shown in Fig. 5. It comprised a 10 × 10 square array of holes in a silicone rubber sheet where the holes were filled with jelly. Filling the holes with a more rigid material than the matrix does not lead to any significant results.[7] However, when a far weaker material was placed in the holes, a pattern switch was observed above a critical strain of $\varepsilon \sim 0.04$ *i.e.* very close to the value found for the case of air holes discussed above. Hence inclusion of a material which has a Young's modulus of ≤1% of the bulk does not suppress the pattern switch and has an insignificant effect on the critical strain.

A sample which contained a 5 × 5 array of circular holes was manufactured using a visco-elastic fluid which is sold as Dittman's therapeutic putty. The material is essentially a stiff variant of the viscoelastic material 'silly putty'. It has a very high viscosity of $\sim 10^5$ Pa s and hence flows slowly over periods of hours. On the other hand it is an elastic solid if strained on short timescales. The sample was produced by refrigerating for ~3 hours which aided removal from the mould. The material has a shear modulus of ~260 kPa and hence buckled under compression. It was positioned horizontally on the lubricated surface of a compression rig and strained uniaxially at a rate of 1 s^{-1} for 5 mm. It was found that the sample was sufficiently rigid to maintain it's original structure for ~1 hour if unstrained and pattern switched above a critical strain as shown in Fig. 6.

The results obtained for the square array of circular holes suggests that other periodic elastomeric structures with appropriate symmetry will have similar properties. This is highlighted using the uniaxial compression of a rectangular array of elliptical holes and the results are shown in Fig. 7. In this case compression was applied in a direction perpendicular to the major axis of the constituent elliptical holes. The nominal stress–strain behaviour is shown in Fig. 7. As for circular holes, the relationship is initially linear with homogeneous compression up to a strain of 0.03. At this strain there is a pattern transformation and the stress plateaus. The transformation is a result of a local elastic buckling instability of the vertical ligaments with rotation of interstitial ligatures in opposite directions. The collective behaviour results in a reversible and repeatable pattern transformation to an alternating array of high and low aspect ratio ellipses where the aspect ratio
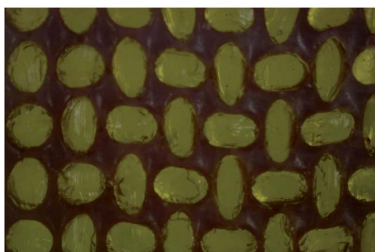

Fig. 6 Pattern switch in the deformation of a visco-elastic fluid. This image (of the central region of the sample) was taken ~1 minute after the sample containing a 5 × 5 square array of circular holes which had been laid on a lubricated flat bed and compressed.
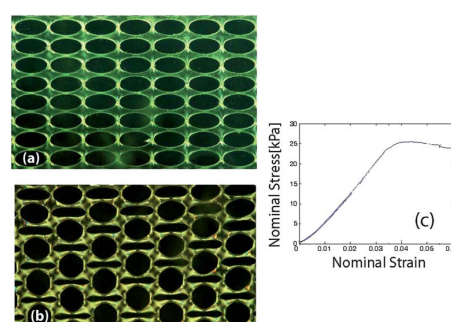

Fig. 7 Uniaxial compression of a rectangular array of ellipses. The sample was 133.2 × 102.5 mm by 6.9 mm thick, containing a 12 × 17 rectangular array of elliptical holes of size 5.01 mm (major axis) by 2.67 mm (minor axis) with hole spacing of 5.99 mm vertically and 11.02 mm horizontally. The direction of compression was orthogonal to the minor axes of the ellipses. Compression in the orthogonal direction results in the same pattern at a value of ε which is ~0.5 smaller than required for the transformation shown here *i.e.* approximately the same as the axis ratio of the ellipses. An experimental stress–strain plot is shown in (c).

contrast increases with increasing macroscopic strain and the low aspect ratio ellipses become nearly circular. The final pattern which emerges is independent of the direction of the applied strain and the ratio of the critical strain required for the pattern transformation is approximately proportional to that of the major to minor axes indicating that it is the stiffness ratio of the repeat unit which sets this global property.

The effect of cell shape was also investigated using 2D cellular structures with square and diamond-shaped voids shown in Fig. 8(a) and (b). The 4 × 4 square array with 10 mm sided voids with a void fraction of ~0.45 were moulded in silicone rubber. The buckled states display qualitatively different features as shown in Fig. 2 although it can be seen that the stress–strain plots are qualitatively similar to each other. The diamond shaped lattice is clearly weaker than the square one as it buckles at ~0.75 of the applied strain and supports ~2.5× smaller stress than the square one. The pattern which develops when the diamond geometry sample was compressed above the critical strain is shown in Fig. 8(d) and a pattern switch was found which is qualitatively similar to the elliptical patterns observed with circular holes. Instead of ellipses, the diamond shaped voids form rhombi which are oriented orthogonally to
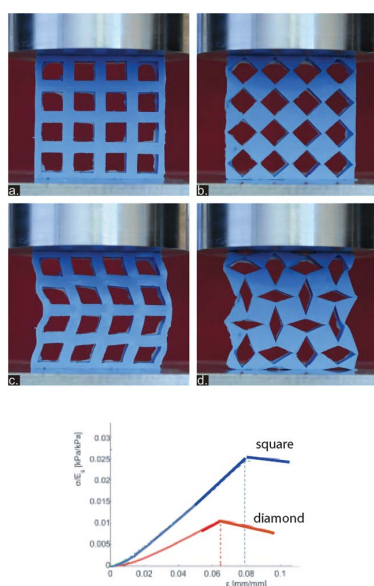

Fig. 5 Silicone rubber sample with jelly filling each of the holes. *N.B.* The jelly adhered to the rubber and retained contact with it throughout the pattern switch.

Fig. 8 Images of the compression of an array of square (a and b) and diamond (c and d) holes in a silicone rubber matrix. Both have the voidage fraction of 0.45 and the images were taken at $\varepsilon = 0.03$ (a and b) and $\varepsilon = 0.1$ (c and d). Experimental stress–strain plots for the respective cases are shown below the images.

their neighbours. This example can be considered as a practical realization of the model problem of rotating tessellated squares which has a Poisson's ratio of -1.[11,12] Hence the material shrinks laterally by the same amount it is compressed by. The second example shown in Fig. 8(a) and (c) is a lattice of squares which does not show a pattern switch but simply buckles so that there is localized shearing of the voids. This is perhaps a surprising result since a simple strut model of a square lattice does show coupled buckling[13] as discussed below.

3   An elemental mechanism

The mechanism which gives rise to the pattern switch can be understood using a simplified model shown in Fig. 9. In this the rubber matrix has been replaced by a skeleton of elastic
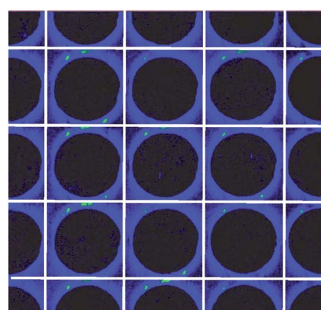

Fig. 9 A schematic diagram illustrating how a skeletal arrangements of Euler struts (shown in white) can be used to represent the full elastomer sample.

classical Euler struts[14] shown in white. The pattern switch which results from the compression of the array is shown in Fig. 10. The initial square array in Fig. 10(a) loses stability above a critical load to a pair of buckled states shown in Fig. 10(b) and (c) when it is compressed uniaxially. In the buckled states it can be seen that elastic 'waves' have travelled across the array from top to bottom and side-to-side and that each of the interstitial points has rotated in alternate directions.

A measure of this bifurcation event was made in experiments on 10×10 arrays of holes in an elastomer. The measure of the bifurcation is the ratio of the vertical to horizontal dimension of the holes which were averaged over the central 36 holes of the 10×10 array. A fixed set of reference holes was used in each case and averaging was performed in pairs. A pitchfork bifurcation is uncovered where a circular array of holes (ratio = 1) is replaced by an array of orthogonal ellipses with increasing (or decreasing) ratios. A simple model for the buckling of a single Euler strut is given by[15]

$$\dot{x} = \lambda x - x^3 \qquad (1)$$

where λ is the load parameter and x is the deflection of the middle of the beam. $x = 0$ is a solution of the equation for all λ but it can easily be shown that there are two more real stable solutions $x = \pm\sqrt{\lambda}$ for $\lambda > 0$ together with the unstable trivial $x = 0$ state. In the case of the pattern switch the array of coupled
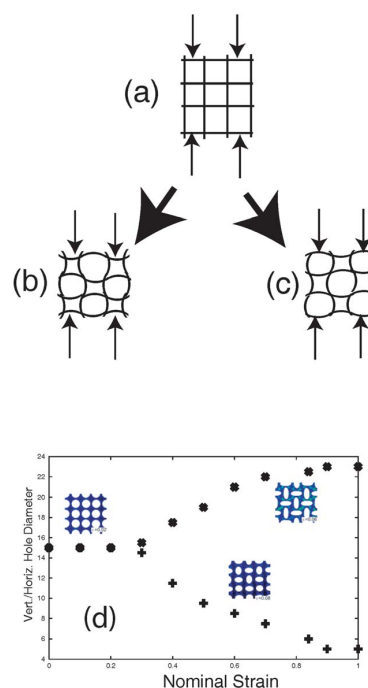
Fig. 10 The compression of the skeletal sample (a) results in buckling of the Euler struts above a critical load to produce two buckled states (b) or (c).[13] An experimental bifurcation diagram is given in (d) where the measure of the state is the ratio of the vertical to horizontal dimension of the holes averaged over the central 36 holes of 10×10 array of circular holes. The hole dimension ratios were measured w.r.t. the same preselected hole.

Euler struts gives a single global pitchfork bifurcation because of the strong coupling which is present in the square array. An interesting feature which is evident in the experimental bifurcation diagram is that the bifurcation is sharp despite the inevitable presence of imperfections. This is perhaps an indication that the imperfections are in some sense 'averaged out' in the square array.

4   Discussion

In conclusion, we have shown that pattern switching is a robust phenomenon when a soft cellular solid containing a square array of circular holes is compressed. The effect does not depend on the details of the properties of the elastic matrix. The robustness is striking and perhaps surprising since only approximately square geometries can be made in practice. Hence the presence of manufacturing imperfections are relatively unimportant. Of greater importance than either the material properties or the presence of imperfections is the symmetry of the lattice and its repeat unit. While square lattices may be weak structures from an engineering perspective, they have important optical properties at the nanoscale and the nonlinear features discussed here persist to very small scales.[4] Hence, these observations at the macroscale open the door for exploring novel metamaterials at a convenient laboratory scale and they in turn provide insights into mechanisms which control properties at the nanoscale.

Acknowledgements

References

1 L. J. Gibson and M. F. Ashby, *Cellular Solids, Structure and Properties*, Cambridge University Press, 1997.

2 P. Vukusic and J. R. Sambles, *Nature*, 2003, **424**, 852–855.

3 X. Zhu, G. Wu, R. Dong, C. Chen and S. Yang, *Soft Matter*, 2012, **5**, 2412–2418.

4 S. Singamaneni and V. V. Tsukruk, *Soft Matter*, 2010, **6**, 5681–5692.

5 T. Mullin, S. Deschanel, K. Bertoldi and M. C. Boyce, *Phys. Rev. Lett.*, 2007, **99**, 084301.

6 Y. Zhang, E. A. Matsumoto, A. Peter, P.-C. Lin, R. D. Kamien and S. Yang, *Nano Lett.*, 2008, **8**, 1192–1196.

7 J. Michel, O. Lopez-Pamiesb, P. Ponte Castan and N. Triantafyllidis, *J. Mech. Phys. Solids*, 2007, **55**, 900–938.

8 R. Lakes, *Science*, 1978, **235**, 1038–1040.

9 K. Bertoldi, P. M. Reis, S. Willshaw and T. Mullin, *Adv. Mater.*, 2010, **22**, 361–366.

10 A. Greenhill, *Proc. Cambridge Philos. Soc.*, 1881, **4**, 65.

11 D. Attard and J. Grima, *Phys. Status Solidi B*, 2008, **245**, 2395–2404.

12 J. Grima, A. Alderson and K. E. Evans, *Phys. Status Solidi B*, 2005, **242**, 561–575.

13 N. Ohno, D. Okumura and T. Niikawa, *Int. J. Mech. Sci.*, 2004, **46**, 1697–1713.

14 A. Love, *Treatise on the Mathematical Theory of Elasticity*, Dover, 1944.

15 S. Strogatz, *Nonlinear Dynamics and Chaos: With Applications to Physics, Biology, Chemistry, and Engineering (Studies in Nonlinearity)*, Perseus, 1994.

197

Dynamic compression of elastic and plastic cellular solids

F. Box,[1] R. Bowman,[2] and T. Mullin[1,a]

[1]*Manchester Centre for Nonlinear Dynamics, University of Manchester, Oxford Road, Manchester M13 9PL, United Kingdom*
[2]*Cavendish Laboratory, University of Cambridge, Cambridge, United Kingdom*

We report the results of an experimental investigation into buckling in elastic and plastic cellular materials under dynamic compression. The buckling instabilities are in the form of a global pattern switch where the square array of circular holes is transformed into a set of orthogonal ellipses. Properties of the instabilities in the elastic and plastic cellular materials are compared and contrasted. The case of the elastic structure is considered as a delayed pitchfork bifurcation. On the other hand, the response of the plastic lattice is complex, and an irreversible global instability is only found above a critical compression rate. © *2013 AIP Publishing LLC*. [http://dx.doi.org/10.1063/1.4824845]

Low density cellular solids are common in nature with examples at the macroscale of cancellous bone[1] with high strength-to-weight ratio to the intricate micro-structures on the wings of butterflies which give them their iridescent colours.[2] The strength-to-weight ratio and optical properties of such materials have been exploited in the design of complex technologically important structures ranging in scale from spacecraft to photonic crystals. When these materials are compressed they may undergo elastic instabilities where the cell walls of the matrix bend or buckle. The influence of this on the global properties of the material is a current area of research. Applications include energy absorption by the crushing of layers[3] to the control of bandgaps of photonic crystals[4] and the wetting of surfaces.[5]

An interesting example of an elastic instability in a cellular material is provided by the compression of a two-dimensional elastomer with a square lattice of holes. The phenomenon is the main focus of this paper and is illustrated in Fig. 1 where it can be seen that the initially square array of circular holes is transformed into a set of orthogonal ellipses under 8% vertical compression. Note that the sides of the sample shown in Fig. 1 move inwards under compression which is a feature of the negative Poisson ratio of this cellular material.[6,7] This instability was predicted theoretically[3] and realised experimentally[8] and has been shown to exist in a variety of soft materials under compression.[9] The aim of this study was to investigate the effects of dynamic compression on the buckling instabilities present in elastic and plastic cellular lattices. In elastic lattices, the switch in states is reversible, repeatable, and global and has now been found at the nanoscale.[4,10] Euler buckling is central to the instability and is of current interest in other aspects of nanomaterials.[11] Since the pattern switch is reversible in the elastic lattice, one sample was used for all compressive testing conducted throughout this investigation. The global pattern switch also occurred in plastic samples; however, different samples had to be used for each experiment as the plastic deformation process was irreversible. The occurrence of the pattern switch in plastic materials suggests that similar

buckling instabilities may result from the dynamic compression of other hard materials.

The buckling of an elastic cellular material with a square array of circular holes can be considered as an example of a pitchfork bifurcation[9] where in the case of the pattern switch the two branches of the pitchfork are buckled states which are shifted in phase by half a wavelength. When a parameter is swept through such a bifurcation there is a delay in the onset of the instability[12] and the amount of the delay will scale as the square root of the sweep speed[13] over a small range of the parameters.

The elastomer sample was made from the addition curing silicone rubber Sil AD Spezial (SADS), supplied by Feguramed GmbH. The cured material has the manufacturer's quoted value of the Young's modulus of $E_s \simeq 400 \, \text{kPa}$ which is in accord with measured values.[14] The manufacture of the sample involved mixing equal measures of two fluids, placing the individual component fluids under vacuum to remove dissolved gases and allowing the mixture to set for an hour to ensure full curing. The mixture was poured into a purpose-built mould of machined cylindrical pillars arranged on a square lattice. The cured sample was removed from the mould, and the two side walls were cut from the sample, leaving seven columns of eight holes, flanked by a column of eight semi-circles on either side. The elastomer sample comprised a lattice of circular holes of diameter $8.79 \pm 0.09 \, \text{mm}$ arranged on a square. The void fraction was 0.65. The height of the sample was $77 \pm 0.1 \, \text{mm}$, width $77 \pm 0.1 \, \text{mm}$, and thickness $7 \pm 0.1 \, \text{mm}$.

The plastic samples were fabricated using a commercial 3D printer (3D Touch triple head, Bits From Bytes) using acrylonitrile butadiene styrene (ABS) plastic. This is a lightweight rigid polymeric material with a Young's modulus of 2.3 GPa which is a factor of ~ 5750 stiffer than the silicone rubber. The printer forms plastic objects by a process known as fused filament fabrication; in essence, a bead of molten thermoplastic is extruded from a hot nozzle which is moved under computer control in the horizontal direction with defined steps in the vertical to build up the object, layer by layer. It is based on the open-source RepRap project.[15] A base layer of polylactic acid was used to help prevent the printed object sticking to the print bed. Since the sample is
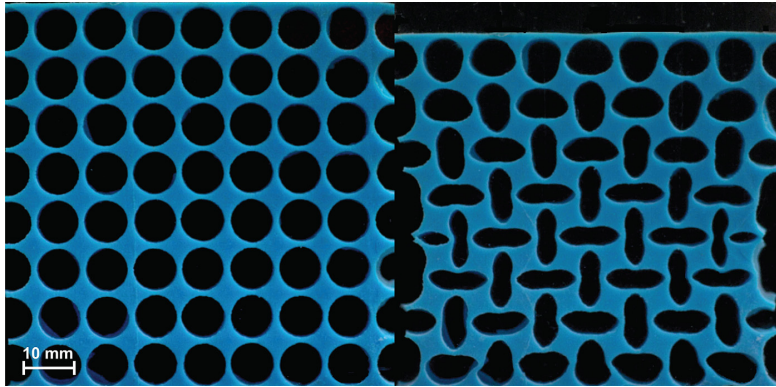
a)tom@reynolds.ph.man.ac.uk

FIG. 1. The pattern switch in a two-dimensional elastomer. (a) Initial state (b) at 8% compression. The global nature of the transformation is evident apart from edge effects at the top and bottom surfaces.

built up in horizontal layers, the material properties are anisotropic; specifically, the joins between layers are weaker than the layers themselves. However, as we are primarily interested in 2D distortions of the structures, printing the samples with the plane of interest horizontal ensured that the material properties were homogeneous in the plane of interest for our experiment.

The plastic samples comprised 5×5 lattices of 9 ± 0.02 mm diameter holes arranged on a square array. The samples had a void fraction of 0.64. They were 60 ± 0.02 mm high, 60 ± 0.02 mm wide, and 10 ± 0.02 mm thick. The side, top, and bottom boundaries were all flanked by semi-circles, i.e., the samples consisted of 5×5 lattices bounded by semi-circles as shown in Fig. 4. The testing of the plastic samples was irreversible, and a new sample was used in each experiment.

The samples were tested on two Instron machines, a twin arm model 5569 for the plastic and single arm model 3345 for the rubber. Each of the samples was placed in a housing and compressed with a Perspex loader of width 100.10 ± 0.05 mm, thickness 9.68 ± 0.09 mm attached to an aluminium clamp. The housing ensured the samples remained upright and consisted of an aluminium U-shaped frame and base, which was attached to each Instron, and a

front and back plate both made from Perspex with a spacing of 10.1 ± 0.1 mm. The front and back plates enabled visualization, prevented out-of-plane buckling and were removable to allow access to the experimental sample. There was a clearance of 0.7 ± 0.1 mm between the loader and the housing when the setup was assembled.

Compression tests were performed on both machines using 1 kN load cells. The sample faces were dusted with flour for the elastomeric structure and coated with vaseline for the plastic lattices to reduce frictional effects. All surfaces were made parallel to ensure even loading of the sample and prevent the loader touching the outer plates of the housing. The load associated with the displacement was recorded once every 100 ms and used to produce a stress-strain curve for the compression process.

The stress-strain data for the elastic lattice shown in Fig. 2(a) has the same characteristic form for all strain rates. The elastic regime where stress increases in proportion to applied strain is followed by a stress plateau where stress is independent of strain. Buckling of the ligaments of the cellular structure is initiated at the turnover point and grows as the square root of the strain in accord with the generic behaviour of pitchfork bifurcations.[9] These curves contain the generic features found in cellular materials under compression of a
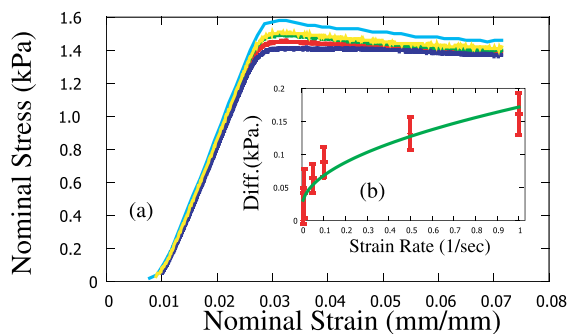

FIG. 2. (a) Plot of the stress-strain diagram for an 8×7 elastic lattice for linear compression rates at 0.005, 0.001, 0.05, 0.1, 0.5, and 1 mm s^{-1}. The stress plateau increases monotonically with strain rate. (b) Differences between the quasistatic critical point and the stresses at onset of the instability at the strain-rates used in (a). The solid line is the least squares fit of a square root function to the data. The quasistatic value was measured at a strain rate of 0.0001 mm s^{-1} which has been shown previously[8] to give a good approximation to the quasistatic limit.
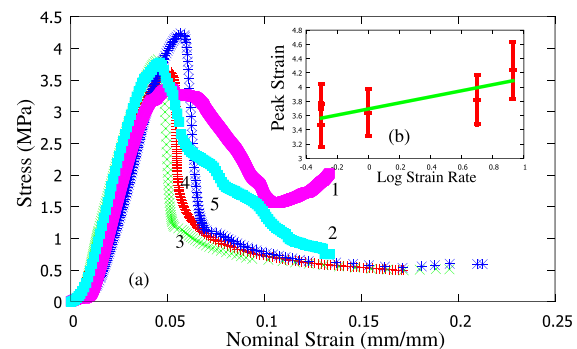
FIG. 3. (a) Stress strain datasets for the ABS plastic material which were taken at 1: 0.016 mm s^{-1}, 2: 0.05 mm s^{-1} (no stress plateau), 3: 1.0 mm s^{-1}, 4: 5.0 mm s^{-1}, and 5: 8.5 mm s^{-1} (single stress plateau). (b) Inset of peak stress for cases where the pattern transformation occurred plotted as a function of the log of the strain rate. The fitted line in (b) has a slope of 0.427. N.B. The stress strain datasets taken at 0.5 mm s^{-1} have been omitted from (a) to clarify the diagram.

FIG. 4. Images of the compression of a plastic sample. (a) Initial state (b) after compression by 10% at $1.0\,\mathrm{mm\,s^{-1}}$. In this case the Poisson's ratio was found to be $\simeq 0$. Small ($\sim 0.8\,\mathrm{mm}$ diam.) holes can be seen at the center of each interstitial. These are features of the prototyping process, and their location was set to the centers of the interstitials to minimize their effect on the strength of the material.

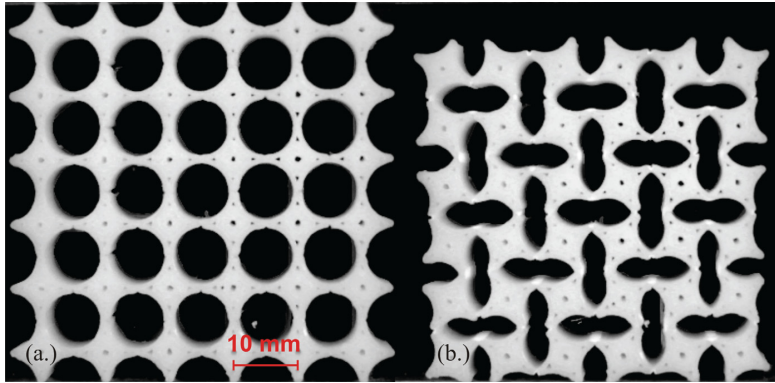linearly elastic region followed by a stress plateau above a critical strain.[1] In the case of a square lattice of holes, a pattern switch from an array of circular holes to one of orthogonal ellipses as shown in Fig. 1 occurs at the onset of the stress plateau.

The linear relationship between macroscopic stress and strain results from the collective microscopic elastic bending of individual ligaments. As can be seen in Fig. 2(a) there is very weak dependence of the slope on strain rate over the range investigated. This result is in accord with those reported in Ref. 16 where independence of this slope was found over a much wider range of strain rates than investigated here. The elastic lattice has the characteristics of a type I material[17] such that there is a gradual onset of the instability with increasing load which is typical of columnar buckling. Hence the plateau corresponds to buckling of the cell walls which occurs above a critical strain.

We show in the inset to Fig. 2(b) a plot of the difference between the values of the critical stress at the onset of the pattern switch, i.e., the values of the stress at the turning points in Fig. 2(a), and the quasi-static case for the strain rate range $0.005\,\mathrm{mm\,s^{-1}}$ to $1\,\mathrm{mm\,s^{-1}}$. The solid line is the least squares fit of a square root function to the data. This result is consistent with the generic delay in pitchfork bifurcations found when the control parameter is swept through the bifurcation point at increasing speeds.[13]

The stress-strain results shown in Fig. 3(a) were obtained using the plastic material. Dynamic compression above a strain rate of $0.5\,\mathrm{mm\,s^{-1}}$ results in a pattern switch comparable to that of the elastomeric structure. An example of a plastic lattice before and after compression at a strain rate of $1\,\mathrm{mm\,s^{-1}}$ is shown in Fig. 4 and corresponds to stress-strain dataset labelled 3 in Fig. 3. Compression at a strain rate below $0.5\,\mathrm{mm\,s^{-1}}$ results in localized collapse of the plastic structure and the formation of a shear band (see Fig. 5). Although distinct dynamic regimes exist above and below a strain rate of $0.5\,\mathrm{mm\,s^{-1}}$, the threshold exhibits sensitivity to imperfections; one sample compressed at $0.5\,\mathrm{mm\,s^{-1}}$ pattern switched whereas a second sample compressed at the same rate displayed localized buckling. The sensitivity to imperfections means that it is difficult to give a sharp estimate of the critical strain rate. Intriguingly, previous work on the compression of elastic lattices showed that the

effect of imperfections on the quasistatic onset of the pattern switch to be surprisingly small.[14]

Above the critical strain rate, the global pattern switch is a robust phenomenon which results from a highly nonlinear event. The pattern switch is caused by plastic collapse and is hence irreversible. The stress-strain data obtained from samples compressed with a strain rate above $0.5\,\mathrm{mm\,s^{-1}}$ (see lines labelled 3–5 in Fig. 3) have the characteristics of a type II material with a linear elastic region and a pronounced peak at a catastrophic buckling transition,[17] followed by a subsequent stress plateau. The peak stress increases with strain rate as shown in Fig. 3(b) where the straight line fit to the logarithmic data indicates that the scaling is ≈ 0.427, i.e., significantly faster than the values of 0.25 found for the elastomer, i.e., the plastic switch is not an example of a simple pitchfork bifurcation. The stress plateau appears to be independent of strain rate, as the level attained by different samples compressed at different rates is the same to within experimental error, which suggests that the pattern switching process is a robust feature of the dynamic compression of plastic lattices and that the energy absorbed by the material is independent of strain rate.[1]

The location of the shear band which forms for compressive strain rates below $0.5\,\mathrm{mm\,s^{-1}}$ is dependent on local imperfections in the sample. The stress-strain results obtained
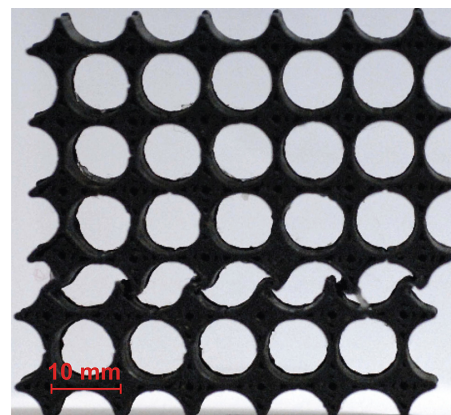

FIG. 5. An image of a localized shearband formed in an ABS sample at a compression rate of $0.0033\,\mathrm{mm\,s^{-1}}$. The location of the band is dependant on local imperfections in the sample.

for strain rates less than $0.5\,\mathrm{mm\,s^{-1}}$ have complicated forms and lack the stress plateau indicative of a pattern switch; two datasets, obtained at strain rates of $0.016\,\mathrm{mm\,s^{-1}}$ and $0.05\,\mathrm{mm\,s^{-1}}$, are included in Fig. 3.

In conclusion, a global pattern switch occurs for all strain rates in an elastic cellular solid which contains a square array of circular holes. The linear section of the stress-strain relationship does not depend on strain rate, but the amplitude of the stress plateau formed when the pattern switch that occurs increases in proportion to the square root of the strain rate. This finding is in accord with generic features of dynamic pitchfork bifurcations.[12] Geometrically equivalent cellular structures made from ABS plastic have a global pattern switch above a critical strain rate. An interesting feature which emerges is that the plateau stress is independent of the strain rate indicating that the energy absorbed by the material is also independent of strain rate. This result suggests that other rigid materials may undergo a pattern switch under dynamic loading. Several attempts were made with a copper cellular material and partial success was achieved. However, we were unable to reach large dynamic strains with the available testing machines and encourage others to test this possibility with more appropriate apparatus.

[1] L. J. Gibson and M. F. Ashby, *Cellular Solids, Structure and Properties* (Cambridge University Press, Cambridge, 1997).
[2] P. Vukusic and J. R. Sambles, Nature **424**, 852 (2003).
[3] N. Triantafyllidis, M. D. Nestorovic, and M. W. Schraad, J. App. Mechs. **73**, 505 (2006).
[4] Y. Zhang, E. Matsumoto, A. Peter, P. Lin, R. Kamien, and S. Yang, Nano Lett. **8**, 1192 (2008).
[5] S. Singamaneni and V. V. Tsukruk, Soft Matter **6**, 5681 (2010).
[6] R. Lakes, Science **235**, 1038 (1987).
[7] K. Bertoldi, P. M. Reis, S. Willshaw, and T. Mullin, Adv. Mater. **22**, 361 (2010).
[8] T. Mullin, S. Deschanel, K. Bertoldi, and M. C. Boyce, Phys. Rev. Lett. **99**, 084301 (2007).
[9] T. Mullin, S. Willshaw, and F. Box, Soft Matter **9**, 4951 (2013).
[10] J. Li, J. Shim, A. Deng, A. Overvelde, X. Zhu, K. Bertoldi, and S. Yang, Soft Matter **8**, 10322 (2012).
[11] S. M. Carr and M. N. Wybourne, Appl. Phys. Lett. **82**, 709 (2003).
[12] P. Mandel and T. Erneux, J. Stat. Phys. **48**, 1059 (1987).
[13] R. Kapral and P. Mandel, Phys. Rev. A **32**, 1076 (1985).
[14] S. Willshaw, "On pattern-switching phenomena in complex elastic structures," Ph.D. thesis (University of Manchester, 2012).
[15] R. Jones, P. Haufe, E. Sells, P. Iravani, V. Olliver, C. Palmer, and A. Bowyer, Robotica **29**, 177–191 (2011).
[16] B. Song, W. Chen, D. Song, N. Winfree, and J. Kang, Int. J. Impact Eng. **31**, 509–521 (2005).
[17] C. R. Calladine and R. W. English, Int. J. Mech. Sci. **26**, 689 (1984).

Bibliography

[1] G. G. Stokes. On the effect of the internal friction of fluids on the motion of pendulums. *Trans. Cambridge Philos. Soc.*, 9:8, 1851.

[2] H. von Helmholtz and G. von Piotrowski. Üeber Reibung tropfbarer Flüssigkeiten. *S.B. Akad. Wiss. Wein.*, 40:607–658, 1860.

[3] R. Hollerbach, R. J. Weiner, I. S. Sullivan, R. J. Donnelly, and C. F. Barenghi. The flow around a torsionally oscillating sphere. *Phys. Fluids*, 14:4192, 2002.

[4] R. F. Folse, A. E. Strahan, and J. M. Nail. High-amplitude torsional oscillations of a sphere in a viscous fluid. *Phys. Fluids*, 17:1774, 1974.

[5] R. F. Folse. Observations of secondary flows generated by a torsionally oscillating sphere in linearly stratified fluids. *Phys. Fluids*, 6:537, 1994.

[6] C. B. Benson and A. C. Hollis Hallett. The oscillating sphere at large amplitudes in liquid helium. *Can. J. Phys.*, 34:668–678, 1956.

[7] E. N. Da C. Andrade and Y. S. Chiong. On the determination of viscosity by the oscillation of a vessel enclosing a fluid: Part I. *Proc. Phys. Soc.*, 48:247, 1936.

[8] J. Buchanan. The oscillations of a spheroid in a viscous liquid. *Proc. Lond. Math. Soc.*, 22:181–214, 1891.

[9] J. Kestin and L. N. Persen. Small oscillations of bodies of revolution in a viscous fluid. *Brown University Report AF-891/2, Contract A718(600)-891*, 1954.

[10] J. E. Verschaffelt. Rotational oscillations of a sphere in a viscous liquid. *Proc. Acad. Sci. Amsterdam*, 18:840–859, 1916.

[11] R. P. Kanwal. Rotary and longitudinal oscillations of axi-symmetric bodies in a viscous fluid. *Q. J. Mech. Appl. Math.*, 8(2):146, 1955.

[12] Lamb, H. *Hydrodynamics*. Dover, 6th edition, 1932.

[13] R. P. Kanwal. Note on the slow rotation or rotary oscillation of axisymmetric bodies in hydrodynamics and magnetohydrodynamics. *J. Fluid Mech.*, 41(4):721–726, 1970.

[14] P. Tekasul, R. V. Thompson, and S. K. Loyalka. Rotatory oscillations of arbitrary axi-symmetric bodies in an axi-symmetric viscous flow: numerical solutions. *Phys. Fluids*, 10:2797, 1998.

[15] P. Tekasul and S. K. Loyalka. Rotatory oscillations of axi-symmetric bodies in an axi-symmetric viscous flow with slip: numerical solutions for sphere amd spheroids. *Int. J. Numer. Mech. Fluids*, 41:823–840, 2003.

[16] U. Lei, C. Y. Yang, and K. C. Wu. Viscous torque on a sphere under arbitrary rotation. *Appl. Phys. Lett.*, 181908:1–24, 2006.

[17] W. Zhang and H. Stone. Oscillatory motions of circular disks and nearly spherical particles in viscous flows. *J. Fluid Mech.*, 367:329–358, 1998.

[18] G. F. Carrier and R. C. Di Prima. On the torsional oscillations of a solid sphere in a viscous fluid. *J. Appl. Mech.*, 23:601–605, 1956.

[19] R. C. Di Prima and N. Liron. Effect of secondary flow on the decaying torsional oscillations of a sphere and a plane. *Phys. Fluids*, 19:1450, 1976.

[20] A. Gopinath. Steady streaming due to small-amplitude torsional oscillations of a sphere in a viscous fluid. *Quart. J. Appl. Math*, 46(3):501, 1993.

[21] Jeffery, G. B. On the steady rotation of a solid of revolution in a viscous fluid. *Proc. Lon. Math. Soc.*, 14:327338, 1915.

[22] G. Kirchoff. *Vorlesungen uber Mathematische Physik Mechanik*, 1, 1876.

[23] W. G. Bickley. The secondary flow due to a sphere rotating in a viscous fluid. *Phil. Mag.*, 25(170):746–752, 1938.

[24] W. D. Collins. On the steady rotation of a sphere in a viscous fluid. *Mathematika*, 2:42–47, 1955.

[25] H. Takagi. Viscous flow induced by slow rotation of a sphere. *J. Phys. Soc. Japan*, 42(1):319–325, 1977.

[26] H. Brenner. The Stokes resistance of an arbitrary particle. *Chem. Eng. Sci.*, 18:1–25, 1963.

[27] O. Sawatski. Das Strömungsfeld um eine rotierende Kugel. *Acta Mechanica*, 9:159–214, 1970.

[28] J. V. Kelkar, R. A. Mashelkar, and J. Ulbrecht. A rotating sphere viscometer. *J. Appl. Polym. Sci.*, 17:3069–3083, 1973.

[29] A. B. Basset. On the motion of a sphere in a viscous liquid. *Phil. Trans. Roy. Soc. London*, 179:43–63, 1888.

[30] K. E. Barret. On the impulsively started rotating sphere. *J. Fluid Mech.*, 27(4):779–788, 1967.

[31] S. C. R. Dennis and P. W. Duck. Unsteady flow due to an impulsively started rotating sphere. *Comput. Fluids*, 16(3):291–310, 1988.

[32] B. U. Felderhof. Transient flow caused by a sudden impulse or twist applied to a sphere immersed in a viscous incompressible fluid. *Phys Fluids*, 19:073102, 2007.

[33] F. Fueillebois and A. Lasek. On the rotational historic term in non-stationary Stokes flow. *Q. J. Mech. Appl. Math.*, 31(4):435–443, 1978.

[34] S. I. Rubinow and J. B. Keller. The transverse force on a spinning sphere moving in a viscous fluid. *J. Fluid Mech.*, 11(3):447, 1961.

[35] E. Loth. Lift of a solid spherical particle subject to vorticity and/or spin. *AIAA Journal*, 46(4):801–809, 2008.

[36] K. Walters and N. D. Waters. On the use of a rotating sphere in the measurement of elasto-viscous parameters. *Brit. J. Appl. Phys.*, 14:667–671, 1963.

[37] J. Leach, H. Mushfique, S. Keen, R. Di Leonardo, G. Ruocco, J. M. Cooper, and M. J. Padgett. Comparison of Faxén's correction for a microsphere translating or rotating near a surface. *Phys. Rev. E*, 79:026301, 2009.

[38] H. Brenner and R. M. Sonshine. Slow viscous rotation of a sphere in a circular cylinder. *Q. J. Mech. Appl. Math.*, 27(1):55–63, 1964.

[39] H. Takagi. Slow rotation of two touching spheres in viscous fluid. *J. Phys. Soc. Japan*, 36(3):875–877, 1974.

[40] H. Brenner. Effects of finite boundaries on the Stokes resistance of an arbitrary particle. *J. Fluid Mech*, 12(1):35–48, 1962.

[41] Q. Liu and A. Prosperetti. Wall effects on a rotating sphere. *J. Fluid Mech.*, 657:1–21, 2010.

[42] W. R. Dean and M. E. O'Neill. A slow motion of viscous liquid caused by the rotation of a solid sphere. *Mathematika*, 10:13–24, 1963.

[43] A. J. Goldman, R. G. Cox, and H. Brenner. Slow viscous motion of a sphere parallel to a plane wall - I. Motion through a quiescent fluid. *Chem. Eng. Sci.*, 22:637–651, 1967.

[44] J. Ashmore, C. del Pino, and T. Mullin. Cavitation in a lubrication flow between a moving sphere and a boundary. *Phys. Rev. Lett.*, 94:124501, 2005.

[45] M. Chaoui and F. Feuillebois. Creeping flow around a sphere in a shear flow close to a wall. *Q. J. Mech. Appl. Math.*, 56(3):381–410, 2003.

206

[46] H. Faxén. The resistance against the movement of a rigour sphere in viscous fluids, which is embedded between two parallel layered barriers. *Ann. Phys.*, 68:89–119, 1922.

[47] A. Ambari, B. Gauthier-Manuel, and E. Guyon. Wall effects on a sphere translating at constant velocity. *J. Fluid Mech.*, 149:235–253, 1984.

[48] G. S. Perkins and R. B. Jones. Hydrodynamic interaction of a spherical particle with a planar boundary - II. Hard wall. *Physica A*, 189:447–477, 1992.

[49] R. G. Cox. Motion of a solid sphere in a general flow near a plane boundary at zero Reynolds number. *J. Eng. Math.*, 30:177–213, 1996.

[50] K. Walters and N. D. Waters. On the interpretation of experimental results obtained from a rotating-sphere elastoviscometer. *Brit. J. Appl. Phys.*, 15:989–991, 1964.

[51] G. Besseris, I. F. Miller, and D. B. Yeates. Rotational magnetic particle microrheometry: the Newtonian case. *J. Rheol*, 43:591, 1999.

[52] S. J. Parkin, G. Knoner, T. A. Nieminen, N. R. Heckenberg, and H. Rubinsztein-Dunlop. Picoliter viscometry using optically rotated particles. *Phys. Rev. E*, 76:041507, 2007.

[53] K. Sakai, T. Hirano, and M. Hosoda. Electromagnetically spinning sphere viscometer. *Appl. Phys. Exp.*, 3:016602, 2010.

[54] E. Lauga and T. R. Powers. The hydrodynamics of swimming microorganisms. *Rep. Prog. Phys.*, 72:096601, 2009.

[55] E. M. Purcell. Life at low Reynolds number. *Am. J. Phys*, 45:3–11, 1977.

[56] O. S. Pak, W. Gao, J. Wang, and E. Lauga. High-speed propulsion of flexible nanowire motors: theory and experiments. *Soft Matter*, 7:8169, 2011.

[57] W. Gao, D. Kagan, O. S. Pak, C. Clawson, S. Campuzano, E. Chuluun-Erdene, E. Shipton, E. E. Fullerton, L. Zhang, E. Lauga, and J. Wang. Cargo-towing fuel-free magnetic nanoswimmers for targeted drug delivery. *Small*, 8(3):460–467, 2012.

[58] A. Najafi and R. Golestanian. Simple swimmer at low Reynolds number: three linked spheres. *Phys. Rev E.*, 69:062901, 2004.

[59] A. Najafi and R. Golestanian. Propulsion at low Reyholds number. *J. Phys.: Condens. Matter*, 17:S1203–S1208, 2005.

[60] R. Golestanian and A. Ajdari. Analytic results for the three-sphere swimmer at low Reynolds number. *Phys. Rev. E*, 77:036308, 2008.

[61] R. Golestanian and A. Ajdari. Mechanical response of a small swimmer driven by conformal transitions. *Phys. Rev. Lett.*, 100:038101, 2008.

[62] R. Golestanian. Three-sphere low-Reynolds-number swimmer with a cargo container. *Eur. Phys. J. E*, 25:1–4, 2008.

[63] M. Leoni, J. Kotar, B. Bassetti, P. Cicuta, and M. C. Lagomarsino. A basic swimmer at low Reynolds number. *Soft Matter*, 5:472–476, 2009.

[64] R. Zargar, A. Najafi, and M. Miri. Three-sphere low-Reynolds-number swimmer near a wall. *Phys. Rev. E.*, 80:026308, 2009.

[65] G. P. Alexander, C. M. Pooley, and J. M. Yeomans. Hydrodynamics of linked sphere model swimmers. *J. Phys.: Condens. Matter*, 21:204108, 2009.

[66] M. Taghiloo and M. Miri. Three-sphere magnetic swimmer in a shear flow. *Phys. Rev. E*, 88:023008, 2013.

[67] R. Dreyfus, J. Baudy, and H. A. Stone. Purcell's "rotator": mechanical rotation at low Reynolds number. *Eur. Phys. J. B*, 47:161–164, 2005.

[68] K. Polotzek and B. M. Friedrich. A three-sphere swimmer for flagellar synchronization. *New J. Phys.*, 15:045005, 2013.

[69] Y. Or and R. M. Murray. Dynamics and stability of a class of low Reynolds number swimmers near a wall. *Phys. Rev. E*, 79:045302(R), 2009.

[70] S. Zhang, Y. Or, and R. M. Murray. Experimental demonstration of the dynamics and stability of a low Reynolds number swimmer near a plane wall. *Proc. American Control Conference*, pages 4205–4210, 2010.

[71] F. Y. Ogrin, P. G. Petrov, and C. P. Winlove. Ferromagnetic microswimmers. *Phys. Rev. Lett.*, 100:218102, 2008.

[72] M. Belovs and A. Cēbers. Ferromagnetic microswimmer. *Phys. Rev. E*, 79:051503, 2009.

[73] R. Dreyfus, J. Baudy, M. L. Roper, M. Fermiger, H. A. Stone, and J. Bibette. Microscopic artificial swimmers. *Nature*, 437(6):04090, 2005.

[74] M. Roper, R. Dreyfus, J. Baudy, M. Fermiger, J. Bibette, and H. A. Stone. Do magnetic micro-swimmers move like eukaryotic cells? *Proc. R. Soc. A*, 464:877–904, 2008.

[75] R. Livanovičs and A. Cēbers. Magnetic dipole with a flexible tail as a self-propelling microdevice. *Phys. Rev. E*, 85:041502, 2012.

[76] E. Lauga. Floppy swimming: viscous locomotion of actuated elastica. *Phys. Rev. E*, 75:041916, 2007.

[77] C. H. Wiggins, D. Riveline, A. Ott, and R. E. Goldstein. Trapping and wiggling: elastohydrodynamics of driven microfilaments. *Biophys. J.*, 74(2):1043–1060, 1998.

[78] T. S. Yu, E. Lauga, and A. E. Hosoi. Experimental investigations of elastic tail propulsion at low Reynolds number. *Phys. Fluids*, 18:091701, 2006.

[79] *Yunsheng Product Manual.*

[80] Jackson, J. D. *Classical Electrodynamics Third Edition.* Wiley, 3rd edition, 1998.

[81] NOAA/NGDC and CIRES. US/UK World Magnetic Model – Epoch 2010.0 Main Field Total Intensity (F), January 2010.

[82] T. T. Lim. Dye and Smoke Vizualisation. In Smits, A. J. and Lim, T. T., editor, *Flow Visualization: Techniques and Examples*, page 45. Imperial College Press, 2000.

[83] R. B. Miles. Planar Laser Imaging. In Smits, A. J. and Lim, T. T., editor, *Flow Visualization: Techniques and Examples*, pages 93–94. Imperial College Press, 2000.

[84] M. Gharib and D. Daribi. Digital Particle Image Velocimetry. In Smits, A. J. and Lim, T. T., editor, *Flow Visualization: Techniques and Examples*, pages 123–147. Imperial College Press, 2000.

[85] Z. Ye, E. Diller, and M. Sitti. Micro-manipulation using rotational fluid flows induced by remote magnetic micro-manipulators. *J. Appl. Phys.*, 112:064912, 2012.

[86] P. Tierno, T. H. Johanse, and T. M. Fischer. Magnetically driven colloidal microstirrer. *J. Phys. Chem. B*, 111:3077–3080, 2007.

[87] B. H. McNaughton, R. R. Agayan, R. Clarke, R. G. Smith, and R. Kopelman. Single bacterial cell detection with nonlinear rotational frequency shifts of magnetic microspheres. *Appl. Phys. Lett.*, 91:224105, 2007.

[88] B. H. McNaughton, P. Kinnunen, R. G. Smith, S. N. Pei, R. Torres-Isea, R. Kopelman, and R. Clarke. Compact sensor for measuring nonlinear rotational dynamics of driven magnetic microspheres with biomedical applications. *J. Magn. Mag. Mater.*, 32:1648–1652, 2009.

[89] L. Yang and H. Liu. Stimuli-responsive magnetic particles and their applications in biomedical field. *Powder Technol.*, 2012.

[90] Q. A. Pankhurst, J. Connolly, S. K. Jones, and J. Dobson. Applications of magnetic nanoparticles in biomedicine. *J. Phys. D: Appl. Phys.*, 36:R167–R181, 2003.

[91] S. F. Medeiros, A. M. Santos, H. Fessi, and A. Elaissari. Stimuli-responsive magnetic particles for biomedical applications. *Int. J. Pharm.*, 403:139–161, 2011.

[92] Y. Man and E. Lauga. The wobbling-to-swimming transition of rotated helices. *Phys. Fluids*, 25:071904, 2013.

[93] Sedra, A. S. and Smith, K. C. *Microelectronic Circuits.* CBS College Publishing, 2nd edition, 1987.

[94] Landau, L. D. and Lifshitz, E. M. *Fluid Mechanics.* Butterworth-Heineman, 2nd edition, 1987.

[95] C. Otto. *The motion of a sphere in a Stokes flow near a wall.* PhD thesis, University of Manchester, UK, 2009.

[96] Han. E. *Magneto-elastic buckling and magnetic driven swimmer*. Master's thesis, University of Manchester, UK, 2012.

[97] R. Trouilloud, T. S. Yu, A. E. Hosoi, and E. Lauga. Soft swimming: exploiting deformable interfaces for low Reynolds number locomotion. *Phys. Rev. Lett.*, 101:048102, 2008.

[98] NOAA/NGDC and CIRES. US/UK World Magnetic Model – Epoch 2010.0 Main Field Inclination (I), January 2010.

[99] J. T. Stuart. Unsteady boundary layers. In Rosenhead, L., editor, *Laminar Boundary Layers*, pages 349–408. Oxford University Press, 1963.

[100] C. Pozrikidis. A singularity method for unsteady linearized flow. *Phys. Fluids*, 1:1508, 1989.

[101] Pozrikidis, C. *Boundary integral and singularity methods for linearized viscous flow*. Cambridge University Press, 1992.

[102] J. R. Blake. A note on the image system for a stokeslet in a no-slip boundary. *Proc. Cam. Phil. Soc.*, 70:303–310, 1971.

[103] J. R. Blake and A. T. Chwang. Fundamental singularities of viscous flow. *J. Eng. Maths*, 8:23–29, 1974.

[104] T. Mullin, S. Deschanel, K. Bertoldi, and M. C. Boyce. Pattern transformation triggered by deformation. *Phys. Rev. Lett.*, 99:084301, 2007.